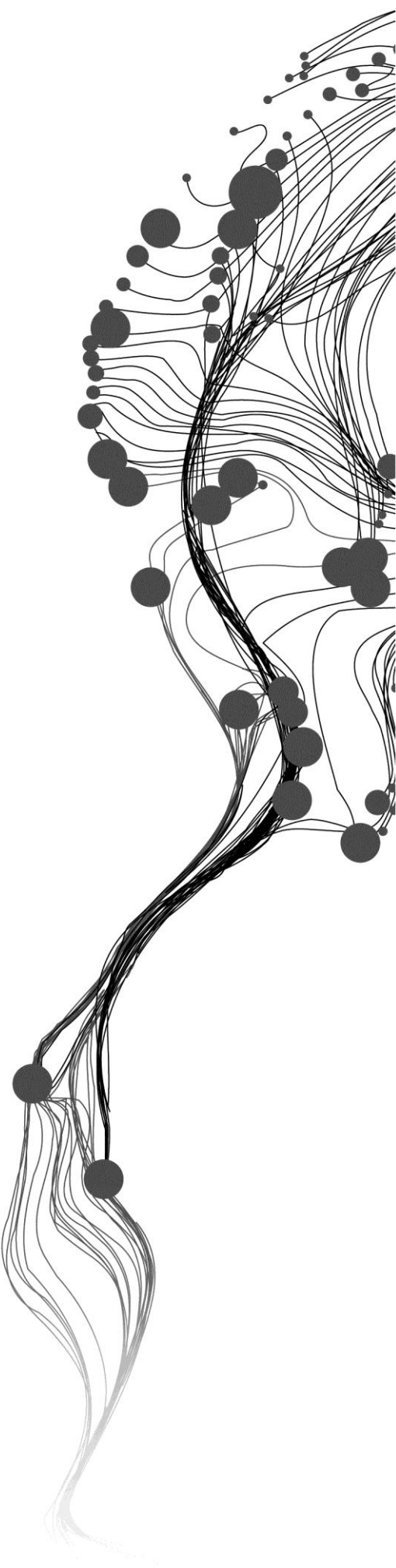


EARTH STRUCTURE USING INTEGRATED SATELLITE GRAVITY, SEISMIC TOMOGRAPHY AND 3D OBJECT ORIENTED ANALYSIS

ISLAM ELSAYED ABDELAZIZ MOHAMED FADEL
MARCH, 2013

SUPERVISORS:
Dr. M. (Mark) van der Meijde
Dr. N. (Norman) Kerle



EARTH STRUCTURE USING INTEGRATED SATELLITE GRAVITY, SEISMIC TOMOGRAPHY AND 3D OBJECT ORIENTED ANALYSIS

ISLAM ELSAYED ABDELAZIZ MOHAMED FADEL
Enschede, The Netherlands, MARCH, 2013

Thesis submitted to the Faculty of Geo-Information Science and Earth Observation of the University of Twente in partial fulfilment of the requirements for the degree of Master of Science in Geo-information Science and Earth Observation.

Specialization: Earth Resources Exploration

SUPERVISORS:

Dr. M. (Mark) van der Meijde

Dr. N. (Norman) Kerle

THESIS ASSESSMENT BOARD:

Prof. Dr. F.D. (Freek) van der Meer (Chair)

Prof. Dr. S.M. (Steven) de Jong (External Examiner, Utrecht University)

DISCLAIMER

This document describes work undertaken as part of a programme of study at the Faculty of Geo-Information Science and Earth Observation of the University of Twente. All views and opinions expressed therein remain the sole responsibility of the author, and do not necessarily represent those of the Faculty.

ABSTRACT

Non-uniqueness of satellite gravity interpretation has been usually reduced by using *a priori* information from seismic tomography models. This reduction in the non-uniqueness using seismic tomography has usually introduced additional uncertainty through the conversion relations or the bias in the interpretation due to user choices and experience. The interpretation of satellite gravity using seismic tomography models has been based on velocity-density conversion formulas or user interpretation for the 3D subsurface structures (objects) in the seismic tomography models. This has been done without a standardized methodology on how to extract the subsurface structures from 3D subsurface data.

In this research, a new methodology is introduced to extract the 3D subsurface structures from 3D geophysical data using a state-of-art 3D Object Oriented Image Analysis (OOA) technique. The 3D OOA is tested using a set of synthetic models that simulate the real situation in the study area of this research. Then, 3D OOA is used to extract the 3D subsurface objects from real 3D seismic tomography model of the study area. After that, the extracted 3D objects are used to reconstruct a forward model and compare its signal with the measured satellite gravity. Finally, the result of the forward modelling, based on the extracted 3D objects, is used to constrain the inversion process of satellite gravity data.

Through this work, a new object-based approach is introduced to interpret and extract the 3D subsurface objects from 3D geophysical data. This can help in interpreting other 3D geophysical datasets that need long time and experience users. Also, a new approach is introduced to constrain modelling and inversion of potential field data using the extracted 3D subsurface structures from other methods. Finally, a new approach is introduced to constrain interpretation of the satellite gravity measurements that can be applied using any 3D seismic tomography model.

ACKNOWLEDGEMENTS

First and foremost, praise and thanks to Allah (God) almighty who gave me the knowledge to finish this work.

Many thanks to the Erasmus Mundus scholarship providers who fully financed my MSc study. I would like to thank Prof. Dr. Hans-Jurgen Gotze and his research team at Kiel University for providing the academic license of IGMAS+ software. Also, I would like to thank Prof. Doug Oldenburg and his research team at University of British Columbia for providing the academic license of GRAV3D inversion software. Many thanks for Dr. Aubreya Adams at Washington University for making the seismic tomography model of the study area available to this study. Also, I wish to thank Dr. Fabio Cammarano at University of Copenhagen for providing us with the density and thermal models.

The words cannot describe my thankfulness to my supervisors Mark van der Meijde and Norman Kerle. Their wisdom, guidance, critical comments, fruitful discussions, and invaluable encouragement were the reason to accomplish this research.

Deep gratitude is to all the staff members of Earth Resource Exploration domain for their encouragement and invaluable lectures and materials during my studies. Special thanks are for Dr. Marleen Noomen for her continuous encouragement.

Also, I cannot forget to mention my grateful to all my professors in Helwan University and especially Prof. Amin Ismail for initiating my geophysical and geological background during my Bachelor degree.

Finally, it is a pleasure to thank my classmates for the times that we shared together and the continuous encouragement and support.

TABLE OF CONTENTS

Contents

1.	Introduction.....	1
1.1.	Background.....	1
1.1.1.	Satellite gravity.....	1
1.1.2.	Non-uniqueness of geophysical data	1
1.1.3.	The modelling and inversion methods	2
1.1.4.	Solving the problem of non-uniqueness	4
1.1.5.	The role of image analysis techniques in potential field interpretation.....	4
1.2.	Problem Statement.....	5
1.3.	Research Objective.....	6
1.4.	Research questions	6
1.5.	Methodology	6
1.6.	Thesis Structure	7
2.	Study area and datasets	9
2.1.	The tectonic configuration in the study area	9
2.1.1.	Tanzania Craton:.....	10
2.1.2.	The Ugandan Basement Complex:	10
2.1.3.	The Rift Branches	11
2.1.4.	The Plume:.....	11
2.2.	Dataset.....	12
2.2.1.	S-wave seismic tomography and density models	12
2.2.2.	Satellite gravity data	12
2.3.	Synthetic models.....	14
2.3.1.	The simple models.....	14
2.3.2.	Complex models	15
3.	Methodology.....	17
3.1.	The first stage: 3D OOA	17
3.1.1.	Purpose.....	17
3.1.2.	Datasets	17
3.1.3.	Software.....	17
3.1.4.	Methodology.....	18
3.1.5.	Expected outputs	18
3.2.	The second stage: Forward modeling (including object based inversion)	18
3.2.1.	Purpose:.....	18
3.2.2.	Datasets	18
3.2.3.	Software.....	19
3.2.4.	Methodology.....	19
3.2.5.	Expected Outputs.....	19
3.3.	The third stage: Constrained Inversion	20
3.3.1.	Purpose.....	20
3.3.2.	Datasets	20
3.3.3.	Software.....	20
3.3.4.	Methodology.....	21
3.3.5.	Expected Outputs.....	21
4.	Results and Discussions.....	22
4.1.	Synthetic modelling.....	22
4.1.1.	Results 3D OOA.....	22
4.1.2.	Discussion 3D OOA.....	30
4.1.3.	Results forward modelling (including object based inversion)	30
4.1.4.	Discussion forward modelling (including object based inversion)	32
4.1.5.	Results constrained inversion.....	33
4.1.6.	Discussion constrained inversion.....	34

4.1.7.	General discussion on synthetic models results	34
4.2.	Application to eastern Africa rift system.....	36
4.2.1.	Results 3D OOA	36
4.2.2.	Discussion 3D OOA.....	39
4.2.3.	Results forward modelling (including object based inversion).....	40
4.2.4.	Discussion forward modelling (including object based inversion).....	42
4.2.5.	Results constrained inversion	46
4.2.6.	Discussion Constrained inversion.....	48
5.	Conclusion and Recommendation.....	51
5.1.	Conclusion	51
5.2.	Recommendations	52

LIST OF FIGURES

FIGURE 1: THE PROBLEM OF NON-UNIQUENESS INVERSION OF POTENTIAL FIELD DATA MODIFIED FROM (ELLIS, 2010). THE MEASURED GRAVITY SIGNAL ABOVE THE EARTH SURFACE COULD BE FITTED BY SEVERAL SUBSURFACE MODELS USING DIFFERENT INVERSION PARAMETERS.....	1
FIGURE 2: FLOW CHART EXPLAINING THE DIFFERENT INTERPRETATION METHODS OF POTENTIAL FIELD DATA.	2
FIGURE 3: FLOWCHART DESCRIBING THE METHODOLOGY OF THE RESEARCH.	7
FIGURE 4: THE STUDY AREA WITH THE MAJOR CENOZOIC RIFT FAULTS DRAWING IN BLACK LINES (ADAMS ET AL., 2012).	9
FIGURE 5: THE DISTRIBUTION OF THE SEISMIC STATIONS (ADAMS ET AL., 2012).	9
FIGURE 6: A), B), AND C) THE AVERAGE SHEAR WAVE VELOCITY OF THE GEOLOGICAL REGIONS WITHIN THE STUDY AREA. D) AND E) THE RECOMMENDED MODELS OF ADAMS ET AL. (2012) SEISMIC TOMOGRAPHY MODEL INTERPRETATION	10
FIGURE 7 ADAPTED FROM ADAMS ET AL. (2012):	11
FIGURE 8: A) THE S-WAVE SEISMIC TOMOGRAPHY MODEL OF THE STUDY AREA WAS ADAPTED FROM ADAMS ET AL. (2012). B) THE DENSITY MODEL WAS DERIVED BASED ON THE S-WAVE SEISMIC TOMOGRAPHY MODEL ADAPTED FROM CAMMARANO (2013). (C) THE FREE-AIR SATELLITE GRAVITY SIGNAL OF THE STUDY AREA FROM EIGEN-6C MODEL. (D) THE TOPOGRAPHY OF THE STUDY AREA ETOPO MODEL. (E) THE TERRAIN CORRECTION OF THE FREE AIR DATA USING ETOPO TOPOGRAPHY. (F) THE BOUGUER ANOMALY MAP BASED ON THE TERRAIN CORRECTION.	13
FIGURE 9: THE SYNTHETIC MODELS DESCRIBED IN TABLE 1.	14
FIGURE 10: THE FIRST COMPLEX SYNTHETIC MODEL	15
FIGURE 11: THE SECOND COMPLEX MODEL.....	16
FIGURE 12: (A) THE 3D IMAGE STACK OF THE SECOND COMPLEX MODEL REPRESENTS IN THE 'RGBGREY' COLOUR SCHEME START AT THE TOP LEFT THE FIRST SLICE WITH DEPTH ZERO MOVING WITH DEPTH INTERVAL 125 M TO THE END OF THE FIRST ROW SLICE NUMBER 8 THEN MOVING TO THE NEXT ROW AND CONTINUE IN THE SAME WAY TO THE BOTTOM LEFT END SLICE NUMBER 56. (B) THE VOXEL CUBE OF THE SAME MODEL IN 'RGBGREY' COLOUR SCHEME ON THE LEFT.....	17
FIGURE 13: (A), (B), (C), (D), AND (E) 3D OOA RESULTS FOR THE SIMPLE SYNTHETIC MODELS. F) EXAMPLE OF THE IMAGE SLICES WERE USED AS INPUT FOR 3D OOA OF THE BOX SYNTHETIC MODEL.	22
FIGURE 14: THE PROCESS OF EXTRACTING OBJECT WITH 3D FUZZY BOUNDARIES. (A) FIGURE SHOWS THE EFFECT OF THE SEGMENTATION PARAMETERS ON THE SEGMENTATION PROCESS SINCE SEGMENTS ARE SMALL AT THE BOUNDARIES OF THE CYLINDER AND LARGER IN THE MIDDLE OF THE CYLINDER AND IN THE WHITE BACKGROUND SURROUNDING THE OBJECT. (B) A CROSS SECTION BETWEEN X AND Y TO SHOW THE EFFECT OF THE SEGMENTATION VERTICALLY. (C) THE MEMBERSHIP FUNCTION TO CLASSIFY THE FUZZY BOUNDARIES. (D) THE CLASSIFIED CYLINDER WITH THE FUZZY ZONE SURROUNDING IT.....	23
FIGURE 15: FLOW CHART SHOWS THE STAGE OF 3D OOA FOR THE FIRST COMPLEX MODEL.	24
FIGURE 16: FIGURE SHOWS THE EFFECT OF THE SEGMENTATION PARAMETERS ON THE MULTI-RESOLUTION SEGMENTATION ALGORITHM ON THE SIZE OF THE SEGMENTS.	24
FIGURE 17: CROSS SECTION SHOWS THE SELECTION OF THE THRESHOLDS. THE BACKGROUND HAD THE DARKEST COLOR EQUAL TO PIXEL VALUE 12 THEN THE CRATON WITH PIXEL VALUE 24, WHILE THE RIFTS HAD A LIGHT GREY COLOR EQUAL TO PIXEL VALUE 128. THE WHITE RECTANGULAR SHOWS THE ZONE OF MIXED RIFTS AND PLUME BOUNDARIES WITH ITS TOP -2800 AND BOTTOM -3950 DEPTH VALUES.....	25
FIGURE 18: AN EXAMPLE FOR 'FIND ENCLOSED BY' ALGORITHM. THE GREEN OBJECT INSIDE THE RED CLASS IN THE LEFT IMAGE WAS DEFINED AND CLASSIFIED INTO THE BLACK CLASS AFTER USING THE ALGORITHM.	25
FIGURE 19: THE ALGORITHM OF "PIXEL-BASED OBJECT RESIZING" THE IMAGES TO THE LEFT BEFORE APPLYING THE ALGORITHM AND THE IMAGES TO THE RIGHT AFTER APPLYING IT. THE LIGHT BLUE OBJECT GREW VERTICALLY IN THE NEGATIVE Z DIRECTION INTO THE GREEN CLASS.....	25
FIGURE 20: AN EXAMPLE FOR 'GROW REGION' ALGORITHM. THE CYAN OBJECT GREW IN THE SEGMENTS OF THE GREEN OBJECT AFTER USING THE ALGORITHM.	26
FIGURE 21: A) TO F) ARE THE SIX STAGES OF THE 3D OOA. G) IMAGE IS THE FINAL RESULTS AFTER THE REFINING STAGE WITH 50% TRANSPARENT DISPLAY FOR THE OBJECTS. H) IMAGE IS THE FINAL CLASSIFIED OBJECTS WITH ZOOM AND REMOVING THE BACKGROUND CLASS FROM THE DISPLAY.	26
FIGURE 22: FLOW CHART SHOWING THE STAGES OF 3D OOA FOR THE FIRST COMPLEX MODEL.....	27
FIGURE 23: CROSS SECTION EXPLAINS THE THRESHOLDS SELECTION. THE DEPTH VALUES FOR THE CRATON, RIFTS AND PLUMES ARE SHOWN. ALSO, THE LOCATION OF THE THREE LAYERS AND THE ZONE OF MIXED RIFTS AND PLUME BOUNDARIES ARE SHOWN ...	27
FIGURE 24: FIGURE SHOWS THE DIFFERENCE IN THE SHAPE INDEX (SI) BETWEEN LAYER 2 SEGMENTS AND LAYER 3 SEGMENTS	28
FIGURE 25: FIGURE SHOWS WHITE ARROWS INDICATING THE SEGMENTS BELONG TO THE RIFT BOUNDARY THAT HAVE HIGHER SI FROM THE OTHER SEGMENTS THAT HAVE SMOOTH SURFACE AND HENCE LOWER SI.	28

FIGURE 26: THE STRATEGY TO CLASSIFY THE PLUME BOUNDARIES IN GREEN COLOR. 1) BEFORE AND 2) AFTER “FIND ENCLOSED BY ALGORITHM”. 3) THE VERTICAL GROWING IN THE DEEPER SLICE. 4) AFTER GROW IN THE X AND Y DIRECTION UNTIL FILL THE CIRCULAR SHAPE. 5) AFTER GROW IN THE X DIRECTION ONLY TO PREVENT FURTHER GROWING IN THE MISCLASSIFIED SEGMENTS WITHIN THE RIFT BOUNDARIES.	29
FIGURE 27: (A) THE IMAGE STACK AFTER CLASSIFYING THE BACKGROUND AND THE MODEL ZONE (B) THE CLASSIFICATION OF THE PLUME. (C) THE CLASSIFICATION OF THE CRATON. (D) THE CLASSIFICATION OF THE FIRST LAYER. (E) THE CLASSIFICATION OF THE SECOND LAYER. (F) THE CLASSIFICATION OF THE THIRD LAYER. (G) THE CLASSIFICATION OF THE RIFT. (H) THE CLASSIFICATION OF THE RIFTS AND PLUME BOUNDARIES. (I) THE CLASSIFIED COMPLETE MODEL.	29
FIGURE 28: COLUMN (A) IS THE ORIGINAL SECTIONS IN IGMAS+. COLUMN (B) IS THE SECTIONS BEFORE 3D OOA IN eCOGNITION. COLUMN (C) IS THE CLASSIFIED SECTIONS AFTER 3D OOA ANALYSIS. COLUMN (D) IS THE CONSTRUCTED MODEL BASED ON THE CLASSIFIED SECTIONS FROM 3D OOA IN COLUMN C.	31
FIGURE 29: (A) THE MEASURED GRAVITY SIGNAL. (B) THE CALCULATED GRAVITY SIGNAL. (C) THE DIFFERENCE BETWEEN THE CALCULATED AND THE MEASURED GRAVITY SIGNAL.	31
FIGURE 30: (A) THE RETRIEVED DENSITY CONTRASTS IN CASE OF USING THE DENSITY CONSTRAINTS AS INITIAL MODEL. (B) THE RETRIEVED DENSITY CONTRASTS IN CASE OF USING THE DENSITY CONSTRAINTS AS REFERENCE MODEL. (C) THE RETRIEVED DENSITY CONTRASTS IN CASE OF USING THE DENSITY CONSTRAINTS AS BOUNDS. (D) THE DIFFERENCE IN CASE OF USING THE DENSITY CONSTRAINTS AS INITIAL MODEL. (E) THE DIFFERENCE IN CASE OF USING THE DENSITY CONSTRAINTS AS REFERENCE MODEL. (F) THE DIFFERENCE IN CASE OF USING THE DENSITY CONSTRAINTS AS BOUNDS. (G) THE MEASURED GRAVITY DATA. (H) THE ASSIGNED STANDARD DEVIATION ERROR TO IT AFTER PREPARING IT FOR THE INVERSION.....	35
FIGURE 31: FLOW CHART SHOW THE STRATEGY THAT WAS USED TO CLASSIFY THE 3D S-WAVE SEISMIC TOMOGRAPHY MODEL.	37
FIGURE 32: (A) THE RAW IMAGE SLICES. (B) THE CUBE AFTER THE SEGMENTATION. (C) THE CUBE AFTER THE CLASSIFICATION OF THE HIGH VELOCITY ZONE BELOW THE PLUME. (D) THE CUBE AFTER THE CLASSIFICATION OF THE CRATON. (E) THE CUBE AFTER THE CLASSIFICATION OF THE PLUME. (F) THE CUBE AFTER THE CLASSIFICATION OF THE RIFT. (G) LAYER 1. (H) LAYER 2. (I) LAYER 3. (J) THE CUBE AFTER THE FINALIZING STAGE.....	38
FIGURE 33: (A) THE RESULTS OF THE SEGMENTATION TEST USING 15 THRESHOLDS (THE WHITE BOX INDICATING THE EFFECT OF LOSING SOME DETAILS RELATED TO THE GRAVITY ANOMALY WHICH WILL BE EXPLAINED) LATER AND (B) THE ORIGINAL SEGMENTATION USING 10. (C) THE 3D VIEW OF THE BASIC 10 CLASSES AND ALSO SHOW THE MIRROR IMAGE EFFECT IN COMPARISON WITH FIGURE (B). (D) FIGURE SHOWS THE EFFECT OF DEGRADING THE FOUR CLASSES (DARK RED, THE RED, THE ORANGE, AND THE YELLOW) IN (C) DURING THE CLASSIFICATION TO THE CRATON CLASS.....	39
FIGURE 34: (A) THE HISTOGRAM OF THE SLICE AT 50 KM DEPTH. (B) THE HISTOGRAM OF DEPTH 300 KM. THE FIGURES SHOW THE DIFFERENCE IN THE RANGE OF VELOCITY CONTENTS THROUGH THE DEPTH.	40
FIGURE 35: (A) THE RESULTS USING 111 KM COSINE ROLL-OFF FILTER SHOWING THE IMPERFECTION IN THE FILTERING PROCESS. (B) THE CALCULATED GRAVITY SIGNAL AFTER THE OBJECT BASED INVERSION. (C) THE IMPORTING PROCESS OF THE CLASSIFIED SECTIONS OUT FROM 3D OOA. (D) THE IMPORTING PROCESS OF THE CLASSIFIED SLICES. (E) AND (F) TWO SECTIONS FROM THE RECONSTRUCTED AND THEIR OBSERVED AND CALCULATED SIGNAL. (G) THE RECONSTRUCTION PROCESS OF THE HIGH VELOCITY ZONE BELOW THE MANTLE. (H) THE RECONSTRUCTION OF THE PLUME. (I) THE RECONSTRUCTION OF THE THREE LAYERS, CRATON AND RIFTS. (J) THE COMPLETE MODEL.....	42
FIGURE 36: (A) THE BOUGUER ANOMALY MAP OF THE STUDYA AREA (B) THE FILTERED BOUGUER MAP USING COSINE ROLL-OFF LOW PASS FILTER > 400 KM. (C) THE FORWARD GRAVITY SIGNAL FROM THE DEEPER PART FROM THE RECONSTRUCTED MODEL USING PLUME AND THE HIGH VELOCITY ZONE BELOW IT. (D) THE BOUGUER ANOMALY MAP ADAPTED FROM SIMIYU AND KELLER (1997). (E) THE LOW PASS FILTERED BOUGUER MAP USING PASS > 1000 KM THAT CORRELATE WITH THE FORWARD GRAVITY SIGNAL ADAPTED FROM SIMIYU AND KELLER (1997). (F) THE POWER SPECTRUM OF THE BOUGUER GRAVITY SIGNAL. (G) THE DEPTH ESTIMATION BASED ON THE POWER SPECTRUM.	43
FIGURE 37: FIGURE SHOWS THE EFFECT OF THE CLASS MERGING ON THE FORWARD MODELLING STAGE. (A) AND (D) SHOW THE DETAILS THAT EXISTED IN THE MODEL BEFORE THE PROCESS OF THE DEGRADATION OF THE CLASSES THAT RELATED TO THE RIFT IN BLUE RECTANGULAR, THE NORTHERN PORTION OF THE CRATON IN GREEN RECTANGULAR (ALSO SEE FIGURE 33 (A)) AND THE CENTRAL PORTION OF THE CRATON IN WHITE THAT SEEMS TO BELONG TO SHALLOW DEPTHS ANOMALIES. (B) AND (C) SHOW THE EFFECT OF THE CLASS DEGRADATION DURING THE CLASSIFICATION OF THE CRATON IN THE FORWARD MODELLING SIGNAL.....	44
FIGURE 38: FIGURE SHOWS THE LOW TEMPERATURE IN THE ZONE THAT CAN BE THE REASON FOR THE LOW VELOCITY IN THE INNER PLUME ZONE.	45
FIGURE 39: FIGURE SHOWS THE COMPARISON BETWEEN (A) THE WORK OF SIMIYU AND KELLER (1997) AND (B) THE MODELLING OF THIS RESEARCH. (C) THE STUDY AREA MAP THAT SHOWS THE LOCATION AND THE EXTENT OF BOTH SECTIONS.	45
FIGURE 40: (A), (B), (C), (D), (E), (F), (G) AND (H) ARE THE RESULTS OF THE INVERSION PROCESS USING DENSITY CONSTRAINTS AS A REFERENCE MODEL. (I) BOUGUER SATELLITE GRAVITY MEASUREMENTS. (J) THE ADDED ERROR TO THE BOUGUER MEASUREMENTS. (K) THE PREDICTED GRAVITY SIGNAL. (L) THE DIFFERENCE BETWEEN THE MEASURED BOUGUER SIGNAL AND THE PREDICTED SIGNAL.	47

FIGURE 41: (A) CAMMARANO (2013) DENSITY MODEL AND (B) USING SEVEN EQUAL INTERVALS ISO-SURFACES. (C) THE DENSITY
MODEL OUT OF THIS STUDY. 49

LIST OF TABLES

TABLE 1: THE DETAILED DESCRIPTION OF THE SIMPLE SYNTHETIC MODELS.	14
TABLE 2: THE DETAILED DESCRIPTION OF THE FIRST COMPLEX MODEL.	15
TABLE 3: THE DETAILED DESCRIPTION OF THE SECOND COMPLEX MODEL.	16
TABLE 4: TABLE SHOWS THE ORIGINAL DENSITY VALUES AND THE RETRIEVED DENSITY CONTRAST.	32
TABLE 5: TABLE SHOWS THE FULL DETAILS OF 3D OOA OF THE REAL DATA.	37
TABLE 6: TABLE SHOWS THE RESULTS OF THE OBJECT BASED INVERSION PROCESS. THE REFERENCE VALUES WERE BASED ON RESULTS FROM EBBING ET AL. (2001) BASED ON THE EQUATION OF CHRISTENSEN AND MOONEY (1995). THEY ESTIMATED THE REFERENCE MODEL UP TO DEPTH 180 KM. CONSEQUENTLY THERE WERE NO AVAILABLE VALUES FOR THE DEEPER OBJECTS.	41
TABLE 7: TABLE SHOWS THE SPATIAL GEOMETRY OF THE EXPORTED 3D MODEL OUT OF THE FORWARD MODELLING PROCESS.	46
TABLE 8: TABLE SHOWS THE SELECTED PARAMETERS FOR THE INVERSION PROCESS AND THE EXPLANATION BEHIND THE SELECTION OF EACH PARAMETER VALUE.	46

1. INTRODUCTION

1.1. Background

Geophysical data are the main source of information about the subsurface. They represent a critical stage in the exploration process for mineral, underground water, oil and gas exploration. Further, they are the main source for information about the composition of the deep interior of the Earth (e.g. lithosphere, mantle composition, structure and dynamics). Potential field data are geophysical data that measure the potential fields of the Earth (e.g. gravity and magnetic fields). These potential fields are mainly affected by the distribution of the physical properties in the subsurface (e.g. gravity measurements are affected by the density distribution in the subsurface and magnetic measurements are affected by magnetic susceptibility distribution). They played a vital role side by side with seismic tomography in modelling the Earth subsurface and especially in regional studies where the studies related to the large geographical regions.

1.1.1. Satellite gravity

Satellite gravity is gravity field measurements that were available recently in the last decade. Recent satellite missions were launched like CHAMP in 2000, GRACE in 2002, and GOCE in 2009 to measure the global gravity field (Greicius, 2012, Tapley and Kim, 2001). The global coverage and the consistent data quality are the most significant advantages of the satellite gravity data (Nabighian et al., 2005). The GOCE satellite has a state-of-the-art gradiometer with accuracy of $\sim 1\text{mGal}$ and an orbital height of 250 km that allowed a high spatial resolution ($\sim 40\text{ km}$) and strong gravity signals (Loekken, 2012b, van der Meijde, 2011). The European Space Agency (ESA) expected that new data from GOCE satellite will help in studies of (i) the Earth's interior physics, (ii) geodynamics associated with the lithosphere, (iii) mantle composition and rheology, and (iv) uplift and subduction processes (Loekken, 2012a).

1.1.2. Non-uniqueness of geophysical data

One of the main issues for interpreting potential field data and subsequently satellite gravity is the non-uniqueness of inversion processes. In an inversion process, field measurements above the earth surface are inverted into a 2- or 3D subsurface spatial distribution of the physical property related to these measurements (e.g. density subsurface distribution in case of gravity measurements) (Wang et al., 2012). The non-uniqueness of the inversion process means that an infinite number of subsurface models can be produced and fit the same field measurements (Figure 1) (Barbosa and Silva, 2011, Claerbout, 1988). Therefore, it needs additional information to reduce such non-uniqueness, which is not easy task and especially in regional studies (Tedla et al., 2011).

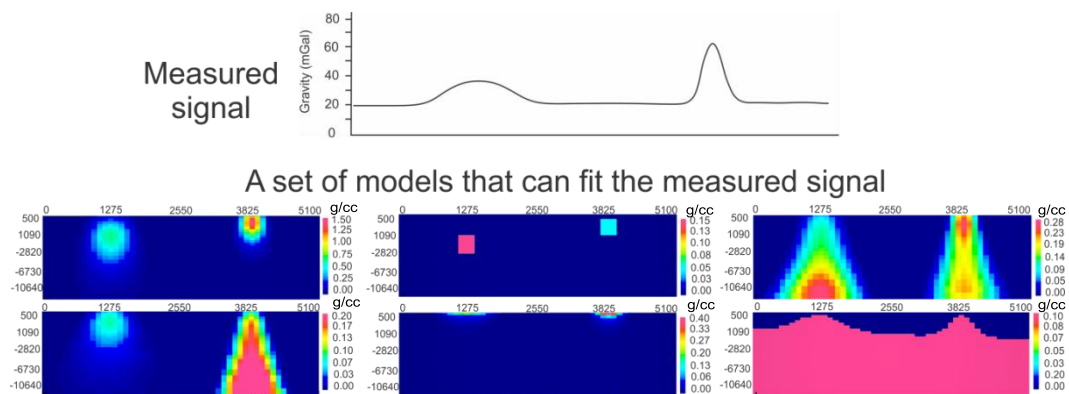


Figure 1: The problem of non-uniqueness inversion of potential field data modified from (Ellis, 2010). The measured gravity signal above the earth surface could be fitted by several subsurface models using different inversion parameters

1.1.3. The modelling and inversion methods

Several methods were used to model and inverse the subsurface using the potential field data. Barbosa and Silva (2011), Nabighian et al.(2005) and Fedi and Pilkington (2012) reviewed methods that were used to inverse and reconstruct subsurface bodies using potential field data. The methods can be divided into two groups: Forward methods, and inverse methods (Figure 2).

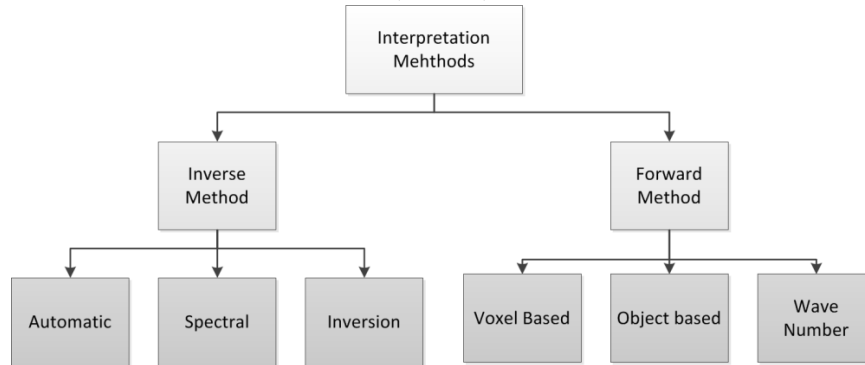


Figure 2: Flow chart explaining the different interpretation methods of potential field data.

1.1.3.1. Forward methods

Forward methods mainly use *a priori* information about the subsurface in order to construct a 3D subsurface model for the area of interest. The calculated geophysical signal resulted from the estimated model is compared with the measured geophysical signal in order to evaluate the constructed model. The most common approaches for the forward modelling are the Haaz (1953) approach (which was adapted in the UBC-GIF software package (Li and Oldenburg, 1996, Li and Oldenburg, 1998)) and the Goetze et al. (1988) approach (implemented in the IGMAS+ software package) (see also Figure 2). The main difference between the two approaches is the method of constructing 3D subsurface models.

First, the Li and Oldenburg (1998) approach used the Haaz (1953) solution for the forward modelling equations that depends on the voxel cube representation of subsurface structure. Second, the Goetze et al. (1988) approach was based on the analytical solution of the volume integral of the 3D polyhedral homogenous body (object based representation) of the 3D subsurface models.

Another method for forward modelling was introduced by Li (2010). The method mainly is based on dividing the studied models into layers and bodies. Then, the effect of each component in the model is calculated in the wavenumber domain. After that, all effects are added in the end in the spatial domain. This method is characterized by its fast computation. Schmidt et al. (2011) reviewed the three different approaches and compared between them.

In general, the forward modelling methods are subjective due to the necessity of the methods to *a priori* information and the dependency of the methods on the user experience who interpret the available *a priori* information to build the subsurface models.

1.1.3.2. Inverse Methods

The inverse methods can be divided into 3 categories (Figure 2):

(i) Automatic methods

The automatic methods (e.g. Euler Deconvolution (Thompson, 1982) and Werner Deconvolution (Hartman et al., 1971)) do not require *a priori* information about the subsurface densities or the shape bounds of the subsurface objects. However, these methods are still far away from producing a reasonable 3D subsurface model because they either produce subsurface point source distribution (Reid et al., 1990) or a contact surface between two media with different physical properties (Mushayandebvu et al., 2004).

(ii) Spectral methods

The spectral methods can be divided into two groups. The first one is based on the statistical spectral method (Spector and Grant, 1970). The second one is based on the spectral content of the potential field data (Parker, 1973).

- 1- The spectral statistical method (Spector and Grant, 1970) is based on the concept that the anomalies from the deep-seated sources have low wavenumber characteristics while the anomalies from the shallow-seated sources have high wavenumber characteristics. In other words, the average radial power spectrum is exponentially proportional increased toward the low wavenumber. The method estimates the average depth of the local and deep seated sources. Barbosa and Silva (2011) mentioned the advantages and disadvantages of the statistical spectral method. The advantages were that it is easy to implement, does not require a high speed computer, is usable in situations with vertically interfered sources, and estimated depths are stable. The disadvantages were that the average depth estimate of the anomalies cannot give detailed information about the variation of the estimated depth, and the underlying assumption that the shallow and deep seated sources have non overlapping spectra restricts the method because it assumes that the shallow and deep sources have a large vertical separation.
- 2- The second group is based on the spectral inversion method. The spectral inversion method is based on the spectral content of the data. The method aims to map the depth to an interface separating two homogenous media using the sum of Fourier transforms of potential field data (Parker, 1973, Gómez-Ortiz and Agarwal, 2005). Barbosa and Silva (2011) discussed the advantage and disadvantages of this group of methods. The advantage is the rapid calculation of the gravity anomaly response. The disadvantages were manifold and include the necessity of the method to depend on *a priori* or estimated information, the effect of the shallow anomalous sources above or overlying the target interface are not included, and the assumptions of the smoothness of the interface that require a low pass filter or employing of a damping parameter.

(iii) Inversion methods

Inversion methods are based on the concept of discretising the subsurface into a cube with 3D cells called voxels. Then, the potential field measurements are used to estimate the 3D distribution of the physical properties in each cell. They can be divided into three groups:

- 1- The first one uses smooth regularization for the solution as the work done by Li and Oldenburg (1998). The advantage of this group of methods is the good retrieval of shallow anomalies. The disadvantage is the necessity to include *a priori* information about the top of the sources and information about the density distribution to constrain the inversion process. The amount of available *a priori* information determines the quality of the solution.
- 2- The second group of methods uses non-smoothing regularization as the work done by Dias et al. (2009). The advantage of this group of methods is the sharp image of the subsurface, but it needs a high amount of *a priori* information.
- 3- The third group is called imaging methods. Fedi and Pilkington (2012) reviewed six of these methods. These methods are based on upward continuation of the data that are governed by depth weighting functions. The upward continuation operator is used because of its stability and the improved resolution compared to the other methods. This group of methods is non-iterative (the solution is achieved in one step), fast, and also the solution can be improved using derivatives. However, the produced subsurface images are smeared and diffused. Also, the performance of the method is reduced in case of non-isolated and non-compact subsurface bodies.

In general, the interpretation methods as stated by Barbosa and Silva (2011) “should not be viewed as competitive but as complementary”. This means that the different available methods are suitable in different situations. Automatic and Spectral methods are the most appropriate in case of lack or few *a priori* information. The inversion methods and forward modelling are more suitable in case of the availability of enough *a priori* information as geological maps, rock samples, drill holes and data from other

geophysical method. Another conclusion is that the forward modelling approach by Goetze et al. (1988) is the only work that implemented the object based approach. However, there is no work done to extract the objects from the 3D geophysical data and constrain the interpretation process according them to date

1.1.4. Solving the problem of non-uniqueness

The problem of the non-uniqueness of the potential field data was reduced in the exploration sector (Minerals, oil and gas exploration) by integrating other geophysical methods and borehole data. These studies had a depth extend up to 20 km. Seismic reflection profiles were usually used to construct subsurface models which were then forward modelled (Kaban, 2011, O'Brien et al., 2005). Also, borehole data, and measurements collected from surface samples were used to constrain the inversion of potential field data and especially in mineral exploration (Spicer et al., 2011a).

The same approach was applied in the regional studies (large spatial and depth extent up to several hundreds of km's) using gravity and seismological data. They used especially deep seismic profiles which provided estimates of the density distribution in the subsurface based on the velocity-density relationships. The estimated density distribution was used to calculate the corresponding gravity signal. Then, the misfit between the calculated and the measured gravity signal was minimized by adjusting the seismic derived density estimates (Bezada and Zelt, 2011, Hirsch et al., 2009, Ebbing et al., 2001). However, this work was done on profiles down to 60 km depth and not fully 3D. In case of satellite gravity data, the non-uniqueness was reduced usually using *a priori* information from the seismological data such as deep seismic profiles either reflection (Bezada and Zelt, 2011, Hirsch et al., 2009) or refraction (Tedla et al., 2011), seismic tomography models (Mishra et al., 2012, Cammarano et al., 2011), crustal thickness models derived from seismological data (Block et al., 2009), or receiver function analyses (Tedla et al., 2011, Mishra et al., 2012).

The main focus of the previous studies was mainly on the conversion of the seismological data into density which is not the optimum. This is due to the uncertainty in both seismic data and in the velocity-density conversion relationships because of the dependency on other physical parameters such as temperature, pressure and mineral composition (Bezada and Zelt, 2011, Cammarano et al., 2011). Ebbing et al. (2001) estimated the subsurface layers and objects based on the seismic tomography models and studies. Then, they used the object based forward modeling approach to estimate the optimum density contrast of the estimated objects. The estimation of objects' geometry and the density contrasts was based on trial and errors until they achieved the minimum misfit between the calculated and the measured gravity signal. However, there was not a defined methodology to extract the 3D subsurface objects from the 3D seismological data and use the settings of the extracted objects to constrain the interpretation process. This can reduce the uncertainty that can be introduced through the conversion process that requires several assumptions for different physical parameters such as temperature, pressure and mineral composition (Cammarano et al., 2011). Also, it can reduce the subjectivity in the object-based approaches that mainly depends on the user experience and decisions. Finally, the usage of the satellite gravity to verify and evaluate the extracted objects from the seismic tomography models can reduce the non-uniqueness in the 3D subsurface modelling using only seismic tomography models because of their low spatial resolution and the uncertainty in the inversion process (Adams et al., 2012, Rawlinson et al., 2010).

In this research, the problem of the non-uniqueness was targeted to be reduced using a state of the art 3D image processing technique called 3D Object Oriented Image analysis (3D OOA) that was applied to extract the 3D subsurface objects from 3D S-wave seismic tomography model of the study area. Before explaining the research objectives and methodology, a brief discussion about the work that was done to reduce the non-uniqueness problem by using image analysis techniques is given.

1.1.5. The role of image analysis techniques in potential field interpretation

Several image processing techniques were used to help in interpreting and extract the geological information from potential field data. For instance, image classification approaches were used to extract

information from geophysical data. Unsupervised ISODATA classification approach was used to classify a band combination of magnetic, apparent resistivity and gamma ray data in order to evaluate the zones with potential resources in the state of Alaska (Wiltse et al., 2009). Also, spatial (by convolution) and frequency domain (by Fourier transform FT) filters (Arisoy and Dikmen, 2011) were used for image enhancement and feature extraction as edge detection (Sertcelik and Kafadar, 2012) or lineaments extraction (Holden et al., 2012). Also, some processing approaches as cellular neural networks (Bilgili et al., 2005), wavelet analysis (Fedi et al., 2004), image fusion (Erkan et al., 2012), and principal component analysis PCA (Zhang et al., 2009) were used for geophysical data enhancement and interpretation. All of the above methods are pixel based approaches. However, the recent developments in object based approaches did not play a role in the analysing the geophysical data to date.

OOA is an image analysis technique that is based on the analysis of segments instead of pixel-by-pixel analysis (Blaschke, 2010). The segments are “regions which are generated by one or more criteria of homogeneity in one or more dimensions (of a feature space) respectively” (Blaschke, 2010). The use of segments gives the ability to simulate human cognition processes by using knowledge-based processing besides spectral features of the objects and context-dependent features such as texture, shape, and context to extract and classify objects in remote sensing data (Martha et al., 2011, Athellogou et al., 2007). Another important advantage of OOA is the ability to integrate different data from different sources (i.e. DEM, LiDAR, and Radar), which significantly improves the accuracy of the objects extraction (Blaschke, 2010). However, the selection of the appropriate segmentation algorithm from a broad range of segmentation algorithms is still a field of research. Moreover, the selection of the appropriate scale factor, shape and homogeneity parameters is still one of the challenges in OOA.

OOA started with the 2D classification then improved to 2.5D, and recently into 3D and 4D. In case of 2.5D OOA, a surface with a single value uses to extract a 2.5D shape of the objects (Strobl, 2008). DEM and LiDAR data were used, as examples, for extracting buildings (Dorninger and Pfeifer, 2008, Kim, 2011, Nguyen et al., 2012), forest structures (Maier et al., 2008), and urban vegetation areas (Hoeftle et al., 2012). In case of 3D OOA, the 3D object are extracted from the 3D image stacks (Rotarska-Jagiela et al., 2008, Schmidt et al., 2010), 3D voxels (Marschallinger et al., 2011), or LiDAR point clouds (Willhauck, 2012). 3D OOA was successfully used in the biomedical image analysis and proved a great ability in 3D objects extraction. For example, Schmidt et al. (2010) used 3D OOA to extract lymph nodes in their anatomical context from X-Ray computed tomography images (CT).

From the previous discussion the conclusion is:

Satellite gravity data, like any potential field data, suffer from the non-uniqueness problem. However, they can be very useful for the subsurface modelling because of the global coverage of the data and the spatial consistency. In the presence of constraints, satellite gravity can be used to model the density variation in the subsurface. 3D seismic tomography is an approach that can provide *a priori* information about 3D subsurface structures and bodies. However, 3D seismic tomography models need a method to extract the subsurface object from them in order to use them to constrain the modelling and the inversion process of the satellite gravity data. 3D OOA is a recent approach that can be used to extract the 3D objects from the 3D data. Consequently, it can be used to extract the objects from the 3D seismic tomography models in order to feed them to the modelling and the inversion process of the satellite gravity.

1.2. Problem Statement

During this research project, the non-uniqueness was targeted to be reduced using 3D OOA analysis of 3D seismic tomography models. In order to accomplish this, two problems were required to be solved. The first problem was the extraction of 3D objects from 3D geophysical data. The second problem was the usage of the extracted objects to reduce the non-uniqueness in the modelling and inversion process.

1- Extracting 3D objects from 3D subsurface data

The results of interpretation of subsurface data were usually visualized as:

- (i) depth slices (Wang et al., 2011),
- (ii) depth profiles (Wang et al., 2012),
- (iii) iso-surfaces (Boszcuk et al., 2011) or
- (iv) voxels (Spicer et al., 2011b).

However, objects extraction from 3D geophysical data is not a common approach. 3D Object Oriented Image Analysis (OOA) is an advanced image analysis technique that was used in this research to extract 3D objects from 3D geophysical data. In this research, 3D OOA was used to extract 3D subsurface objects from an S-wave seismic tomography model of the study area.

2- 3D constrained satellite gravity modelling and inversion

Satellite gravity interpretation suffers from non-uniqueness. Therefore, it needs *a priori* information that can be used to constrain the modelling and the inversion process. In this research, a 3D seismic tomography model was used to constrain the 3D modelling and inversion of satellite gravity data.

1.3. Research Objective

1. Extracting 3D objects from 3D geophysical data using 3D OOA.
2. 3D forward gravity modelling of the S-wave seismic tomography model based on the extracted objects through 3D OOA.
3. Adjusting the misfit between the forward modelled and measured satellite gravity signal.
4. Inversion of satellite gravity data using constraints based on the model output of the forward modelling stage.

1.4. Research questions

1. What is the capability of the 3D OOA to extract 3D objects from 3D geophysical data?
2. How will 3D OOA represent the fuzzy boundaries of geophysical subsurface bodies?
3. How can the S-wave seismic tomography model represent the density distribution in the subsurface?
4. What is the degree of the misfit? What is the effect of the low spatial resolution of the tomography model?
5. Can the forward model represent the regional gravity field of the study area?
6. How can the misfit between the calculated signal and the measured satellite gravity signal be adjusted?
7. How can the inversion of the satellite gravity data add to the 3D model of the study area?

1.5. Methodology

In this research project, the work flow was divided into three main stages (Figure 3):

1- 3D OOA:

In this stage, synthetic 3D subsurface models were used to test the capability of 3D OOA technique to extract the 3D subsurface objects out of them. Then, 3D OOA was used to extract the 3D objects from real 3D models of the study area.

2- Forward modelling (including object based inversion):

This stage mainly depended on the output of 3D OOA stage. The classified objects derived through 3D OOA were used in the forward modelling process. The model was constructed based on 3D OOA results then the objects' density contrasts were calculated using object based inversion technique. The forward modelling process aimed to compare the modelled gravity signal based on 3D OOA analysis with the measured satellite gravity signal.

3- Constrained inversion:

This stage used the model of the forward modelling stage to constrain the inversion process. It aimed to reduce the misfit between the measured satellite gravity signal and the calculated signal. Also, it aimed to enhance the details in the 3D model of the study area.

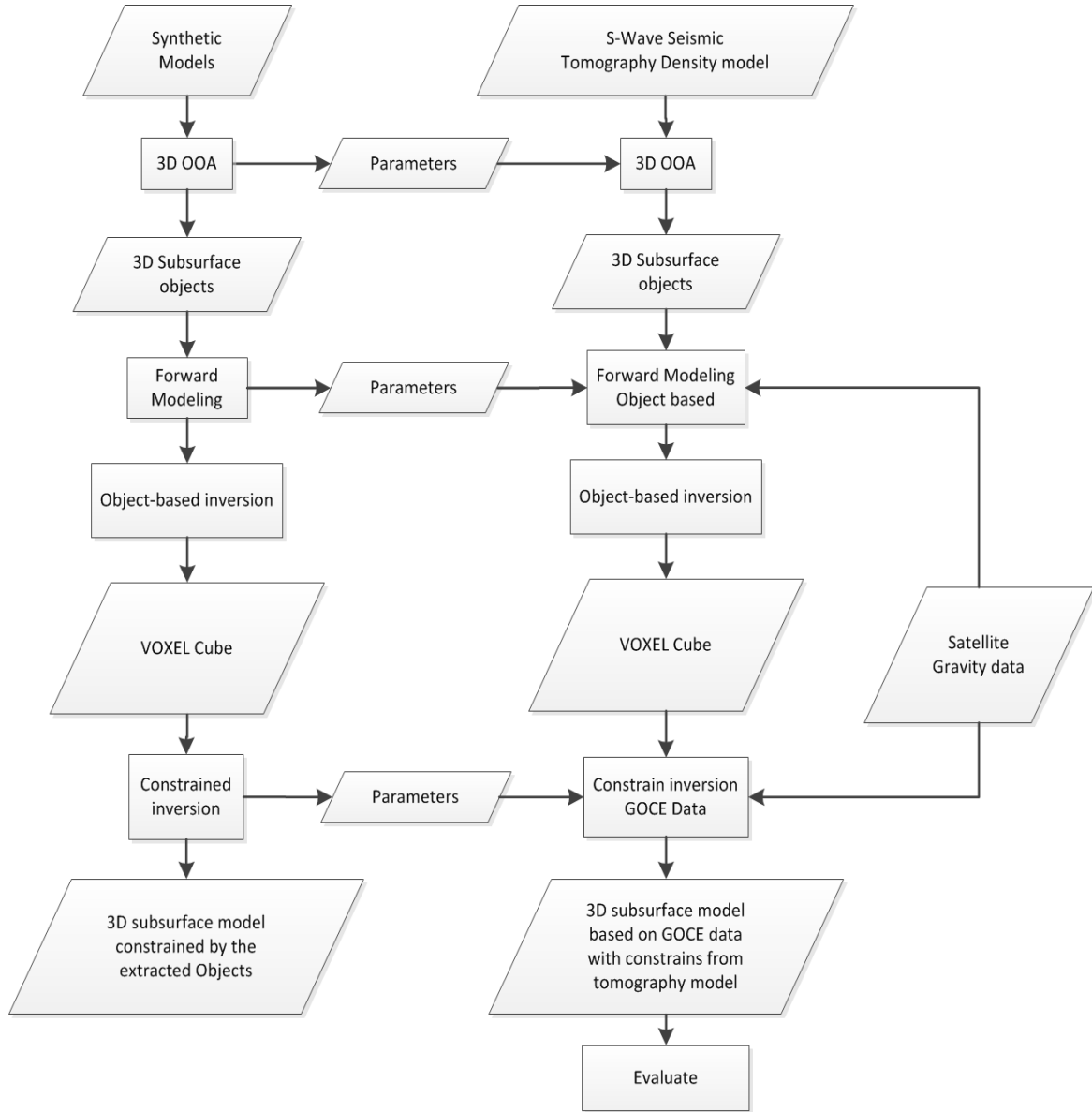


Figure 3: Flowchart describing the methodology of the research.

1.6. Thesis Structure

Chapter 1: includes brief background, problem definition, research objective, research question, and brief description of the study area.

Chapter 2: includes a detailed description for the study area and datasets.

Chapter 3: includes a detailed explanation for the methodology.

Chapter 4: includes the results of both synthetic and real data with discussion of the results.

Chapter 5: includes the conclusion and the recommendations for the future research.

2. STUDY AREA AND DATASETS

The study area lies in the central portion of the East African Rift System (EARS) between 1 to -11 N latitude and 28 to 39 E longitude. It mainly includes Tanzania, Rwanda, Burundi and small portions from the Democratic Republic of the Congo, Zambia, Angola, and Malawi (Figure 4).

The EARS is a significant part of the African superswell that is one of the largest topographic anomalies on the Earth. The area mainly consists of the Archean Tanzania Craton that is surrounded by the Eastern and Western branches of the rift system. The craton is also surrounded by Proterozoic mobile belts and volcanic activities (Cahen, 1984, Kampunzu et al., 1998).

2.1. The tectonic configuration in the study area

Several seismological studies addressed the main tectonic configuration of the area (Last et al., 1997, Julià et al., 2005, Ritsema et al., 1998, Owens et al., 2000, Huerta et al., 2009, Walker et al., 2004). Also other geophysical methods were used to define the tectonics of the study area such as the work done by Simiyu and Keller (1997) who used gravity data to model the long wavelength anomalies in the study area.

In this study we used the 3D shear wave tomography based model of the area produced by Adams et al. (2012). The model was able to address the tectonic settings of the study area using data of 182 seismic events and their records from several sources including stations from the Global Seismic Network, the Africa Array permanent seismic network, the Africa Array East African Seismic Experiment (Phase 1 and 2), and the Tanzania Broadband Seismic Experiment TBSE (Figure 5).

The data were inverted first for the Rayleigh wave phase velocities using the two plane approximation method (Forsyth and Li, 2005). Then, the phase wave velocities were inverted using (Park et al., 2008) to obtain a quasi 3D shear wave velocities model for the East African Upper Mantle.

The shear wave velocity model was used after that by Cammarano (2013) in currently on-going research to produce the 3D P-wave, density and temperature models of the study area. The 3D physical properties distribution in the subsurface of the study area based on seismic tomography models and the density, temperature, reflects the presence of different tectonic settings as discussed above.

The subsurface models can be divided into two main parts as mentioned in Adams et al. (2012). The first part (0 to ~200 km depth) contained the lithosphere which included the Tanzania Craton, rift branches, basement complex, fold belt and volcanism. This part was characterized by the velocity contrast between the high velocity/density of the Tanzanian Craton and Ugandan basement complex and, on the other hand, the low velocity /density of the surrounding tectonic settings as rift branches, Ruwenzori fold belt

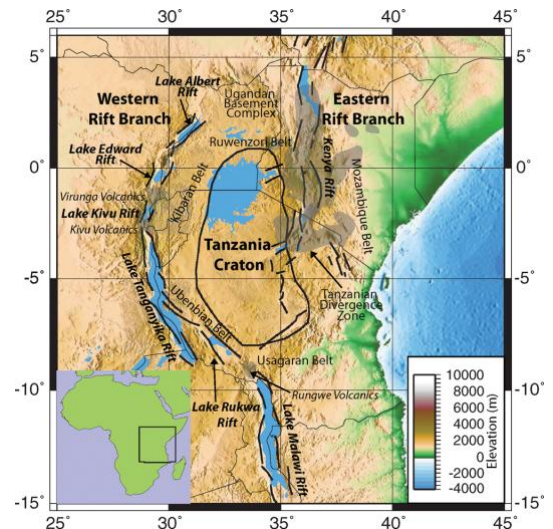


Figure 4: the study area with the major Cenozoic rift faults drawing in black lines (Adams et al., 2012).

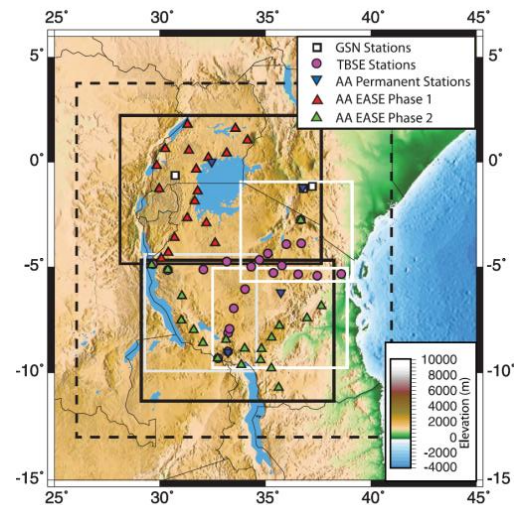


Figure 5: The distribution of the seismic stations (Adams et al., 2012).

and Cenozoic volcanisms. The second part of the 3D subsurface model was from ~200 to ~400 km depth. This part was related to the upper mantle which was mainly dominant by the low velocity/low density anomaly that relate to the existence of the plume. The plume was interpreted as a head plume or part of the deep mantle super plume in the western Africa as mentioned in Figure 6.

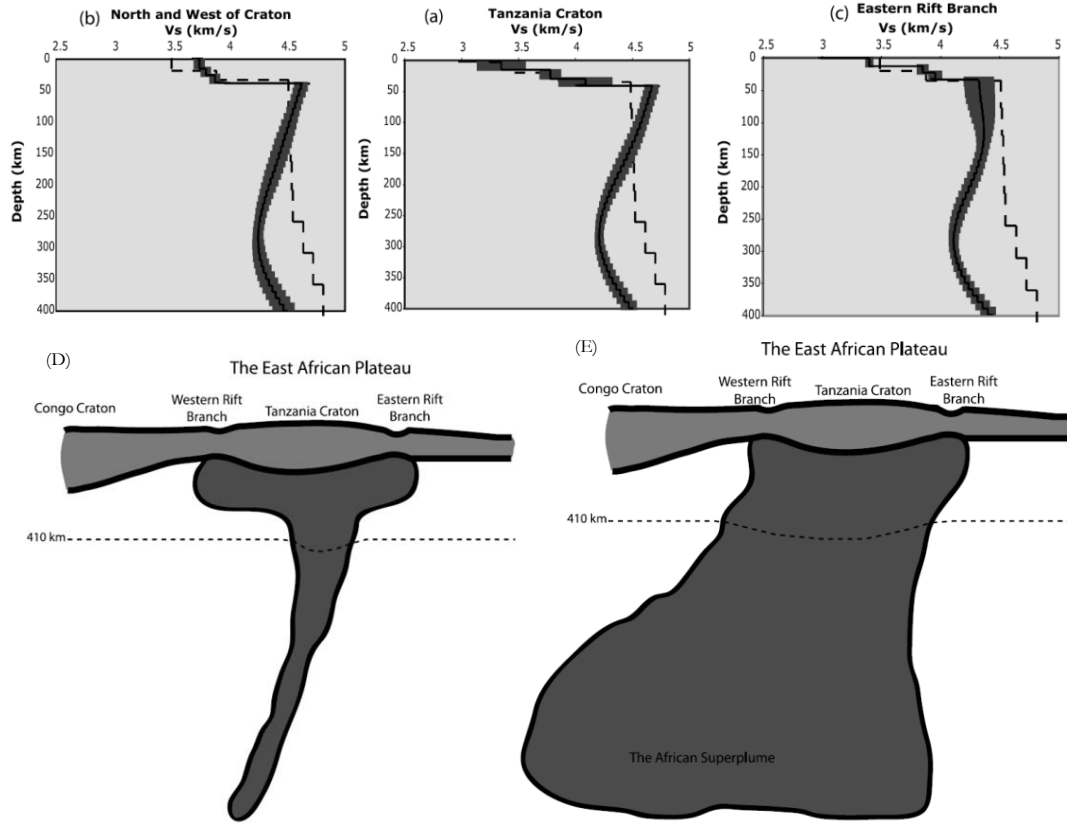


Figure 6: A), B), and C) The average shear wave velocity of the geological regions within the study area. D) and E) the recommended models of Adams et al. (2012) seismic tomography model interpretation

Each of the subsurface structures has its own certain characteristics in the 3D models as described in Adams et al. (2012). All details on these specific characteristics are described below.

2.1.1. Tanzania Craton:

The term craton was used to distinguish an old stable part of lithospheric continent from the other active and unstable regimes that subjected to consequence cycles of merging and rifting. The Tanzania craton consists of granites and greenstones. It has an elevation of ~ 1200 m and approximately dimensions of 1000 km by 500 km, and it was formed since, at least, 2.5 Ga. The 3D subsurface models of the study areas showed that the craton had the fastest (up to 4.65 km S⁻¹) values in the upper part from 0 to ~200 km as shown in Figure 7. The craton is surrounded by Proterozoic mobile belts (Figure 4 and Figure 7). The Ubendien Belt to the southwest of the craton is the oldest since it was formed around 2.0 and 2.1 Ga. To the west of the craton, the Kibaran Belt was fomed since 1.3 Ga. To the east and southeast of the craton, the Mozambique Belt was formed between 570 Ma and 1.2 Ga. The Proterozoic Belts show the same high velocity anomalies as the craton.

2.1.2. The Ugandan Basement Complex:

The Ugandan basement complex consists of migmatitic gneisses and granulites with uncertain age that range between 1.8 and 2.5 Ga. The relation between the Ugandan basement complex and the Tanzanian craton is not well documented. However, they were regarded as two cratonic blocks that are separated by Ruwenzori fold belt which shows a thinning in the lithosphere with about 25 km and thrust over the two

blocks. The same high velocity anomaly of Tanzanian Craton existed within Ruwenzori belt and Ugandan basement complex as shown in Figure 7.

2.1.3. The Rift Branches

The East African Rift System EARS is bifurcated around the Tanzanian Craton into the Eastern branch and the Western branch. The Eastern branch consists of several rifting segments that trend N-S called the Kenya rift. The Eastern rift branch becomes wide in northern Tanzania due to a 300 km faulting block called the northern Tanzania divergence zone. The Western Branch consists of several rifts that are the Ugandan rift (consisting of Lake Albert and Lake Edward rifts), the Lake Kivu rift, the Lake Tanganyika Rift, the Lake Rukwa Rift, and the Lake Malawi Rift.

The shear wave velocities showed low velocities beneath the two rifts branches. The velocity reduction was more beneath the eastern branch rather than the western branch. This anisotropy was related to that the eastern branch was more active than the western branch. The velocities in the upper 150 km were 8% slower than the velocities of the Tanzanian craton and reached 4.15 km s^{-1} at the Kenya rift (Figure 7).

2.1.4. The Plume:

Mantle plumes are defined as localized upwelling current of solid rocks that are hotter, thus less dense, than the surrounding Mantle. The second part of the 3D subsurface model (~ 200 to ~ 400 km) was dominant by a mantle plume. It was explained by the large low velocity anomaly that started at ~ 200 km depth as shown on the 250 km depth slice and in the cross sections Figure 7.

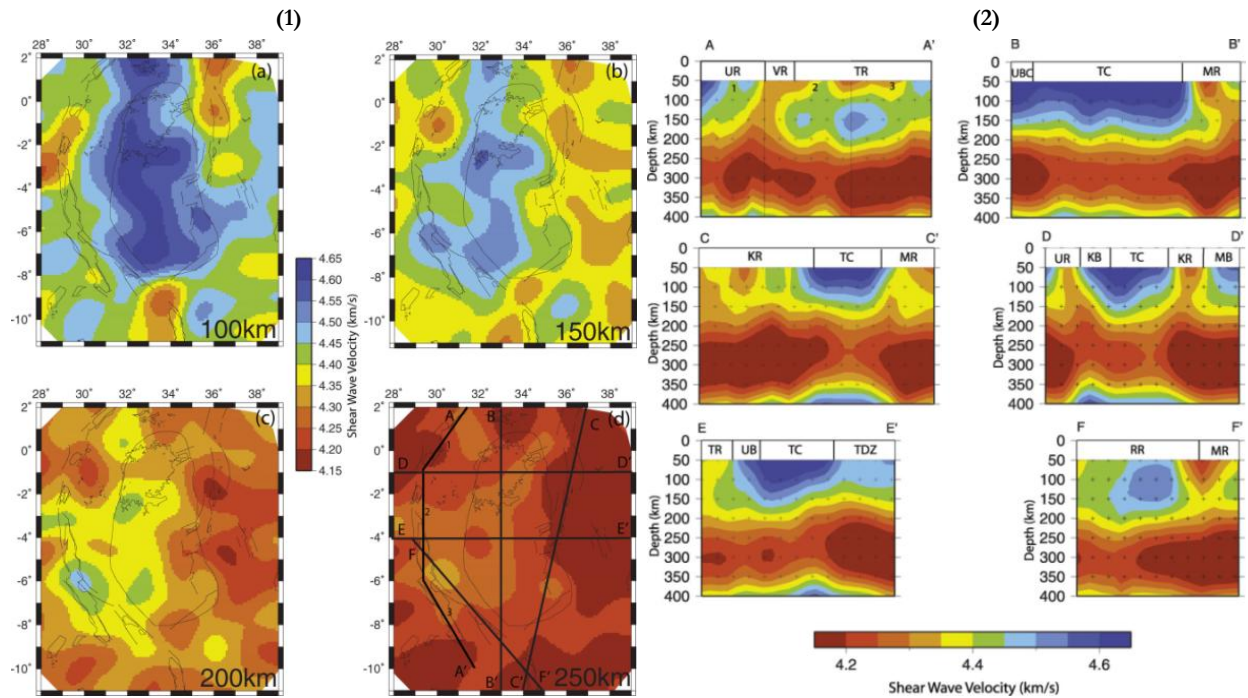


Figure 7 Adapted from Adams et al. (2012):

- 1) Shear wave velocity maps at selected depths from the 3-D shear wave model. Locations for the cross-sections are shown on the 250 km depth slice (d). Rift faults and craton boundary are the same as shown in Figure 4.
- 2) The cross-sections are indicated on the 250 km slice. Eastern rift branch: KR, Kenya Rift; TDZ, Northern Tanzania Divergence Zone. Western rift branch: UR, Ugandan Rifts; VR, Kivu Rift; TR, Tanganyika Rift; RR, Rukwa Rift; MR, Malawi Rift; UBC, Ugandan Basement Complex; TC, Tanzania Craton; The Proterozoic mobile belts: KB, Kibaran Belt; MB, Mozambique Belt; UB, Ubendian Belt.

2.2. Dataset

The dataset can be divided into three categories. First, the synthetic models and it was explained in details later. Second, 3D and 2D data sets that were explained here:

2.2.1. S-wave seismic tomography and density models

Seismic tomography is an established approach that can provide information about the 3D subsurface seismic velocity distribution from earthquakes data (Nolet, 2011). The velocity distribution in the subsurface can be converted into density distribution (Brocher, 2005, Ebbing et al., 2001) that can be used directly to forward model the gravity signal. Consequently, the calculated gravity signal from the forward modelling can be compared with the measured satellite gravity signal. Finally, adjustments to the forward model can be applied in order to reduce the misfit between the calculated and the measured signal.

The seismic tomography model of the study area (Adams et al., 2012) had a spatial resolution of 0.5 degree in the horizontal plane and a resolution of 10 km in the vertical direction. The model started at depth 40 km and extended until 400 km (Figure 8 (A)). It did not include the shallow part since the vertical resolution 10 km did not allow to show the shallow structures since they needed a small depth interval (can be 5 or 1 km). The model defined the regional setting of the study area. The shear wave velocity uncertainty was around 0.2 km s⁻¹ for depths shallower than 250 km and around 0.3 km s⁻¹ at greater depths. The depth uncertainties in the main features were in order of + 25-50 km at shallow depths and in order of + 75-100 km deeper in the upper mantle (Adams et al., 2012).

Then, the model was converted by Cammarano (2013) into density (Figure 8 (B)), temperature and P-wave velocity model. The produced models had the same spatial resolution as the S-wave seismic tomography model. However; the details about the uncertainty in the seismically derived density model were not available since the work still in progress.

2.2.2. Satellite gravity data

The idea for satellite gravity measurements was triggered after the success of the Radar Altimeter measurements. The first completed Radar Altimeter image of the sea and ocean surfaces, which was provided by Seasat in 1978, completely changed the understanding of the geophysicist and the geodesists to the tectonic processes. The Radar altimeter measurements provided the scientific community with valuable information about the earth interior. (Nabighian et al., 2005). From this, the sea-surface topography from radar altimeter data was used to calculate the vertical component of the gravity field. This significantly helped in improving the knowledge of the earth's tectonic (Hwang et al., 1998, Sandwell and Smith, 1997). Consequently, the gravity field measurements were moved from only calculating the marine gravity field from radar altimeter measurements to measuring the global gravity field using new satellite missions. This step led to improving the quality of the available data and also improving our understanding of the overall earth tectonic history (Loekken, 2012a, Tapley and Kim, 2001).

The EIGEN-6C gravity field model (Barthelmes et al., 2011) was used in this research. The model is a combined gravity field model of LAGEOS/GRACE, GOCE and DTU10 global gravity anomaly grid of a maximum degree 1420. The model is recent and showed an improvement over the previous models. The model consists of a combination of different satellite gravity measurements (e.g. GRACE and GOCE) with terrestrial data. The model accuracy is higher than the older models. The model accuracy was evaluated by comparing the heights derived from the model and the geoid heights derived from the GPS/Leveling measurements all over the world. However, a new version of the model, eigen-6c2 that released in December 2012 showed more accuracy than the eigen-6c. The free-air and geoid anomalies grids were available on the International Centre for Global Earth Models (ICGEM) web site (<http://icgem.gfz-potsdam.de/ICGEM/>).

2.2.2.1. Preparing the gravity data

The satellite gravity data needed to be prepared to use them in the inversion process. The free air satellite gravity measurements for the study were downloaded with a resolution of 0.25 degree (Figure 8 (C)). Then, they were corrected for the terrain effect. The effects of the nearby topography were removed using the ETOPO topography data (Figure 8 (D)) available through the GFZ website (<http://icgem.gfz-potsdam.de/ICGEM/>). The effect of the terrain correction on the satellite gravity measurements was small with a maximum value of 3.16 mGal (Figure 8 (E)), which was also mentioned in Mishra et al. (2012). Then, the data were corrected for the mass excess or deficiency due to high or low elevation from the mean sea level. The Bouguer correction used also the ETOPO topography data with the same spatial resolution (0.25 degree) of the satellite gravity data (Figure 8 (F)).

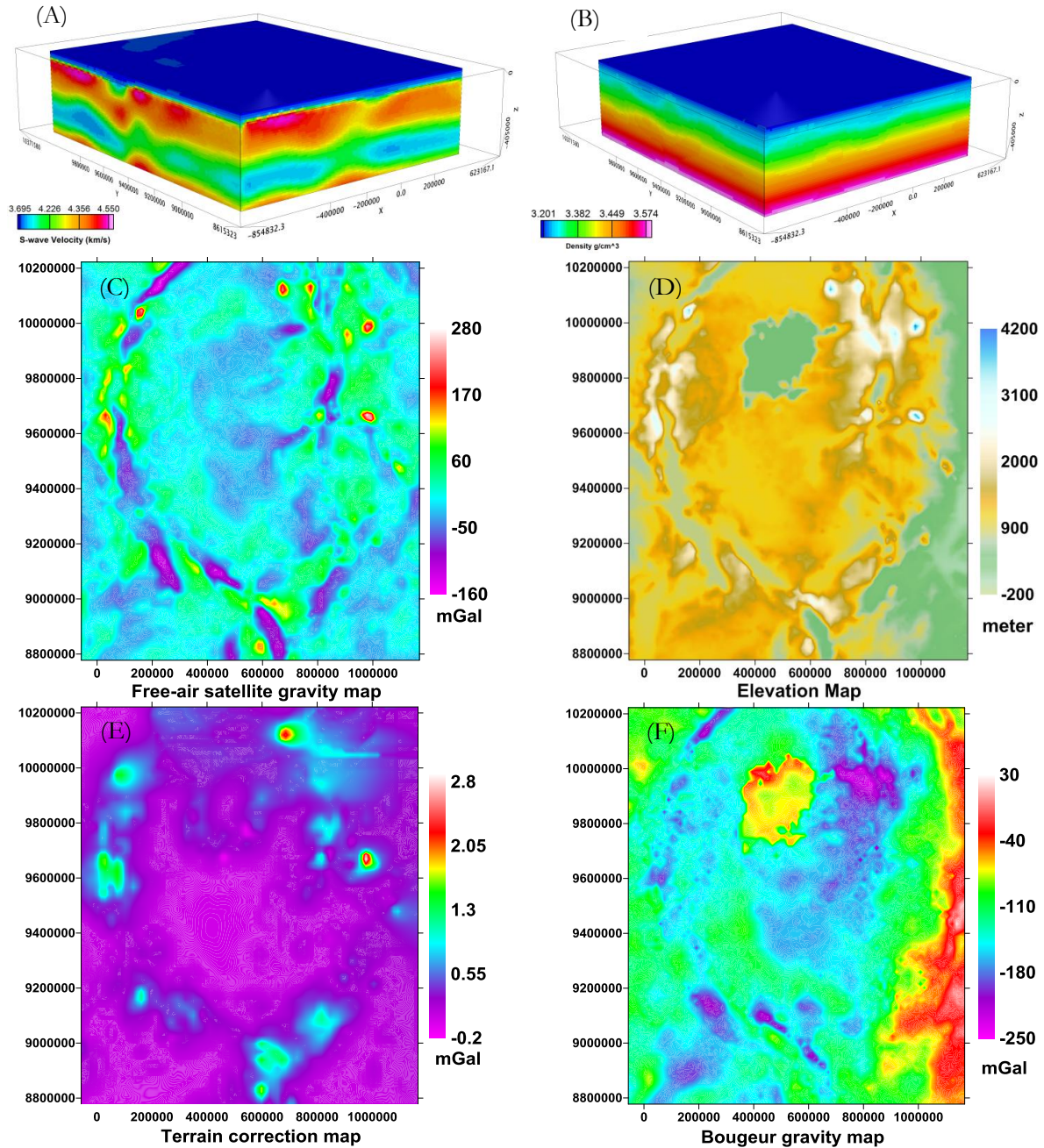


Figure 8: A) The S-wave seismic tomography model of the study area was adapted from Adams et al. (2012). B) The density model was derived based on the S-wave seismic tomography model adapted from Cammarano (2013). (C) The free-air satellite gravity signal of the study area from Eigen-6c model. (D) The topography of the study area ETOPO model. (E) The terrain correction of the free air data using ETOPO topography. (F) The Bouguer anomaly map based on the terrain correction.

2.3. Synthetic models

After the tectonic settings of the study area were studied, two groups of density synthetic models were created. These two groups were created to test the work flow of the methodology that included 3D OOA, forward modelling and constrained inversion. The first group of the synthetic models contained a simple single object in homogenous background. The second group contained more complex models than the simple models group. These models aimed to simulate the real situation as much as possible. Moreover, they aim to study the difficulties in dealing with multiple objects in the same model.

2.3.1. The simple models

Five simple models were created to simulate the objects in the study area. The rift branches were simulated by a vertical object. Whereas, the craton were simulated by box, cylinder and sphere models in order to determine the effect of the shape on the interpretation techniques. The boundary between the plume and the upper lithospheric objects was simulated by 2D simple surface.

	Length along X (km)	Length along Y (km)	Thickness along Z (km)	Depth to top (km)	Density Contrast (g/ cm ³)
Vertical Object	8	0.5	6	0.5	0.4
Sheet Object	8	8	0.5	0.5	0.4
Box Object	4	4	6	0.5	0.4
Cylinder Object	4(diameter)	4(diameter)	6	0.5	0.4
Sphere Object	4(diameter)	4(diameter)	4	0.5	0.4

Table 1: The detailed description of the simple synthetic models.

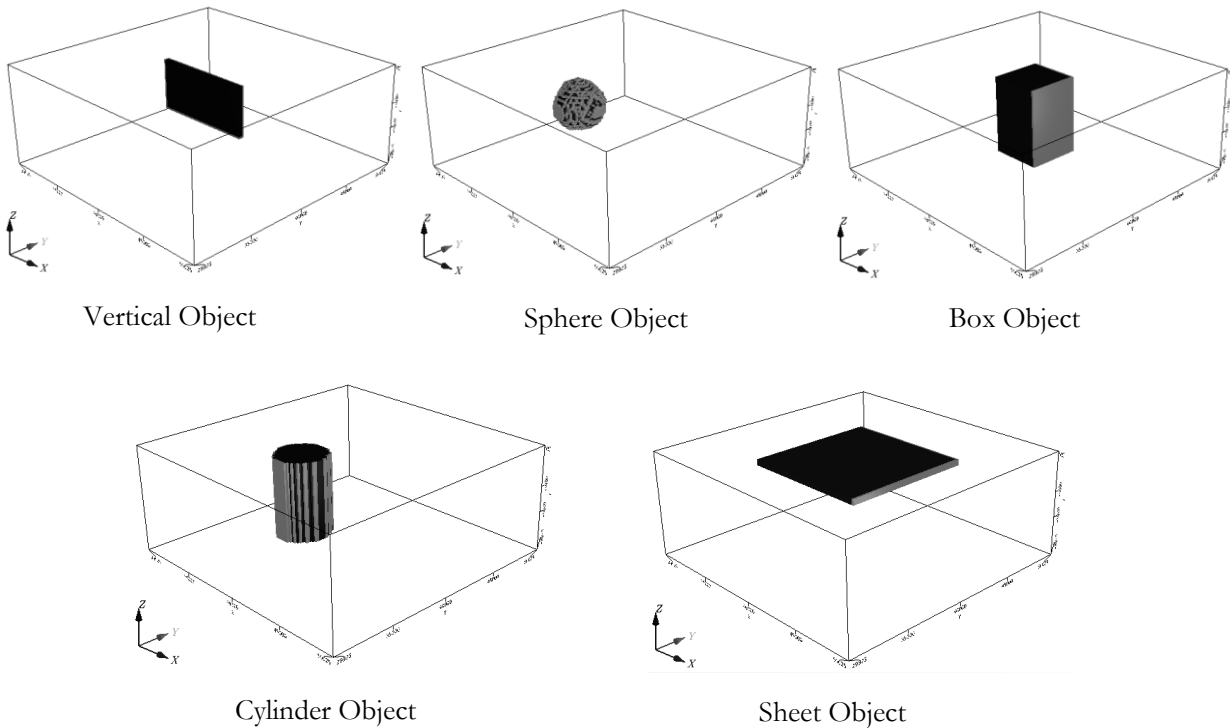


Figure 9: The synthetic models described in Table 1.

2.3.2. Complex models

Two complex models were created to simply simulate the configuration of the study area. They were created to test the capability of the methodology workflow.

2.3.2.1. Model 1 – no vertical variation

The first model was a simple combination of the objects that represent the tectonic settings in the study area. It contained two vertical objects to represent the two rift branches, cylinder object in the middle to represent the craton, and a layer underlying these objects to represent the plume. Three transition zones were added, between each object and its neighbourhood, to represent the change in the density values between them (Table 2 and Figure 10).

	Length along X (km)	Length along Y (km)	Thickness along Z (km)	Depth to top (km)	Density (g/ cm ³)	Density Contrast (g/ cm ³)
Vertical Objects (Rifts)	1	6	~3	0.0	2.0	-0.4
Cylinder Object (Craton)	4	6	~3	0.0	2.3	-0.1
Background Layer	Surrounding the rifts, Craton, and the plume				2.4	0
Underlying Layer (Plume)	10	10	~2	4	2.1	-0.3
The vertical boundaries (between the background and the vertical object)	0.2	6	~3	0	2.15, 2.1, 2.05	0.25, 0.2, 0.15
The vertical boundaries (between the vertical object and the Craton)	0.2	6	~3	0	2.05, 2.15, 2.25	0.35, 0.25, 0.15
The horizontal boundaries (Between the above objects and the plume)	10	10	0.2	3.4, 3.6, 3.8	2.25, 2.2, 2.15	0.15, 0.2, 0.25
The reference density	2.4 g/ cm ³					

Table 2: The detailed description of the first complex model.

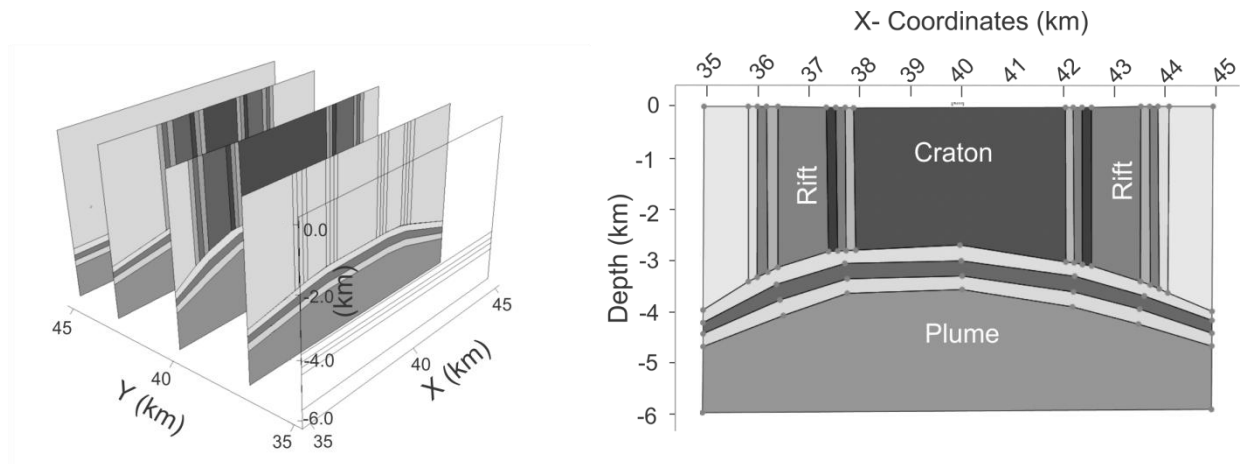


Figure 10: the first complex synthetic model

2.3.2.2. Model 2 – depth varying densities

In the second model more complexity was added to the model by adding three layers that had density values increasing with depth. The model was divided into the two vertical objects, the cylinder object, the three transition zones, and the background into three layers that had density values increasing with depth. In addition to this, the values of the density contrast were the same in different parts of the different objects. This made the object extraction process based on the density values more difficult than the previous model (Figure 11 and Table 3).

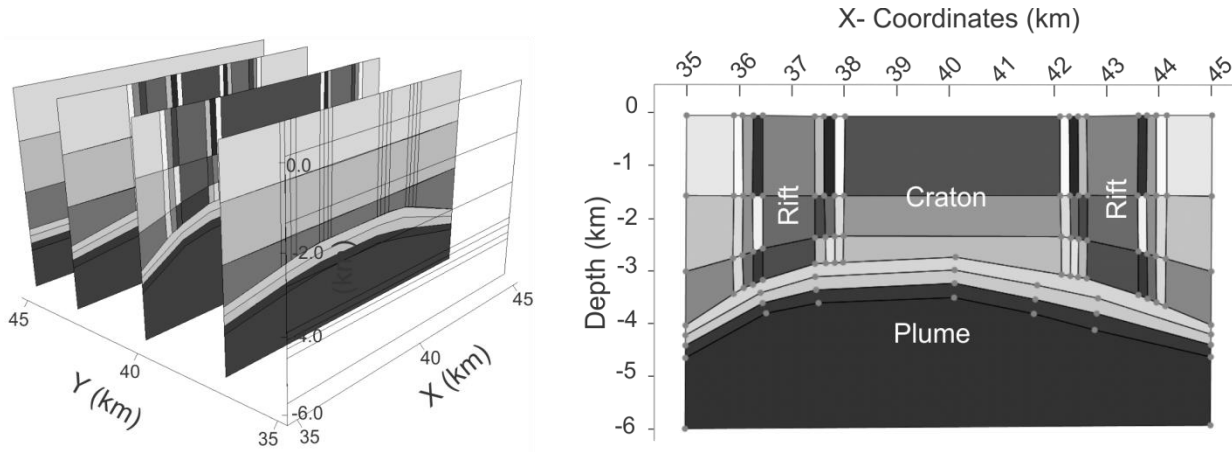


Figure 11: The second complex model.

	Length along X (km)	Length along Y (km)	Thicknes s along Z (km)	Depth to top (km)	Density in Layer 1 (g/ cm ³)	Density Contrast (g/ cm ³)	Density in Layer 2 (g/ cm ³)	Density Contrast (g/ cm ³)	Density in Layer 3 (g/ cm ³)	Density Contrast (g/ cm ³)
Vertical Objects (Rifts)	1	6	~3	0	2.1	-0.125	2.2	-0.025	2.3	0.075
Cylinder Object (Craton)	4	6	~3	0	2.5	0.275	2.6	0.375	2.7	0.475
Background Layer	Surrounding the rifts, craton, and the plume				2.3	0.075	2.4	0.175	2.5	0.275
Underlying Layer (Plume)	10	10	~2	4	2.5					0.275
The vertical boundaries (between the background and the vertical object)	0.2	6	~3	0	2.25	0.025	2.35	0.125	2.45	0.225
					2.2	-0.025	2.3	0.075	2.4	0.175
					2.15	-0.075	2.25	0.025	2.35	0.125
The vertical boundaries (between the vertical object and the Craton)	0.2	6	~3	0	2.2	-0.025	2.3,	0.075	2.4	0.175
					2.3	0.075	2.4,	0.175	2.5	0.275
					2.4	0.175	2.5	0.275	2.6	0.375
The horizontal boundaries (Between the above objects and the plume)	10	10	0.2		3.4	2.5				0.275
					3.6	2.4				0.175
					3.8	2.3				0.075
The reference density	2.225 (g/ cm ³)									

Table 3: The detailed description of the second complex model.

In this chapter, the study area and the datasets were explained. The study area was explained based on the literature. The subsurface structures in the study area were explained as objects with specific characteristics which fit with the scope of this research. The datasets can be divided into 2D and 3D data. The 2D data are the gravity signal and the elevation map while the 3D data are the seismic tomography and density models including the synthetic models.

3. METHODOLOGY

The methodology can be divided into three stages: 3D OOA, forward modelling including object based inversion, and constrained inversion. These three stages were applied on the synthetic models in the beginning in order to define the capability of the methodology workflow. Then, they were applied on the real datasets. In this chapter, the three stages are explained by explaining the purpose, the software, the concept, the used datasets and the expected output of each stage.

3.1. The first stage: 3D OOA

3.1.1. Purpose

The purpose of this stage was the extraction of the 3D subsurface structure configurations from the 3D geophysical data in the form of objects.

3.1.2. Datasets

3D cubes of the 3D subsurface objects were used as the input for this stage. However, in order to use these 3D objects for the purpose of 3D OOA, these objects were required to be converted into 3D image stacks. The 3D image stacks are a series of images that are arranged according to their vertical location. Therefore, the 3D objects, represented as 3D voxel cubes, were converted to slices, gridded using Kriging (Oasis Montaj, 2010), and were then converted into 3D image stacks (APPENDIX 2).

Another issue related to the 3D image stacks was the colour scheme that would be used to describe the density distribution in the image. The “rgbgrey” colour scheme of Oasis Montaj 7.5 software (Oasis Montaj, 2010) was used for the 3D image stack (Figure 12). This means that the maximum density contrast was assigned the black colour and ranging, using linear colour distribution method, until white that corresponded to the minimum density contrast.

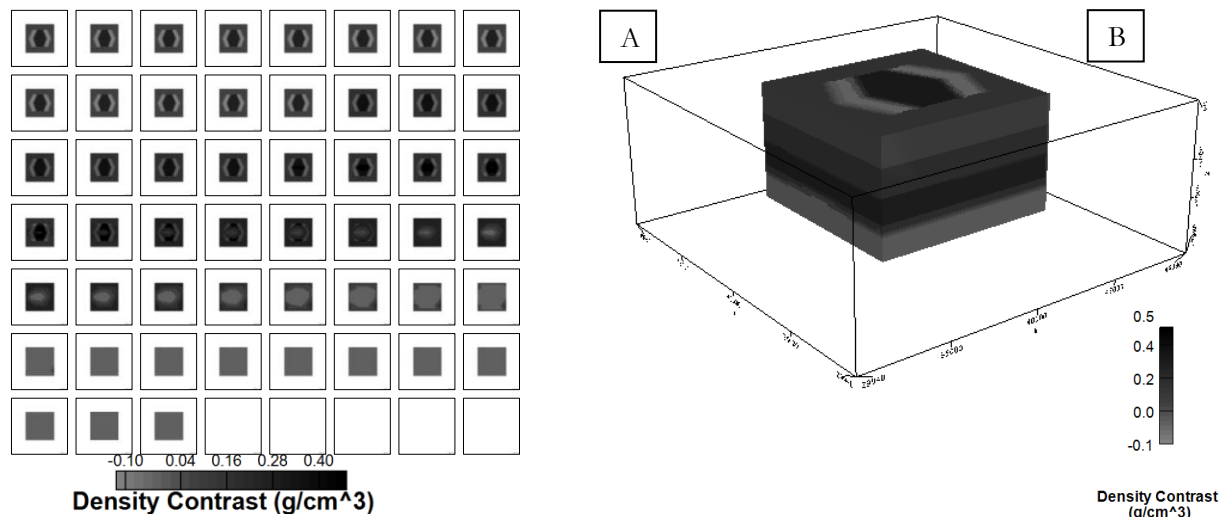


Figure 12: (A) the 3D image stack of the second complex model represents in the ‘rgbgrey’ colour scheme start at the top left the first slice with depth zero moving with depth interval 125 m to the end of the first row slice number 8 then moving to the next row and continue in the same way to the bottom left end slice number 56. (B) The voxel cube of the same model in ‘rgbgrey’ colour scheme on the left.

3.1.3. Software

eCognition 8.7 software was used for the 3D OOA analysis. eCognition was released in 2000 as the first commercial OOA software. The software is one of the powerful tools for OOA since 50-55% of OOA

scientific articles used it (Blaschke, 2010). The software allows the handling of 2D, 3D and 4D data (eCognition Developer, 2011).

3.1.4. Methodology

Any OOA procedure in eCognition is based on rulesets. A ruleset is a series of commands that apply a number of algorithms in a certain sequence with the purpose of extracting and classifying objects from the images. 3D OOA ruleset can be divided into 4 main steps:

- 1- The segmentation process: in which the image pixels were grouped into homogeneous segments based on certain criteria that were fed to the algorithm by the user or automatically.
- 2- The analysis step: in which the images were analysed to determine the features that can be used in the classification process. These features can be based on spectral, spatial, context, or texture characteristics of the objects in the images.
- 3- The classification process: in which the objects were assigned to their classes based on the analysis from the previous step.
- 4- The refining and exporting stage: in which the classification results were refined and the misclassified small segments were corrected. Finally, the exporting process in which the output from the OOA was exported into a suitable format to the next stage in the analysis.

3.1.5. Expected outputs

The expected outputs were 3D objects and 3D classified images that were used to build models in the next forward modelling stage.

3.2. The second stage: Forward modeling (including object based inversion)

3.2.1. Purpose:

The purposes of this stage were calculating object density contrasts, and evaluating and adjusting the model output from the 3D OOA stage. This was accomplished by:

- 1- Building models using depth slices and cross sections of the extracted 3D objects.
- 2- Calculating the objects' density contrasts using the object based inversion technique (Haase (2008) in Schmidt et al.(2011)). The technique uses least square estimations to calculate the objects density contrasts'. These density contrasts contribute to a calculated gravity signal that has the minimum misfit with the measured gravity.
- 3- Calculating the forward gravity signal and compare it with the measured satellite gravity. Based on the degree of misfit between the calculated and the measured gravity signal one can judge on the accuracy of the 3D OOA process.

3.2.2. Datasets

Three different datasets were used in this stage.

- 1- The 3D objects and 3D classified images output from 3D OOA were converted into 2D depth slices and cross sections to use them in this stage. The reason is the limitation in the forward modelling software IGMAS+ since the software does not allow to import 3D objects. The software allows importing depth slices, cross sections or voxels. Consequently, the 3D objects and 3D classified images were converted to depth slices and cross sections to use them as a guide to rebuild the model in IGMAS+.
- 2- The measured satellite gravity signal was compared with the calculated gravity signal output from the constructed 3D forward model in order to evaluate the reconstructed model.
- 3- The topographic map of the study area.

3.2.3. Software

3D Interactive Gravity and Magnetic Application System (IGMAS+) software was used in this stage. The software is an object-based 3D modelling software and uses triangulated polyhedrals to construct 3D subsurface bodies. The software calculates the forward signal based on the analytical solution of the volume integral of the 3D polyhedral homogenous body that was transformed into a surface integral (for more details about the mathematical background the reader can refer to Goetze and Lahmeyer (1988)).

The most powerful advantage of using the triangulated polyhedral approach is the possibility to easily doing geometric changes in the 3D model, after building it, and directly updates the forward gravity signal. This is possible because the algorithm was designed to update the calculated gravity signal in the region where only the triangulation change. This direct response for modifications in the model allows the user to make the required adjustment until he gets the best fit. However, the process of model reconstruction is time consuming (for more details about the advantage and disadvantage in comparison with the other approaches, the reader can refer to Schmidt et al. (2011)).

Another important feature in the software is the object based inversion approach. It is possible to apply the object based inversion algorithm on triangulated bodies in order to get the optimum density contrasts values. The density contrasts values output from the object inversion process can accomplish the best fit between the calculated and the measured gravity signal instead of trial and error approach. The inversion algorithm is mainly based on the linear inversion minimum mean square error algorithm that was introduced by Haase (2008) in Schmidt et al.(2011).

In this research, the density contrasts were used instead of the absolute density values. The reason is the limitation in IGMAS+ that allows only using one absolute density value as a background. However, in case of deep studies ($\sim >40$ km depth), the background density values change with depth. Consequently, including these different absolute background density values were not possible in IGMAS+. Therefore, the density contrasts values were used instead of the absolute values. The density contrasts represent the deviation from the background density model. This background model is assumed theoretically to produce a gravity field without any anomalies. Therefore, the deviation from these background densities is assumed to produce the gravity anomalies in the gravity measurements. In the synthetic models, the background density was 2.4 g/cm^3 for the first complex model (Table 2) and 2.225 g/cm^3 for the second complex model (Table 3). In case of the real data, the background densities vary with depth. Ebbing et al. (2001) calculated a background density model to interpret their results. This model was based on the equation of Christensen and Mooney (1995) that converts the seismic tomography velocities into densities. They estimated the background model up to depth 180 km. Consequently, there were no available values for calculating the absolute gravity values of the deep part of the object based inversion results' as mentioned in Table 6.

3.2.4. Methodology

The forward modelling stage was accomplished in four steps:

- 1- Creation of an empty 3D mesh in IGMAS+, then importing the classified images and sections in their correct geo-referenced location.
- 2- Building of the model by drawing the different objects and bodies guided by the classified images and sections.
- 3- Applying the inversion approach to get the optimum density contrasts off the objects.
- 4- Calculating the forward gravity signal and compare it with the measured gravity.

3.2.5. Expected Outputs

The expected output from this stage was a 3D model in the form of a voxel cube. This model will then be used as a constraint for the inversion in the next stage.

3.3. The third stage: Constrained Inversion

3.3.1. Purpose

The purpose of this stage was the optimum modelling of the study area. In this stage, the satellite gravity data were used to enhance the details in the constructed model from the previous stage. The constructed model from the previous stage was used to constrain the inversion process. The inversion process aimed to enhance the details in the model. It calculates the distribution of the density within the objects. It also allowed calculating the density distribution in the shallow zone (0:40 km). This enhancement reduced the misfit between the established model in the previous stage and the satellite gravity measurements and especially the high wave number (shallow depth) anomalies.

3.3.2. Datasets

- 1- The extracted model from the forward modelling stage in the voxel format.
- 2- The measured satellite gravity signal.
- 3- The topography data.

3.3.3. Software

The University of British Columbia-Geophysical Inversion Facility's (UBC-GIF) GRAV3D was used in this stage. Among several inversion techniques, this technique was selected due to the well suited software package, the ability to add constraints to the inversion, the good results in different case studies, and the ability to get the full license for academic purposes.

Li and Oldenburg (1996, 1998) introduced the concept of the inversion approach for GRAV3D. The approach is based on discretizing the 3D subsurface model into cells using a 3D orthogonal mesh. Then, it uses the vertical gravity component to estimate the density contrast distribution in each cell within the model. The calculated density contrasts should produce the minimum misfit between the measured gravity signal and the calculated (forward) gravity signal out of the model according to the following equation,

$$\phi_d(m) = \phi - \phi_m(m)$$

$\phi_d(m)$: The data misfit associated with the model.

ϕ : The real data.

$\phi_m(m)$: The objective function that describes the model m.

However, infinite number of models can produce the desired degree of misfit. Thus, an objective function was used to constrain the shape of the estimated model according to the available *a priori* information that can be supplied to the solution as a reference model, bounds or as initial models. The used objective function is,

$$\begin{aligned} \phi_m(m) = & \alpha_s \int_V w_s [w_r(z)(m - m_{ref})]^2 dV + \alpha_x \int_V w_x \left[\frac{\partial}{\partial x} (w_r(z)(m - m_{ref})) \right]^2 dV \\ & + \alpha_y \int_V w_y \left[\frac{\partial}{\partial y} (w_r(z)(m - m_{ref})) \right]^2 dV + \alpha_z \int_V w_z \left[\frac{\partial}{\partial z} (w_r(z)(m - m_{ref})) \right]^2 dV \end{aligned}$$

Where,

$m - m_{ref}$: The deviation of the estimated model from the supplied reference model.

w_s, w_x, w_y, w_z : Spatially dependent weighting function where,

w_s : control the smallness (difference) between the reference model and the estimated model in any location.

w_x, w_y, w_z : control the smoothness of the spatial distribution of difference between the reference and the estimated model in the different X, Y and Z directions.

$\alpha_s \alpha_x \alpha_y \alpha_z$: Global weighting function that controls the relative importance of the above terms where, α_s for smallness, $\alpha_x \alpha_y \alpha_z$ for the smoothness. They can be input by the user via the Alpha weighting function

The potential field data have no inherent depth information (Williams, 2008, Li and Oldenburg, 1998), so a depth weighting function $w_r(z)$ was used to describe the decay of the kernel function for the surface gravity data with depth. In case of the presence of constraints or significant topography, a distance weighing function can be used in which the lateral variation is included as well as the vertical variation.

For more information the reader can refer to Li and Oldenburg (1996), Li and Oldenburg (1998) and Williams (Williams, 2008).

3.3.4. Methodology

The constrained inversion process can be divided into three steps:

- 1- The data preparation step: in this step the voxel model out of the forward modelling stage, the measured satellite gravity data were subjected to a MATLAB code (APPENDIX 3) in order to convert them in suitable format for use in GRAV3D.
- 2- Determination of the optimum inversion parameters: The optimum weighting parameters will be estimated through the literature review and the synthetic test.
- 3- Running the inversion process.

3.3.5. Expected Outputs

The expected output from this stage was an improved 3D subsurface model of the study area where the distributions of the density contrasts within the objects were enhanced.

In this chapter, the methodology was explained. The methodology can be divided into three stages. First, 3D OOA analysis of the 3D image stacks of the data in order to retrieve the subsurface structures. Second, the forward modelling stage including the object based inversion in which the models were reconstructed based on the 3D OOA results then the objects' density contrasts were estimated using object based inversion technique. Third and final, the constrained inversion stage in which the models output of the forward modelling stage were used to constrain the inversion of the gravity signals.

4. RESULTS AND DISCUSSIONS

In this chapter, the results and discussion of synthetic and real data are shown and explained. The synthetic models were used firstly to determine the capability of the whole methodology. Then, the methodology was applied on the real datasets. The results and discussions of the synthetic models are provided in the first two sections. Then, the results and discussions of the real data are provided in sections 4.3 and 4.4.

4.1. Synthetic modelling

4.1.1. Results 3D OOA

In the next two subsections, the 3D OOA analysis will be explained for both simple and complex models.

4.1.1.1. 3D OOA of the simple models

All the simple models were analysed using one simple ruleset. The ruleset consisted of three steps:

- 1- Automatic threshold algorithm: automatically calculates the threshold value of the background using an algorithm based on histogram based method and homogeneity measurements (eCognition Developer, 2011).
- 2- Multi-threshold segmentation algorithm: uses the value of the automatic threshold (or user defined threshold/s) to create segments that divide the image into two classes (or more) based on the threshold value. (eCognition Developer, 2011).
- 3- Convert image objects algorithm: connects and converts the objects segments extracted from the images in 3D (eCognition Developer, 2011).

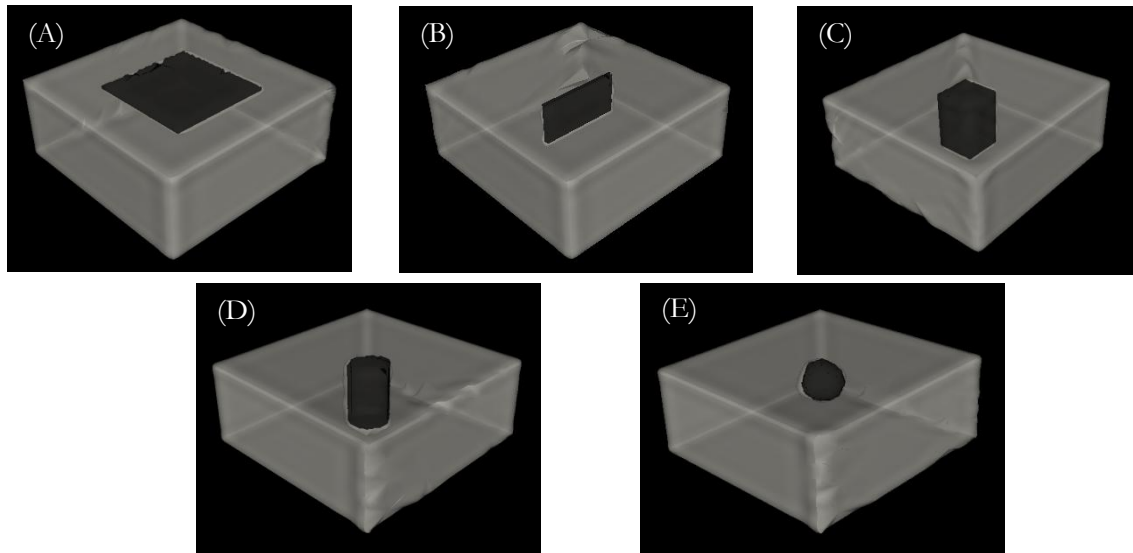


Figure 13: (A), (B), (C), (D), and (E) 3D OOA results for the simple synthetic models. F) Example of the image slices were used as input for 3D OOA of the box synthetic model.

As shown in Figure 13, the extraction and classification processes were done successfully. Five different objects were retrieved using 3D OOA (Figure 13 (A)-(E)). The objects represented different shapes and potential problems in retrieval (round edges, sharp edges, volumes or sheets, etc.). All objects were defined crisp and no noise was added. The five different objects were equally well retrieved. Independent if they are sphere, sheet, square or cylinder, there is no limitation on the shape with respect to the quality and completeness of the retrieved synthetic object.

4.1.1.2. 3D OOA of fuzzy boundaries model:

The previous test was done on objects with crisp boundaries. Although it served its purpose for the synthetic testing of the 3D OOA capabilities it is not realistic for real world subsurface objects. In this subsection, an experiment was done to test the capability of the 3D OOA to deal with the 3D fuzzy objects. Fuzzy boundaries were added to the simple cylinder synthetic models. Then, the model was subjected to the 3D OOA (Figure 14). The analysis was carried out using a simple ruleset that consists of:

- 1- Multi-resolution segmentation: is an algorithm that builds the segments starting by one pixel and then merges the neighbourhood pixels that only fit both spectral and shape homogeneity parameter of the algorithm. The parameters were: Scale parameter=1, Shape=0.1 and Compactness=0.1. The small values of the parameters were chosen to make the segmentation able to discriminate the small changes within the fuzzy boundary zone (Figure 14(A) and (B)). The large parameters could lead to miss the details within the object due to forcing the segmentation algorithm to produce large segments. These large segments could cause missing the details of variation within the fuzzy boundaries.
- 2- Classification: is an algorithm that evaluates the membership of the segments to the target class. A class with the name “object” was created to assign the cylinder object to it. A fuzzy membership function was used in the “object” class. The membership function defined the fuzzy boundaries of the simple cylinder objects (Figure 14(C)).
- 3- Convert image objects algorithm: convert the objects extracted from the images into objects connected in 3D (Figure 14(D)).

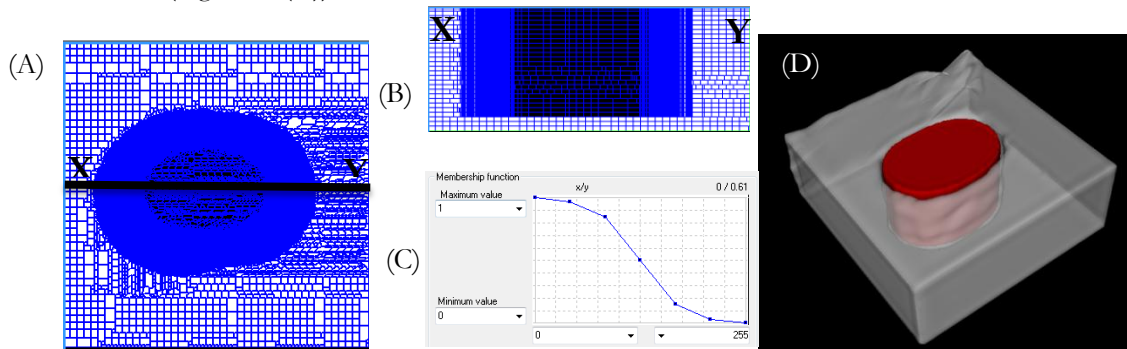


Figure 14: The process of extracting object with 3D fuzzy boundaries. (A) Figure shows the effect of the segmentation parameters on the segmentation process since segments are small at the boundaries of the cylinder and larger in the middle of the cylinder and in the white background surrounding the object. (B) A cross section between X and Y to show the effect of the segmentation vertically. (C) The membership function to classify the fuzzy boundaries. (D) The classified cylinder with the fuzzy zone surrounding it.

4.1.1.3. Complex models

3D OOA of the complex models is quite different from 3D OOA of the simple models. The added complexity to these models made the process of the object extraction from them more difficult than the simple case. Consequently, the rulesets of the complex models became more complicated and included a long chain of algorithms to be able to retrieve the 3D objects from them. The ruleset of each complex model was explained individually since each model required a different ruleset. **The full details of each ruleset of the complex models are in Appendix 1.**

1. 3D OOA of the first complex model:

The first complex model was described in section 2.3.2. The models are based on combinations of the tested synthetic models and includes (i) two vertical objects that represent the rift branches', (ii) cylinder object representing the craton, (iii) a surface separating the plume in the deeper part of the model and the upper objects, and (iv) three transition zones between each object and its neighbourhood to describe the gradual change between them. The complexity of the analysis was in the parts of the model that had similar density contrasts, but belonging to different objects.

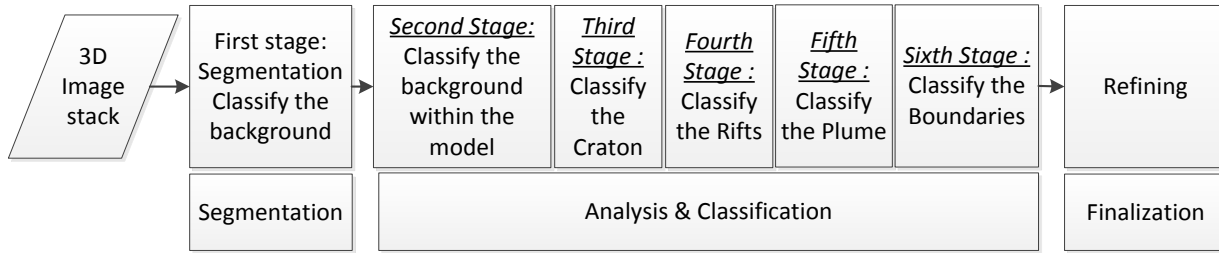


Figure 15: Flow chart shows the stage of 3D OOA for the first complex model.

The ruleset of the first complex model can be divided into six main stages (Figure 15):

- 1- The first stage was a basic one. It mainly separated the white background in the images that did not relate to the objects in the model. Then, the image objects were prepared for further classification by creating object segments using multi-resolution segmentation algorithm. This stage consisted of three main steps:

- The first step used the *“automatic threshold”* algorithm to define the threshold of the white background zone automatically.
- The second step used the *“multi-threshold segmentation”* algorithm to create segments and classify them into “background” and “objects” using the automatic threshold value (Figure 21 (A)).

- The third step used *“multi-resolution segmentation”* to segment the “objects” for the later classification process. The multi-resolution segmentation is an algorithm that builds the segments starting by one pixel and then merges the neighbourhood pixels that only fit both spectral and shape homogeneity parameter of the algorithm. The algorithm requires three main parameters the scale factor, the shape and compactness. The scale factor determines the size of the segments while both shape and compactness determine the spectral and shape homogeneity. The parameters used were small values to capture all the details of objects in the model on the expense of the computational time. These parameters were (scale factor = 10, shape = 0.1, and compactness = 0.1). The usage of large scale parameters (Figure 16) could lead to miss the details of the objects due to forcing the segmentation algorithm to produce large segments.

The effect of different parameters on multi-resolution segmentation

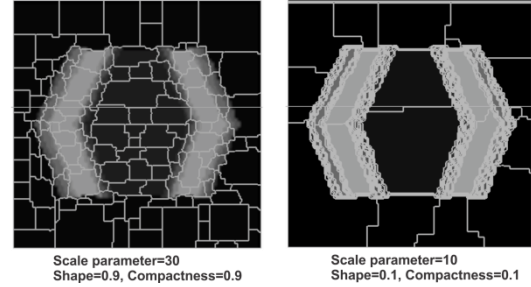


Figure 16: Figure shows the effect of the segmentation parameters on the multi-resolution segmentation algorithm on the size of the segments.

- 2- In the second stage, the background inside the model region was separated from the enclosed model objects (Figure 21 (B)). In this process, a classification based on the pixel values and the number of pixels in the classified segments was used. The pixel value threshold (≤ 12) was used to classify the “background” from the enclosed “objects” (Figure 17). Then, a merging algorithm was applied for the segments belonging to “background” class to merge them together. Finally, a second classification process used the number of pixels of the classified segments. This process aimed to reclassify the small segments inside the objects that were classified as “background”, but they actually belonged to the “objects” class surrounding them.
- 3- The third stage was the classification of the cylinder object that represents the craton (Figure 21 (C)). The classification process assigned the craton class to the pixels with values equal to 20. This value was chosen because the craton had a high density value, subsequently it had the highest density contrast; hence it had a dark grey value that equal to a pixel value 20 (Figure 17). Then, the “merge region” algorithm was applied to merge all the craton segments together.
- 4- The fourth stage was the classification of the two vertical objects that represent the rift branches in the study area (Figure 21 (D)). The classification process assigned the rift class to the pixel with values equal to 128. This value was chosen because the rift branches had a low density values. Hence, they had a light grey colour that equal to the pixel value 128 (Figure 17).

5- The fifth stage was the classification of the deeper part of the model. This part contains the plume that is separated from the upper part by a 2D contact surface (Figure 21 (E) and Figure 17). In the previous stage, the classification process of the rift assigned also the plume object to the rift class (Figure 21 (D)). This happened because both the rift branches and the plume had the same density contrast and consequently the same pixel values (Figure 17). Also, some segments that belonged to the plume were assigned to the craton class based on the pixel value. Because of that, a classification process was applied to assign the entire rift and craton segments that are located deeper than -4500 m depth to the plume class (Figure 17). Then, another classification process was applied to remove the small segments that do not belong to the plume by reclassifying the segments with a number of pixels less than 800 pixels to the “objects” class again.

6- The sixth stage was the most complicated stage in this ruleset. This stage was the classification of the boundaries and assigning them to their objects (Figure 21 (F)). A series of classification processes was applied to classify the boundaries surrounding the rifts and the boundaries surrounding the plume. This classification series depended on the position and the pixel values of the target objects. First, it classified the shallower part of the boundaries from the surface until -2800 m (slice number 44) as “rift boundaries” class (Figure 17). Then, it assigned the deep part of the boundaries, deeper than -3950 m, into the “plume boundary” class (Figure 17). After that, the region between -2800 m to -3950 m was the region that needed to be classified. The problem in this region was that the plume boundary and rift boundary had the same pixel values. Three new algorithms were used to separate them:

- The first was the “find enclosed by” algorithm. This algorithm looks for the segments that are enclosed by one or more than one class and then assign these enclosed segments to the user predefined class. This algorithm was used to define the plume boundary in this region (Figure 18). First, the outer part of the plume boundary was classified using the pixel value 32. Then all the segments enclosed by this outer part were assigned to the “plume boundary” class. This method was able to prevent the misclassification with the rift boundaries that had the same value.
- The second was the “pixel-based object resizing” algorithm (Figure 19). This algorithm allows an object to grow in any X, Y or Z direction constrained by pre-defined thresholds. These thresholds can be adapted by the user or using certain classes that the object can grow into them. This algorithm was used to grow the rift boundary only in the Z “vertical” direction within the classified plume boundary. It was able to define the remained part of the rift boundaries.

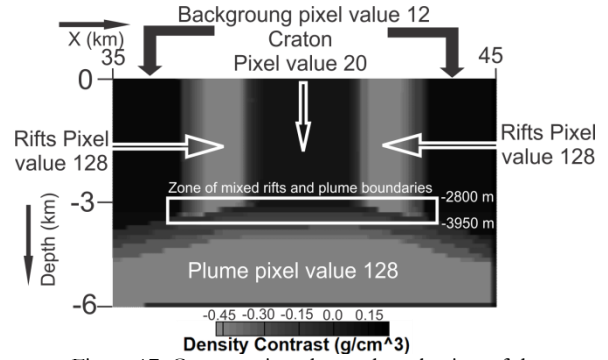


Figure 17: Cross section shows the selection of the thresholds. The background had the darkest color equal to pixel value 12 then the craton with pixel value 24, while the rifts had a light grey color equal to pixel value 128. The white rectangular shows the zone of mixed rifts and plume boundaries with its top -2800 and bottom -3950 depth values

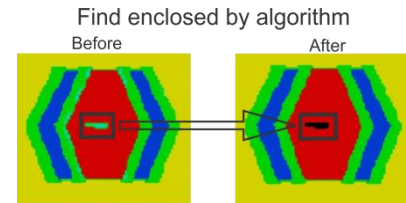


Figure 18: an example for ‘find enclosed by’ algorithm. The green object inside the red class in the left image was defined and classified into the black class after using the algorithm.

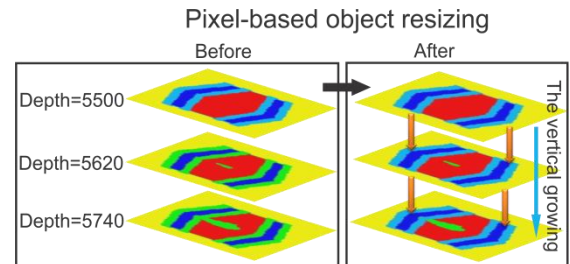


Figure 19: the algorithm of “pixel-based object resizing” the images to the left before applying the algorithm and the images to the right after applying it. The light blue object grew vertically in the negative Z direction into the green class.

- The third was the “grow region” algorithm (Figure 20). This algorithm behaves largely in the same way as the “pixel-based object resizing”. However, the difference is that this algorithm makes the objects grow based on the segments and not pixels. It also does not have the flexibility to constrain growing in a certain direction since the segments can have different shapes and irregular extend. This algorithm was used to classify the last part of the plume boundary. This was accomplished by growing the “plume boundary” class in the remaining segments that belonged to it. This algorithm was applied after the complete definition of the rift boundaries.

Then, a series of refining processes was done to reclassify the small misclassified segments. Finally, “convert image object” algorithm was applied to connect the classified objects in 3D and finalize the classification process (Figure 21 (G) and (H)).

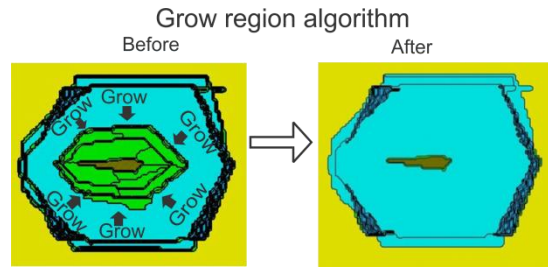


Figure 20: an example for ‘grow region’ algorithm. The cyan object grew in the segments of the green object after using the algorithm.

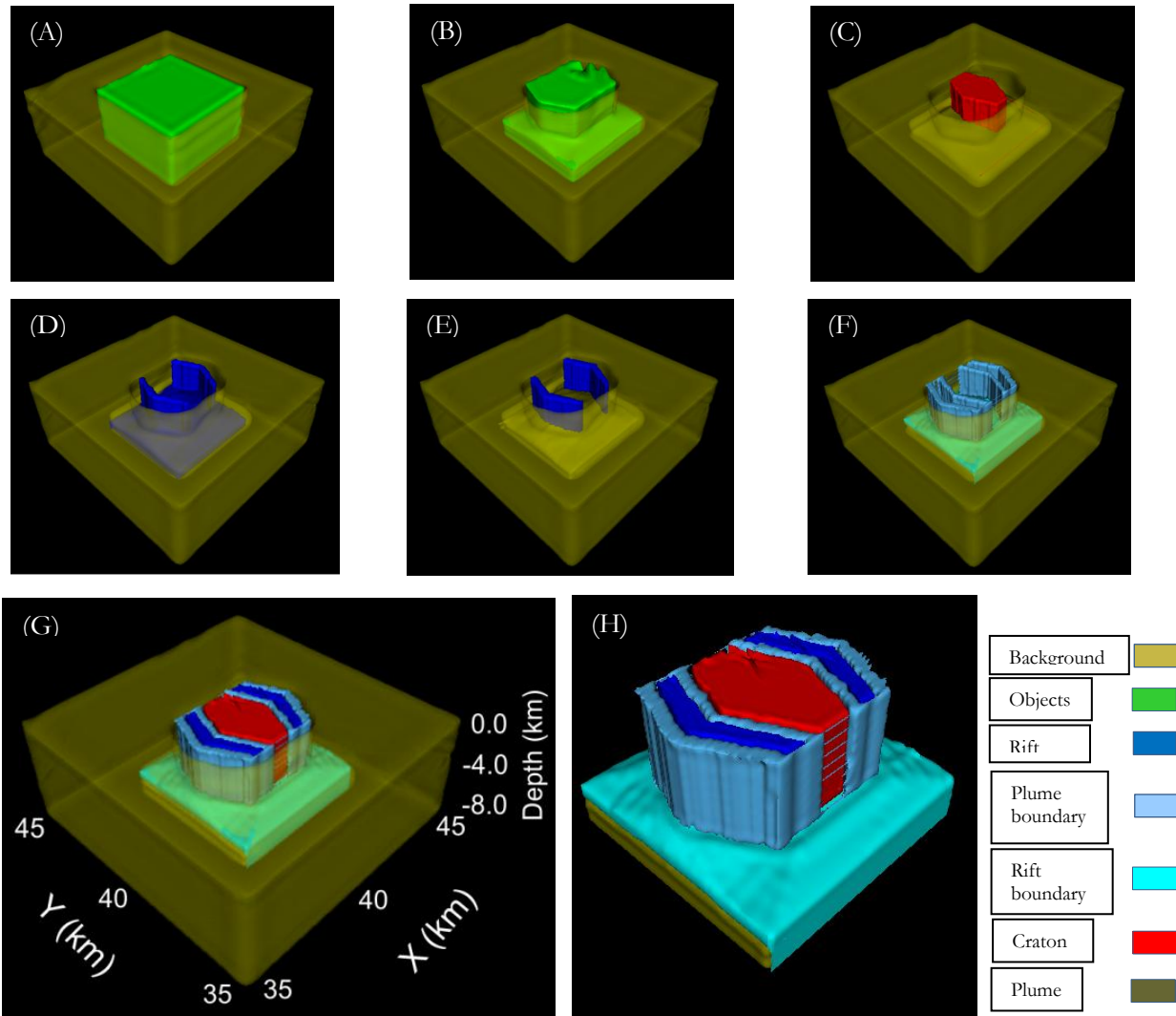


Figure 21: A) to F) are the six stages of the 3D OOA. G) Image is the final results after the refining stage with 50% transparent display for the objects. H) Image is the final classified objects with zoom and removing the background class from the display.

2. 3D OOA of the second complex model:

The second complex model was described in section 2.3.2. The model had the same objects as the previous complex model, though with more complexity. This was done by adding layers in which the density increases with depth. Consequently, the objects within these layers also had variable densities that increase with depth. This complexity added more objects and parts of objects that had the same density contrast values. This increased the difficulty of the classification process.

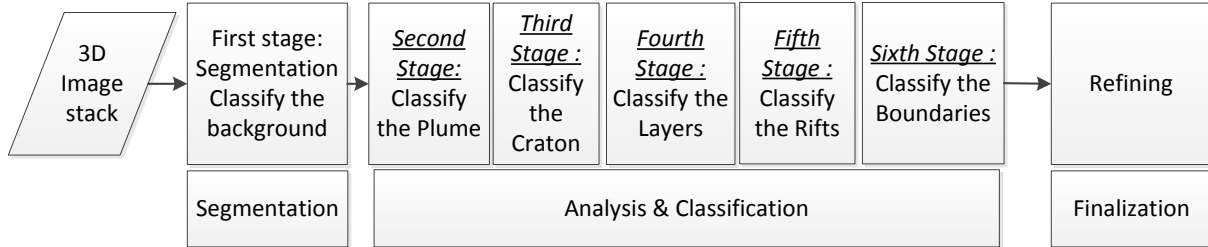
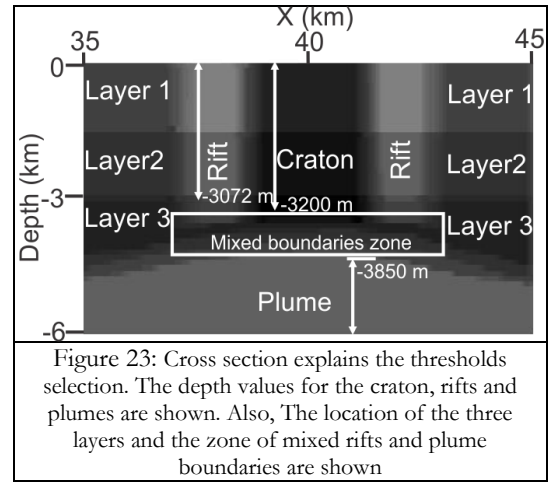


Figure 22: Flow chart showing the stages of 3D OOA for the first complex model.

The ruleset for the second complex model can be divided into seven stages (Figure 22):

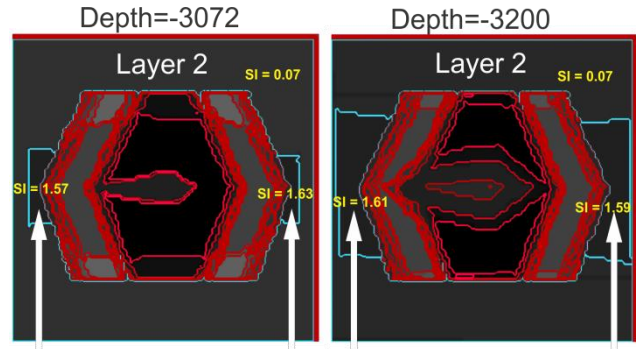
- 1- Another strategy of classification was used in this ruleset to test a different classification strategy that is based on dividing the data into classes with equal interval of pixel values. All the objects or parts of the objects that had the same density contrast were classified in temporary class “objects”. Then, they were reclassified in their correct classes. The “multi-threshold segmentation” algorithm was used to create segments and classify them based on the pixel values. Fifteen thresholds were used to create the segments and classify them to fifteen classes. The fifteen thresholds were selected based on the analysis of the images. Then, the pixels values correspond to the density contrast of the constructed objects in the model were selected. The used thresholds were the pixel values that related to the different density contrast in the model. In this stage, the white backgrounds that result artificially from the images exporting process were defined in a separate class “Background” (Figure 27 (A)).
- 2- The second stage was defining the plume. The plume was defined by separating it from the temporary class “objects”. The plume was separated using its deep location in the model (depth > -3850 m) (Figure 23 and Figure 27 (B)).
- 3- The third stage was defining the craton. It was defined by gathering the parts belonging to it. This was done by separating the parts related to it from the main temporary classes based on the craton shallow location (depth < -3200 m) (Figure 23 and Figure 27 (C)).
- 4- The fourth stage was defining the three different layers. This step was done early because it facilitated the objects extraction processes in the later stages:
 - The first layer was extracted using its shallow location (Figure 23). However, the classification was not perfect. Hence, a refining process was applied based on the number of pixels within each segment since the misclassified segments were characterized by their small size and hence by their low number of pixels (Figure 27 (D)).
 - The second layer was extracted using a different strategy. The first layer was allowed to grow vertically through the segments that belong to the second layer until the boundary of the third layer. Then, the second layer was separated from the first one based on their different depths.



Finally, the segments of the second layer were merged using the “merge region” algorithm (Figure 27 (E)).

- The third layer was extracted using two steps.
 - The first step aimed to define a small part of the layer that existed within the second layer. This part was extracted using the “If-else” algorithm. This algorithm is applying a sequence of processes if certain conditions were satisfied. The “If-else” algorithm was used by putting a condition to restrict the classification within certain depth (-3072: -3200 m) then assign the segments that had certain shape index (from 1.57 to 1.64) to the third layer. The shape index for 3D image stack is a parameter that depends on the smoothness of the surface. The small shape index indicates a smooth surface. This range of shape indices were able to define the segments that belonged to layer three since the size and the geometry are different from the segments belonged to layer 2 (Figure 24).
 - The second step was getting the main part of layer three. It was done by allowing the vertical growing of layer two and the small part of layer three vertically until the plume boundary. Then, the new layer two parts that belong to layer three were classified in their correct class based on their depth (Figure 23). Finally, the “merge region” technique was applied to gather all layer three segments together (Figure 27 (F)).
- 5- The fifth stage was the classification of the rift. The rift was extracted by separating the parts related to it from the temporary classes based on their shallow depth location (depth > -3072 m) (Figure 23). Then, all the parts were joined using “merge region” algorithm (Figure 27 (G)).
- 6- The sixth stage was the classification of the boundaries. The rift boundaries, in the shallow part, were classified based on their location (depth < -2816). The deeper part of the plume boundaries were classified also based on their location (depth > -3968 m).

Then, the region between -2816 m and -3968 m had parts of the rifts and the plumes with the same pixel values (Figure 23). The rift boundaries were separated by allowing the rift object in the shallow zone to grow vertically in this zone through the segments that belonged to it. Another part of the rift boundaries was separated from the plume boundaries based on the longitudinal shape of them using shape index values (shape index ≤ 3.7) (Figure 25). This shape index was able to discriminate between the longitudinal segments that belong to the rift from the circular segments. The plume boundaries were separated in this zone using a different strategy. It had a small part within the craton in slice number 43 at depth -2944 m Figure 26(2). This small part was classified to “plume boundary” using “find enclosed by” algorithm. Then, this small part was allowed to grow vertically in the deeper slice (Figure 26 (3)). After that, the small classified segment in the deeper slice grown in the X and Y direction until fill the circular region with the “plume



The segments within Layer 2 that belong to Layer 3
Figure 24: Figure shows the difference in the shape index (SI) between Layer 2 segments and Layer 3 segments

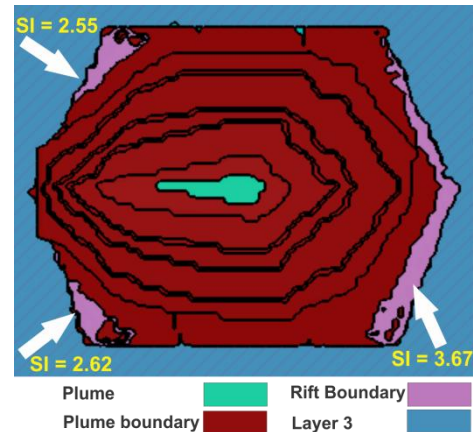


Figure 25: Figure shows white arrows indicating the segments belong to the rift boundary that have higher SI from the other segments that have smooth surface and hence lower SI.

boundary” Figure 26 (4). Then, it was allowed only to grow in the x direction within the segments that belong to the plume boundary Figure 26 (5) (a detailed explanation of the whole process in Figure 26). The plume boundary was defined by repeating this step until the depth of -3712. Finally, the remaining part of the rift boundaries was classified using “pixel-based object resizing” algorithm into the remaining part of the temporary classes (Figure 27 (H)).

- 7- At the end, a sequence of refining processes was applied using a sequence of merging processes. The purpose of this step was gathering all segments of the same object together. Finally, a sequence of reclassification and growing processes was applied to fix some small segments with wrong classification and reclassify them into their correct classes (Figure 27 (I)).

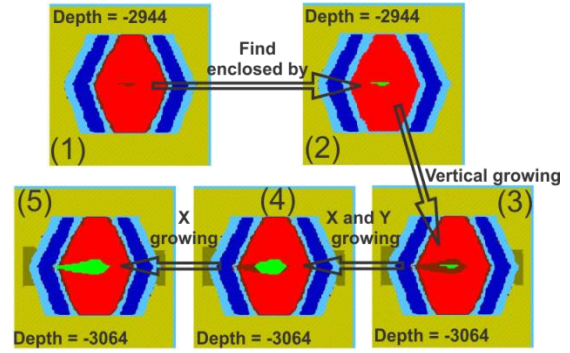


Figure 26: The strategy to classify the plume boundaries in green color. 1) Before and 2) after “find enclosed by algorithm”. 3) The vertical growing in the deeper slice. 4) After grow in the X and Y direction until fill the circular shape. 5) After grow in the X direction only to prevent further growing in the misclassified segments within the rift boundaries.

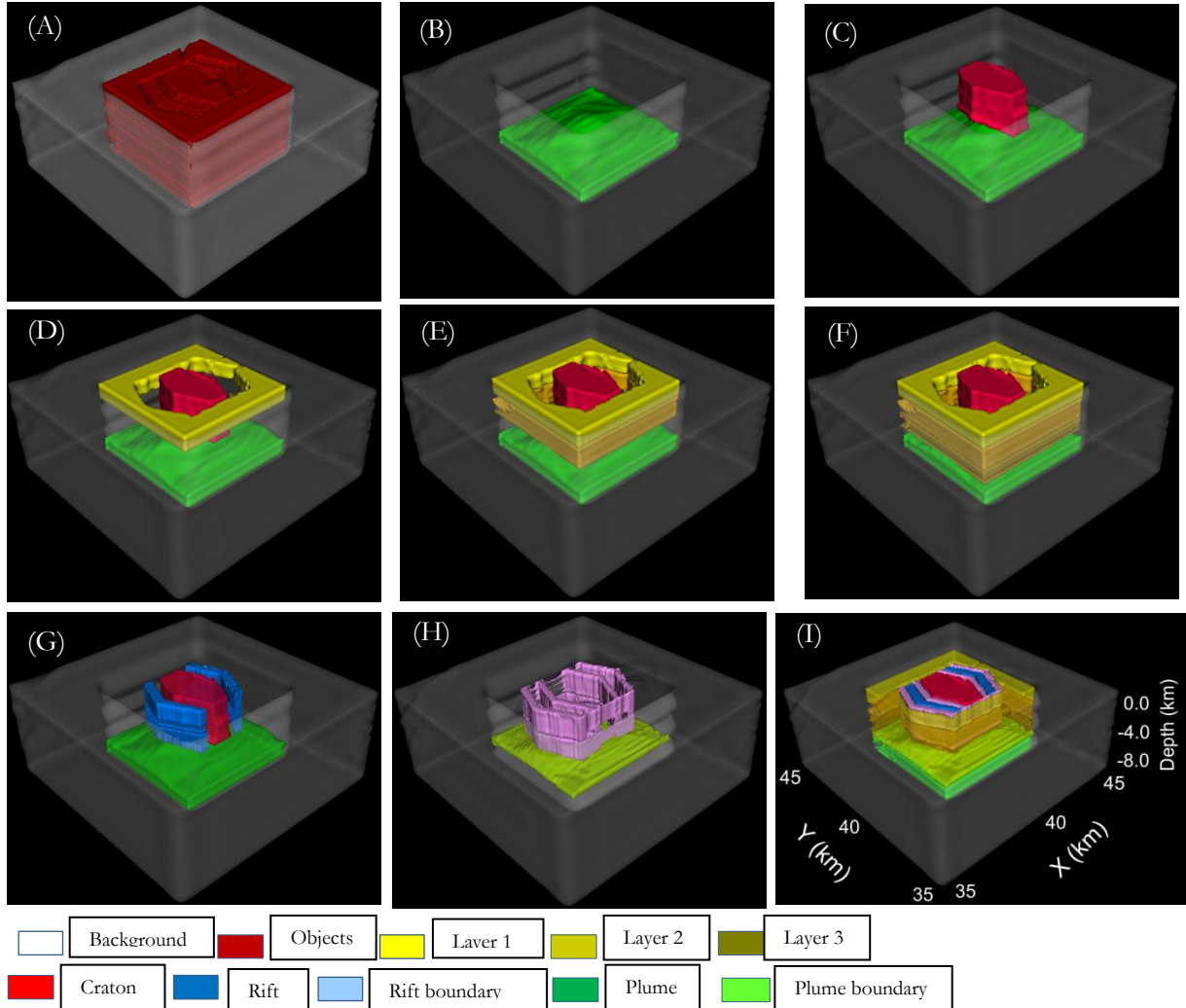


Figure 27: (A) The image stack after classifying the background and the model zone (B) The classification of the plume. (C) The classification of the craton. (D) The classification of the first layer. (E) The classification of the second layer. (F) The classification of the third layer. (G) The classification of the rift. (H) The classification of the rifts and plume boundaries. (I) The classified complete model.

4.1.2. Discussion 3D OOA

From the results of 3D OOA analysis for both simple and complex synthetic models (Figure 13, Figure 14, Figure 21, Figure 27), it was shown that 3D OOA is capable to extract objects from 3D geophysical data with a high level of accuracy. This will also be shown later through the forward modelling process for the second complex model (subsection 4.1.3) since the calculated gravity signal based on the model out of 3D OOA had a misfit of 0.2% with the measured signal (Figure 29). However, there were some limitations in 3D OOA analysis.

The first one was the problem of the depth below the mean sea level. Several trials were made in order to assign the model its true depth values from 0 to -8 km (with depth interval -0.125 km). eCognition was not able to handle assigning -0.125 km as interval for the depth slices. It was only able to handle the positive interval values. This limitation has forced the researcher to assign the -8 km depth to zero km depth and go upward until +8 km that corresponded to 0 km depth. This limitation has not affected the processing and the results of the data since the output classified section and slices were georeferenced manually during the forward modelling stage. Hence, the shifted sections and slices were repositioned in their actual location. However, this solution will caused another problem in the display of the extracted objects during *the real data analysis* since the synthetic data were symmetric but the real data are most likely not. It was the reason that the extracted object looked reversed like a mirror image (Figure 33).

The second problem was the dependency of the classification process on the user knowledge. This happened because the synthetic models were created by the user and consequently the classification process (including the used pixel values, position and context thresholds) was biased by the user knowledge about the models. This limitation will influence the results of the real data analysis. In the real data analysis, the absences of knowledge about the model and the bias toward certain subsurface structural settings will most likely reduce the amount of details that can be extracted from the model.

4.1.3. Results forward modelling (including object based inversion)

In this stage, the forward modelling was done based on the classified sections from 3D OOA. The second complex model was selected for this step because of the complexity that was added in the model which is physically more realistic. Hence, using this model allows judgement of the capability of the methodology to actually retrieve 3D earth structure in complex conditions.

4.1.3.1. Re-constructing the model

The 3D OOA classified sections (Figure 28 (C)) were imported into IGMAS+. Then, the model was reconstructed based on the extracted objects in the classified sections (Figure 28 (D)). The process of reconstructing the model is explained in Figure 28. The original sections before 3D OOA are shown in Figure 28 (B), while Figure 28 (C) shows the sections after 3D OOA analysis. Then, the reconstruction process was done in IGMAS+ (Figure 28(D)). The original synthetic model (Figure 28(A)) was shown to compare it with the retrieved model based on 3D OOA (Figure 28(D)). The reconstruction process was accomplished successfully. However, some distortion happened in parts of the object as it shown in Figure 28 column (D) section 3.

4.1.3.2. Object-based inversion

The object based inversion process was based on Haase (2008) in Schmidt et al.(2011), as mentioned in subsection 3.2.3, to calculate the density contrasts that produce the optimum fit with the measured gravity data. Here, the calculated gravity signal (Figure 29(A)) from the original model (Figure 28 (A)) was considered as the measured gravity signal. The calculated gravity signal (Figure 29(B)) from the reconstructed model (Figure 28 (D)) was compared with the measured gravity signal in order to determine the degree of misfit (Figure 29 (C)) between them.

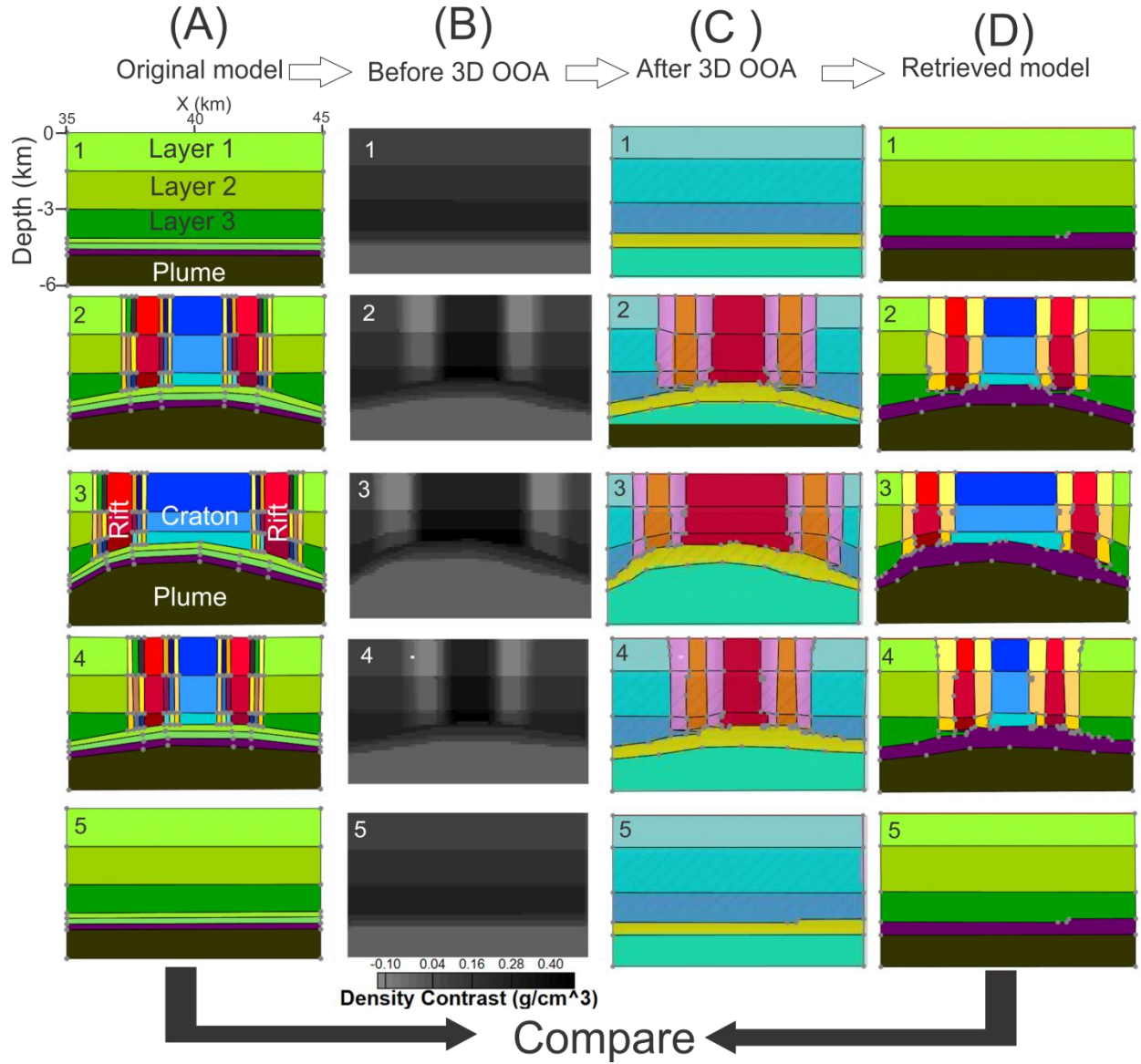


Figure 28: column (A) is the original sections in IGMAS+. Column (B) is the sections before 3D OOA in eCognition. Column (C) is the classified sections after 3D OOA analysis. Column (D) is the constructed model based on the classified sections from 3D OOA in Column C.

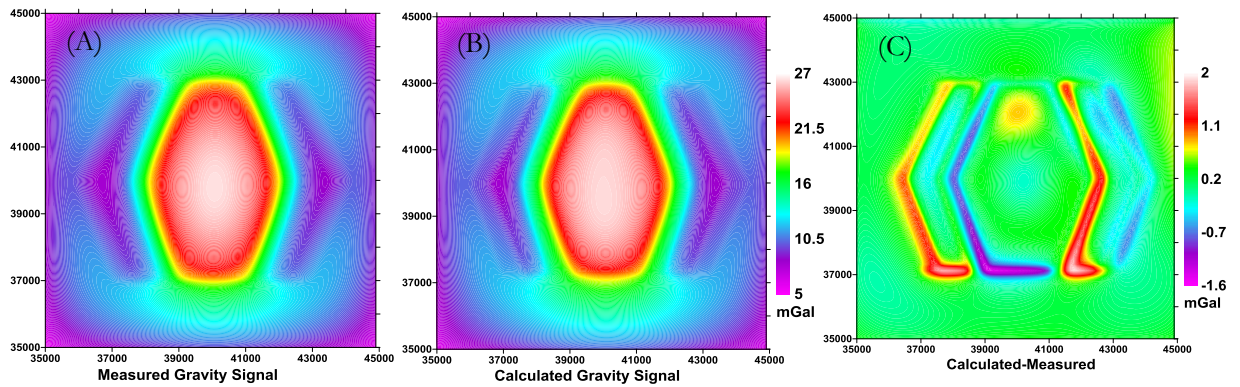


Figure 29: (A) The measured gravity signal. (B) The calculated gravity signal. (C) The difference between the calculated and the measured gravity signal.

The calculated gravity signal showed 99.8% correlation with the measured gravity. However, the retrieved density contrasts showed wrong estimations as shown in Table 4. The retrieved densities showed close values to the original ones in the shallow parts (e.g. LAYER1, CRATON 1, BOUNDARY 1 BET. LAYER 1 & RIFT 1, BOUNDARY 1 BET. RIFT 1 & CRATON 1, LEFT RIFT 1, and RIGHT RIFT 1). However, the density contrasts of the deep objects were not retrieved, and a large error was shown in the density contrasts estimations (e.g. CRATON 3, BOUNDARY 3 BET. LAYER 3 & RIFT 3, and RIGHT RIFT 3). This happened because in the same location the objects had the same geometry and position (in X and Y) but located at different depths, whereas they all contribute in the calculation of the gravity signal. This can explain the large deviation with positive density contrast (CRATON 3 = - 5.704g/cm³) and the large deviation with negative density contrast (CRATON 2= 1.134 and PLUME= 1.045) because their effects cancelled each other out in the calculated gravity signal.

	Original Density	Density Contrast		Retrieved Density contrast	Difference
Layer 1	2.3	0.075	Layer 1	0.07	0.005
Layer 2	2.4	0.175	Layer 2	0.253	-0.078
Layer 3	2.5	0.275	Layer 3	-0.909	1.184
Craton 1	2.5	0.275	Craton 1	0.256	0.019
Craton 2	2.6	0.375	Craton 2	1.134	-0.759
Craton 3	2.7	0.475	Craton 3	-5.704	6.179
Boundary 1 bet. Layer 1 & Rift 1	2.25	0.025	Boundary 1 bet. Layer 1 & Rift 1	0.008	-0.033
Boundary 1 bet. Layer 2 & Rift 2	2.2	-0.025			
Boundary 1 bet. Layer 3 & Rift 2	2.15	-0.075			
Boundary 2 bet. Layer 1 & Rift 1	2.35	0.125	Boundary 2 bet. Layer 2 & Rift 2	0.754	-0.679
Boundary 2 bet. Layer 2 & Rift 2	2.3	0.075			
Boundary 2 bet. Layer 3 & Rift 2	2.25	0.025			
Boundary 3 bet. Layer 1 & Rift 1	2.45	0.225	Boundary 3 bet. Layer 3 & Rift 3	-6.211	6.386
Boundary 3 bet. Layer 2 & Rift 2	2.4	0.175			
Boundary 3 bet. Layer 2 & Rift 2	2.35	0.125			
Boundary 1 bet. Rift 1 & Craton 1	2.4	0.175	Boundary 1 bet. Rift 1 & Craton 1	0.067	0.008
Boundary 1 bet. Rift 2 & Craton 2	2.3	0.075			
Boundary 1 bet. Rift 3 & Craton 3	2.2	-0.025			
Boundary 2 bet. Rift 1 & Craton 1	2.5	0.275	Boundary 2 bet. Rift 2 & Craton 2	0.556	-0.381
Boundary 2 bet. Rift 2 & Craton 2	2.4	0.175			
Boundary 2 bet. Rift 3 & Craton 3	2.3	0.075			
Boundary 3 bet. Rift 1 & Craton 1	2.6	0.375	Boundary 3 bet. Rift 3 & Craton 3	8.436	-8.161
Boundary 3 bet. Rift 2 & Craton 2	2.5	0.275			
Boundary 3 bet. Rift 3 & Craton 3	2.4	0.175			
Boundary 1 bet. Plume & Above	2.3	0.075	Boundary bet. Plume & Above	-0.762	0.937
Boundary 2 bet. Plume & Above	2.4	0.175			
Boundary 3 bet. Plume & Above	2.5	0.275			
Plume	2.2	-0.025	Plume	1.045	-1.07
Left Rift 1	2.1	-0.125	Left Rift 1	-0.102	-0.023
Left Rift 2	2.2	-0.025	Left Rift 2	-1.734	1.709
Left Rift 3	2.3	0.075	Left Rift 3	7.055	-6.98
Right Rift 1	2.1	-0.125	Right Rift 1	-0.137	0.012
Right Rift 2	2.2	-0.025	Right Rift 2	-1.134	1.109
Right Rift 3	2.3	0.075	Right Rift 3	4.584	-4.509
reference	2.225	0	reference	0	0

Table 4: Table shows the original density values and the retrieved density contrast.

4.1.4. Discussion forward modelling (including object based inversion)

The classified slices and sections out of 3D OOA facilitated the process of the model reconstruction (Figure 28). However, the model building was a time consuming process, and IGMAS+ still needs development to become a user friendly application. The reason was that the software only reported the presence of errors during the triangulation process without indication about the reason or the source of the error. The triangulation process is the process in which the constructed configurations in the sections

are interpolated, in the gaps between the sections, to produce the bodies. This was beside the existing difficulties in the process of dividing the objects to introduce a new object beside or within the already existing ones. So manipulation of models is tedious and in case of complex models also sensitive to errors. Although fuzzy boundaries could be retrieved using the powerful membership function classification tool in eCognition it was not possible to define them in IGMAS+. Therefore, the fuzzy boundaries could only be represented as crisp boundaries thereby limiting the capacity to retrieve the exact location of the fuzzy boundaries despite the fact that they are recognizable in the data.

The results of the object based inversion approach, for the reconstructed model, showed some inherent limitations in the approach. Although 3D OOA analysis was able to retrieve the shape and the boundaries of the object, the retrieved density contrast from the inversion showed only good results for the shallow objects. This happened because the objects had the same geometry and X and Y position but located at different depths (Figure 28), whereas that they all contributed in the final calculated signal Figure 29 (D). This led to wrong estimations of the density contrasts of the deep objects. However, the effect of the wrong calculated density contrasts on the calculated gravity signal was minimal, in this case at least, with a high correlation of 99.8% between the calculated and measured gravity signals. The wrong estimation of the density contrasts happened because of two reasons as mentioned in Schmidt et al. (2011):

- 1- The large number of the objects in the model (20 objects).
- 2- The fact that the gravity signal in the same place depended on several objects that had the same spatial geometry but located at different depths. This led to add non-uniqueness in the density contrasts estimations since an infinite number of density contrasts would produce same gravity signal.

This led to a conclusion that 3D OOA was able to solve the problem in the shape configuration of the 3D subsurface bodies but that the inversion needed a low numbers of objects (without objects of identical position and geometry that located at different depths) in order to show good density contrast estimates. The results can also be improved by using *a priori* information, e.g. the density contrast of one or two objects, in the inversion process. Such *a priori* information can be gotten from literature.

4.1.5. Results constrained inversion

The 3D model from the forward modelling process was used to constrain the inversion process. This process was applied to determine the possibility to reduce the misfit between the calculated and the measured gravity through the inversion process.

The forward model was exported using at 100 m resolution for the voxels in X, Y, and Z directions. Then, the voxel cubes were converted into a 3D mesh format using a MATLAB code for use in GRAV3D. Gaussian noise (0.02% of signal strength with an absolute minimum of 0.02) was added to the measured gravity signal since the original data were error free (Figure 30 (G) and (H)).

The calculated densities from the forward modelling process were then converted in two different formats to be used in different ways. The calculated density was converted into density model format and bounds format. The model format was used to constrain the inversion for use as an initial model and a reference model for the inversion process. The bounds format was used to constrain the inversion through the values of the bounds. The density values out of the forward modelling were converted to bounds by allowing the density to change within 0.002 g/cm³ around the original value out of the forward modelling process.

The results of the inversion process showed some remarks. The results of the inversion using the density constraints as initial model were smeared. The retrieved density contrasts ranged between 0.38 g/cm³ and -0.256 g/cm³. The retrieved average density contrast of the rifts was -0.175 g/cm³. This value was close to the average value of the rift of -0.75 g/cm³. The same was shown for the craton. The model did not define the plume; however, it showed a decrease in the density contrasts below the craton (Figure 30 (A)). Comparing the results of the reference and the bounds inversion (Figure 30 (B) and (C)), it shows that the inversion process behaves differently depending on the constraints used. The bounds inversion results

showed that the inversion process kept the wrong density contrasts that were assigned as constraints. However, the reference inversion results showed that the inversion process attempted to retrieve the true density contrasts. This can be shown in the deepest part of the craton where the value of the bounds inversion was around -5.7 g/cm^3 , and the value of the reference inversion was around -2.98 g/cm^3 while the true value was 0.475 g/cm^3 .

The misfit between the calculated and measured gravity was reduced in case of using the density constraints as initial and reference models (Figure 30 (D) and (E)). However, in the case of using bounds, the misfit was the same (Figure 30 (F)). The reason was related to the degrees of freedom in the inversion in case of the initial and reference model scenarios while the inversion was constrained to the bounds values in case of using the density constraints as bounds.

4.1.6. Discussion constrained inversion

The constrained inversion process proved that the misfit between the calculated gravity signal and the measured gravity signal (after the forward modelling and the object based inversion) can be minimized (Figure 30 (D) and (E)). Also, the process was able to, partially; retrieve the true density contrast even in the case of feeding the process with constraints that were wrong.

Analysis of the results showed that:

- Using constraints as an initial model was able to reduce the misfit and retrieved, approximately, the true density contrast; however, it was not possible to retrieve the shape of the objects.
- Using constraints as bounds forced the inversion process to produce the results within the supplied bounds. If the bounds allow a wide range of density contrast variation, the produced model will show larger fit than in the case of using restricted bounds. The process mainly depends on the level of confidence in the density constraints.
- Using constraints as a reference model was able to preserve the shape of the objects and partially retrieve the true density. The use of the density constraints as a reference allowed the inversion process to behave freely during the inversion process. Using the constraints as a reference model required the determination of the Alpha coefficients. α_s is the factor that defines the degree of misfit between the reference model and the calculated one. α_x , α_y , and α_z are the factors that define the aspect ratio which are controlling the preferred dimensions for the growing of the anomalous objects in the model. If the model contains several objects with different dimensions, the value should be as the ratio of the used cell size. In the synthetic model inversion, the default Alpha coefficients were used ($\alpha_s = 0.001$, $\alpha_x = 1$, $\alpha_y = 1$, and $\alpha_z = 1$) which are appropriated to a model with 100 m cell size.

4.1.7. General discussion on synthetic models results

The previous discussions led to conclusions that can be used in the real data analysis stage:

1. 3D OOA allows retrieving the shape and the body boundaries of the subsurface objects.
2. The forward modelling stage cannot represent the fuzzy boundaries in case of using IGMAS+. These conclusions made the crisp boundaries the only choice during the 3D OOA of the real data analysis. Also, the object based inversion process within IGMAS+ Haase (2008) in Schmidt et al. (2011) needs a few numbers of objects and also, if available, some density constraints values about one or two objects.
3. The constrained inversion process depends on the type and the quality of the used constraint. The usage of the constraint as bounds or a reference model is based on the level of confidence in the constraint. This conclusion also mentioned in Williams (2008).

The output conclusions from the results of synthetic data guided the methodology during the analysis of the real datasets of the study area. In the next sections, the results of the real data analysis will be explained and discussed.

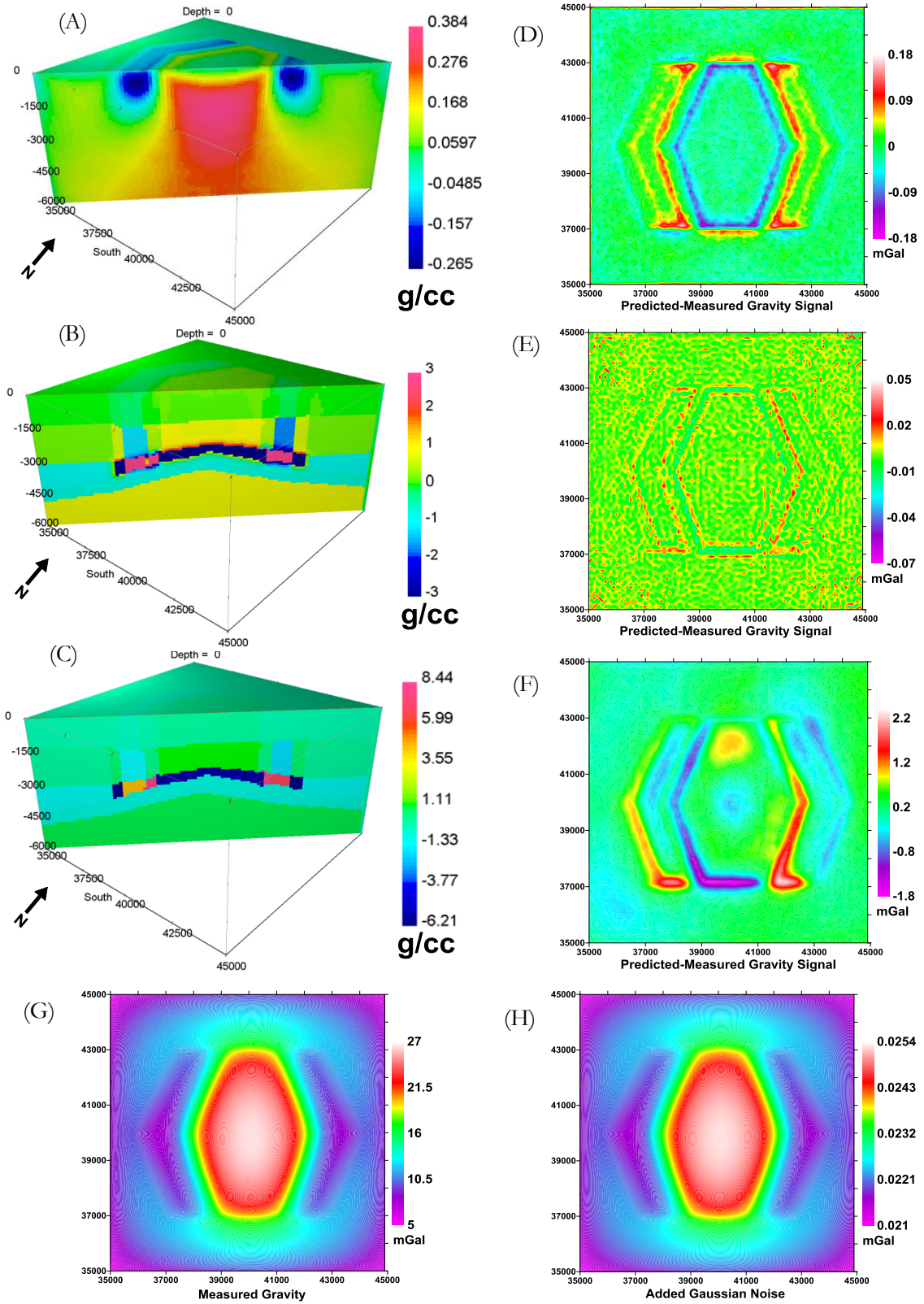


Figure 30: (A) The retrieved density contrasts in case of using the density constraints as initial model. (B) The retrieved density contrasts in case of using the density constraints as reference model. (C) The retrieved density contrasts in case of using the density constraints as bounds. (D) The difference in case of using the density constraints as initial model. (E) The difference in case of using the density constraints as reference model. (F) The difference in case of using the density constraints as bounds. (G) The measured gravity data. (H) The assigned standard deviation error to it after preparing it for the inversion.

4.2. Application to eastern Africa rift system

In this section, the results of the real data analyses are shown. The 3D OOA results of the S-wave seismic tomography model of the study area are shown followed by the forward modelling and object-based inversion results using the classified sections output from 3D OOA. Finally, the results and discussion of the constrained inversion using the output model from forward modelling results are shown.

4.2.1. Results 3D OOA

In this subsection, the results of 3D OOA for the 3D S-wave seismic tomography model of the study area are shown. The following explanation is followed by Table 5 that contain the full details of the ruleset applied.

4.2.1.1. Preparing the image stack

Preparing the image stack was the first stage. The S-wave seismic tomography model included 37 slices starting from depth -40 km to -400 km with a 10 km interval. The slices were gridded using Kriging algorithm using grayscale colour scheme with linear colour distribution method. Then, the slices were exported into images with TIFF format with their geo-reference information in order to construct the 3D image stack (Figure 32 (A)). After that, the image stack was used for 3D OOA in eCognition. The image stack was imported to eCognition to start 3D OOA analysis of the model. The model was analysed using a ruleset that was similar to the ruleset of the second complex model (section 4.1.1.3). However, there were some differences in the strategy of 3D OOA. The ruleset for the S-wave seismic tomography model can be divided into three stages (Figure 31):

4.2.1.2. Stage 1: Segmentation

In this stage, the model was segmented using the “multi-threshold segmentation” algorithm. The algorithm was fed by 9 thresholds in order to divide the image object level to 10 classes (Figure 32(B)). The selected number of classes that controlled the thresholds values was chosen based on the results and the interpretation of the 3D seismic tomography model as mentioned in Adams et al. (2012). The authors (Adams et al.) used 10 classes to show the results of the model. Therefore, the same number was chosen for the classification process. The values of the 9 thresholds were selected in order to divide the image pixel values into 10 classes using equal interval. Then, a small band of white background in the end of the southern and eastern corner of the 3D image stack, which was an artefact created during the image exporting process, was removed using the classification algorithm. To define the background class the algorithm used thresholds of a pixel value equal to 255, which equals the value of the white background.

4.2.1.3. Stage 2: Classification

The classification stage used the “assign class” algorithm. It can be divided into five steps.

- 1- The first step aimed to classify the high velocity zone below the plume. It assigned the high velocity classes at a depth greater than 290 km to “deep high velocity” class (Figure 32-C).
- 2- The second step aimed to classify the craton and the high velocity zones in the shallow part of the model. High velocity classes in the shallow part were assigned to the “craton” class (Figure 32 (D)).
- 3- The third step aimed to classify the plume which is represented by the low velocity zone that is located deeper than 200 km. Low velocity classes that are below 160 km depth are therefore assigned to the “plume” class (Figure 32 (E)).
- 4- The fourth step aimed to classify the two rift branches. It assigned the low velocity layers in the shallow zone with depths less than 150 km to the “rift” class (Figure 32 (F)).
- 5- Then the zone between the upper part of the model (including the craton and rifts) and the deep part of the model (including the plume and the high velocity zone beneath it) was divided into three layers using the initial segmentation thresholds (Figure 32 (G), (H) and (I)).

4.2.1.4. Stage 3: Finalizing

The finalizing stage aimed to finalize the 3D OOA analysis. It started with a series of the “merge region” algorithm to merge all the classified segments from the same class into objects. Then, it was followed by the “convert image objects” algorithm to connect the classified objects in 3D (Figure 32 (J)).

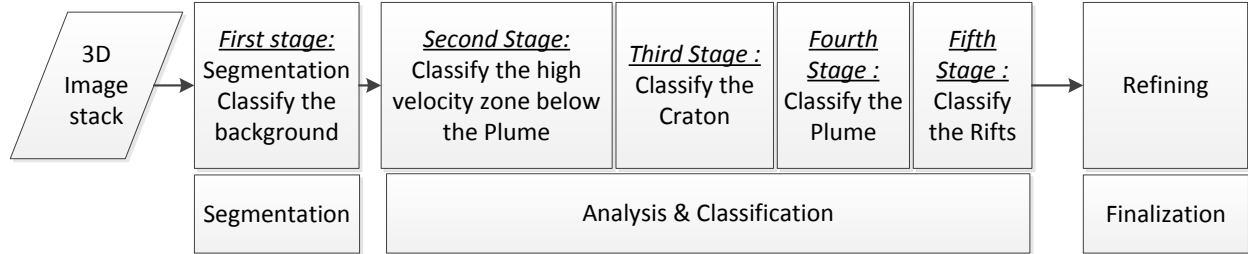


Figure 31: flow chart show the strategy that was used to classify the 3D S-wave seismic tomography model.

Process	Used class/domain	Thresholds	Parameters	Description
multi-threshold segmentation	Domain: Pixel Level	Class 1: _lev10 Threshold 1: 25 Class 2: _lev09 Threshold 2: 50 Class 3: _lev08 Threshold 3: 75 Class 4: _lev07 Threshold 4: 100 Class 5: _lev06 Threshold 5: 125 Class 6: _lev05 Threshold 6: 150 Class 7: _lev04 Threshold 7: 175 Class 8: _lev03 Threshold 8: 200 Class 9: _lev02 Threshold 9: 225 Class 10: _lev01	Level Name: New Level Image Layer: Layer 1	The algorithm uses the threshold to create to classes for objects and background
Classification	Domain: Image Object Level Level: New Level Class Filter: lev01, lev02, lev03, lev04, lev05, lev06, lev07, lev08, lev09, lev10		Active classes: BG	Evaluate the membership function that assigned to the evaluated class
assign class	Domain: Image Object Level Level: New Level Class Filter: lev03, lev04, lev05, lev06	Z distance to first slice < 11	Use class: _Deep_HighVel	The algorithm assigns the a candidate object satisfying the given threshold to the “Use class”
assign class	Domain: Image Object Level Level: New Level Class Filter: lev01, lev02, lev03, lev04		Use class: _Craton_HighVel	The algorithm assigns the a candidate object satisfying the given threshold to the “Use class”
assign class	Domain: Image Object Level Level: New Level Class Filter: lev09, lev10		Use class: _Plume	The algorithm assigns the a candidate object satisfying the given threshold to the “Use class”
assign class	Domain: Image Object Level Level: New Level Class Filter: _Plume	Z distance to first slice >= 25	Use class: _Rift	The algorithm assigns the a candidate object satisfying the given threshold to the “Use class”
assign class	Domain: Image Object Level Level: New Level Class Filter: lev07, lev08, lev09, lev10	Z distance to first slice > 26	Use class: _Rift	The algorithm assigns the a candidate object satisfying the given threshold to the “Use class”
merge region	Domain: Image Object Level Level: New Level Use Class: _Deep_HighVel		Fusion super object: yes	the algorithm merges all the segments belong to the “use class” into one segment
merge region	Domain: Image Object Level Level: New Level Use Class: BG		Fusion super object: yes	the algorithm merges all the segments belong to the “use class” into one segment
merge region	Domain: Image Object Level Level: New Level Use Class: _Craton_HighVel		Fusion super object: yes	the algorithm merges all the segments belong to the “use class” into one segment
merge region	Domain: Image Object Level Level: New Level Use Class: _Plume		Fusion super object: yes	the algorithm merges all the segments belong to the “use class” into one segment
convert image objects	Domain: Image Object Level Level: New Level Use Class: all the classes		Connected 3D	The algorithm aim to convert image object to 3D connected objects to improve the construction and the visualization of the objects

Table 5: Table shows the full details of 3D OOA of the real data.

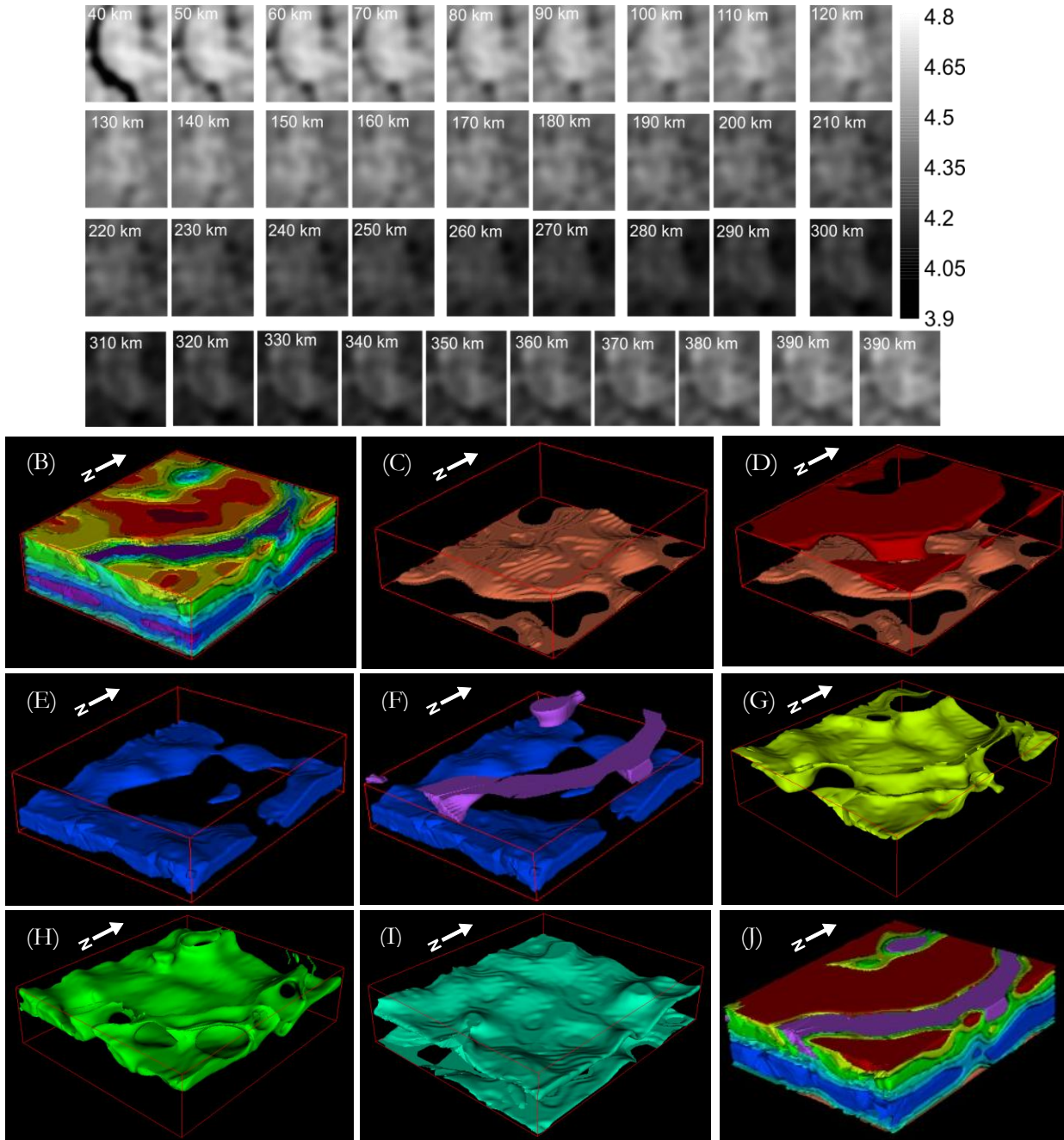


Figure 32: (A) The raw image slices. (B) The cube after the segmentation. (C) The cube after the classification of the high velocity zone below the plume. (D) The cube after the classification of the craton. (E) The cube after the classification of the plume. (F) The cube after the classification of the rift. (G) Layer 1. (H) Layer 2. (I) Layer 3. (J) The cube after the finalizing stage

The results of the 3D OOA (Figure 32) showed the different structural elements of the model. The process was able to classify the rifts, craton, plume, the high velocity zone below the plume, and three layers. These three layers were located between the shallow part, containing the craton and the rifts, and the deep part, containing the plume and the high velocity zone below it. They were divided into three layers because they contained a wide range, about 30% (4.4 km/sec^{-1} to 4.65 km/sec^{-1}) of the full range of the seismic velocities (3.88 km/sec^{-1} to 4.8 km/sec^{-1}). This wide range was preferred by the user to be described by three layers, which could describe a gradual change in the velocity.

4.2.2. Discussion 3D OOA

3D OOA was able to extract 3D objects from a 3D S-wave seismic tomography model. However, the process was affected by several factors that need a detailed discussion.

4.2.2.1. Segmentation

The multi-threshold segmentation method was able to divide the model into ten classes with fixed interval. These classes were reclassified later to their objects' classes. The multi-threshold segmentation algorithm is controlled by the value of the thresholds. The selected number of classes that controlled the thresholds values were chosen based on the results and the interpretation of the 3D seismic tomography model as mentioned in Adams et al. (2012). However, this number of classes was not able to define the location of the objects' boundaries. A test was made using 15 classes instead of 10, and the results showed that the general patterns of the objects were preserved without clear definition of the boundaries (Figure 33 (A) and (B)). It is also crucial to mention that it was not possible to increase the number of classes due to the limitation in the forward modelling process as will be explained later. Some objects needed to degrade their details because of the large section interval that will be used later in the forward modelling stage as will be discussed in subsection 4.2.4.2.

The multi-threshold approach is not optimal for 3D OOA. The powerful segmentation algorithms (e.g. multi-resolution segmentation), object features and statistical tools in eCognition were not fully used. A methodology should be developed for the cases where the thresholds are not available or not clear. A work flow is needed to be developed to integrate such automatic approaches with statistical analysis of each depth slice individually. This can be done to identify and connect the required parameters between the depth slices.

4.2.2.2. Classification

The results of the classification process faced some problems. Some objects' details were lost, and others were not clearly defined during the classification. The craton object (Figure 33 (D)) merged four classes; the dark red, the red, the orange, and the yellow class (Figure 33 (C))). The three first classes (Dark red, red, and orange) had a high velocity that belongs to the craton. However, the fourth class (yellow) represented the transition zone between the craton and the surrounding objects. By including this class to the craton object, the details of the craton boundaries were lost. The rift object also was not clearly defined. The classification of the rift was based on the low velocity characteristics and the depth extent. However, the boundaries of the object in 3D had fuzzy characteristics. This made the object lose some details from its actual boundaries position (Figure 33 (B) and (C)). This meant that another approach is needed to extract the actual location of the object boundaries.

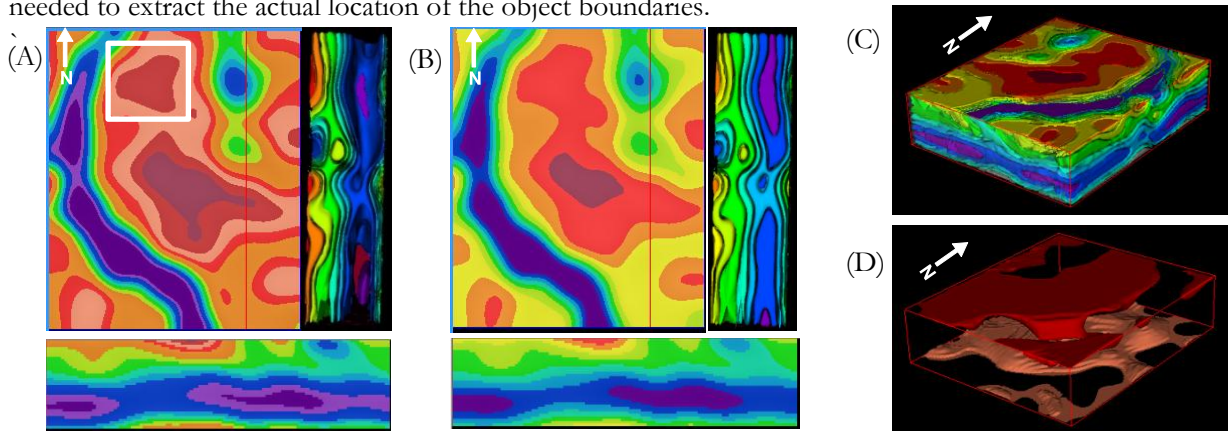


Figure 33: A) the results of the segmentation test using 15 thresholds (the white box indicating the effect of losing some details related to the gravity anomaly which will be explained) later and B) the original segmentation using 10. (C) The 3D view of the basic 10 classes and also show the mirror image effect in comparison with figure (B). (D) Figure shows the effect of degrading the four classes (dark red, the red, the orange, and the yellow) in (C) during the classification to the craton class.

Another important issue in the geophysical data is the change in the histogram content (e.g. velocity or density values) with depth (Figure 34). This issue affected the behaviour of the automatic approaches such as the “automatic threshold” and “estimate scale parameter” tool for multi-resolution segmentation. These automatic approaches can prevent the subjectivity in the thresholds selection process and improve the quality of the 3D object extraction process.

Also, the limitation of the forward modelling process (as discussed in subsection 4.1.7) prevented using the powerful membership functions of eCognition to define fuzzy boundaries as in the case of the craton and rift. These fuzzy boundaries could not be built in the forward modelling process, and hence, they were not used in the 3D OOA. The usage of crisp boundaries instead of fuzzy boundaries in places where objects had fuzzy boundaries caused loss in the details of the object boundaries.

The conclusion of the previous discussion is that, the workflow is needed to be developed to identify the actual location of the boundaries. This can decrease the number of classified objects and produce accurate location of the boundaries that can affect the results of the forward modelling. The accuracy assessment of 3D OOA analysis will be evaluated after the forward modelling stage.

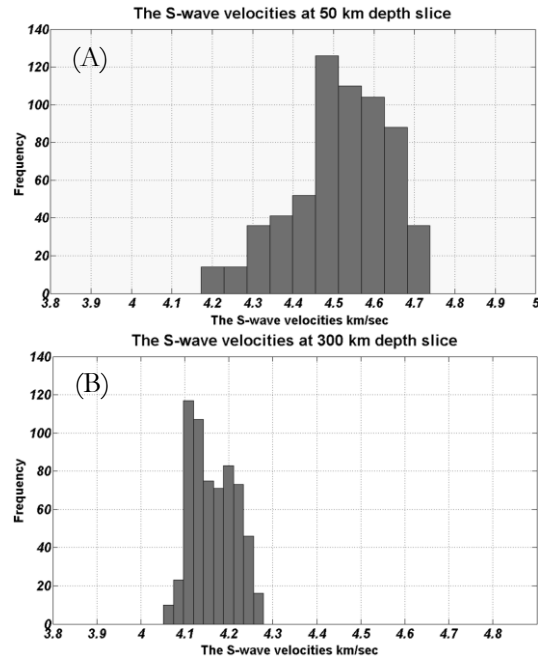


Figure 34: (A) The histogram of the slice at 50 km depth. (B) The histogram of depth 300 km. The figures show the difference in the range of velocity contents through the depth.

4.2.3. Results forward modelling (including object based inversion)

In this subsection, the results of the forward modelling stage are shown. The subsection includes the step of preparing the satellite gravity, the reconstruction step, and the object-based inversion step

4.2.3.1. Preparing the satellite gravity data

The Bouguer gravity data was subjected to a filtering process to reduce the small wavelength content of the anomalies since these anomalies cannot be retrieved in the model because of the low resolution of the input data (111 km). A Cosine roll-off filter was used in the filtering process because it is a clean filter that can reduce ringing effects possibly created during the Fast Fourier Transform (FFT) filtering process in the wavenumber domain. The Cosine roll-off filter also has the advantage that it does not change the content of the power spectrum of the data. A regional Cosine roll-off filter was applied on the data with short wavelength corner frequencies equal to 111 km and an intermediate filter degree equal to 5 (0:10 full degree range) to keep balance between the long wavelength content and the ringing effect (Figure 35 (C)).

4.2.3.2. Re-constructing the model

The classified slices and sections from 3D OOA were used to build the model in the forward modelling process. In order to reconstruct the full resolution model, 56 cross sections could be used. This is spatially equivalent with a 0.25 degree (27.5 km) section intervals in X direction. However, 14 sections, with about 111 km distance interval across the X direction, were used to reconstruct the model due to the limitation of IGMAS+ on model input and computation time as discussed earlier (subsection 3.2.3). An empty density model of the study area was created in IGMAS+ software. Then, the classified slices, sections, the measured satellite gravity, and DEM were imported in it (Figure 35 (C) and (D)). After that, the reconstruction process was accomplished based on the classified sections (Figure 35 (E) and (F)). Last, the objects were formed by the triangulation process (Figure 35 (G), (H), (I) and (J)).

4.2.3.3. Object-based inversion

The inversion process was applied on the reconstructed model to calculate the density contrasts of the reconstructed objects. It was assumed that these calculated density contrasts could produce a minimum misfit between the measured satellite gravity and the calculated gravity response. There were in total 9 reconstructed objects. The calculated density contrasts for the 9 classes are shown in Table 6.

Object	Density Contrast (g/cm ³)	Average seismic velocity
Crust 0:40 km	0.118 Reference: 2.67 (0:10 km) and 2.90 (10:32 km)	
Craton	0.001 reference 3.35	4.44:4.8
Rift	-0.047 reference 3.35	3.88:4.26
Layer1	-0.025 reference 3.35	4.35:4.44
Layer2	0.003 reference 3.35	4.26:4.35
Layer3	-0.047	4.26:4.17
Plume	-0.058	4.08:4.17
Inner plume	0.006	4.08:3.88
High velocity zone below the mantle	0.056	4.26:4.53

Table 6: Table shows the results of the object based inversion process. The reference values were based on results from Ebbing et al. (2001) based on the equation of Christensen and Mooney (1995). They estimated the reference model up to depth 180 km.

Consequently there were no available values for the deeper objects.

The craton, the rifts, and plume density contrasts were correlated with the seismic tomography model. The rifts had a negative density contrasts which correlated with the low velocity in the seismic tomography model. The craton had a positive density contrasts which correlate with the high velocity of the seismic tomography model; however, the craton had about 8% velocity increase which did not correlate with the 0.1% density increase in the retrieved value. The plume had a low density contrasts that correlates with the low seismic velocity; however the inner plume, which should have a lower density contrast than the plume, had a small increase in the density contrast. The density contrasts of the three layers had a correlation between Layer 2 and Layer 3 with the seismic tomography velocity; however, Layer 1 had a negative density contrast, which contradicts the seismic tomography results. The density contrast of the high velocity zone below the plume was correlated with the results of the seismic tomography model.

The results of the inversion process (Table 6) should be interpreted in relation to the background values. Ebbing et al.(2001) used the global IASPEI seismic layered velocity model and converted it into density using the velocity-density relation that published by Christensen and Mooney (1995). This model was assumed theoretically to produce a normal gravity field without any anomalies. Therefore, the deviation from these background densities was assumed to produce the gravity anomalies in the gravity measurements. The background values of the deeper layers were not estimated; hence the values could not be interpreted in relation to their absolute values.

The calculated gravity signal had 70% correlation with the filtered Bouguer anomaly signal (Figure 35 (B)). The patterns in the calculate gravity signal had a correlation with the objects in the model as the low Bouguer anomaly at the rifts and the circular pattern in the middle that correlates with the craton. However, two high Bouguer anomalies were not retrieved (Figure 35 (A)). These anomalies were not retrieved because of the inversion process did not include objects that had the same extension and geometry. It is crucial to mention that the filtering process only removes the anomalies based on their wavelength and not the depth. This means that the shallow objects with the large wavelength will still exist in the data even after the filtering process. These objects were not modeled since the model starts at 40 km depth. Another crucial factor that affected the correlation result is the edge effect (Figure 35 (B), (E) and (F)). The edge effect happens when the model is extended laterally beyond its original extension. This causes abrupt changes in the calculated gravity signal at the edges of the model. This effect can be avoided in the future by not extending the models beyond their lateral extend.

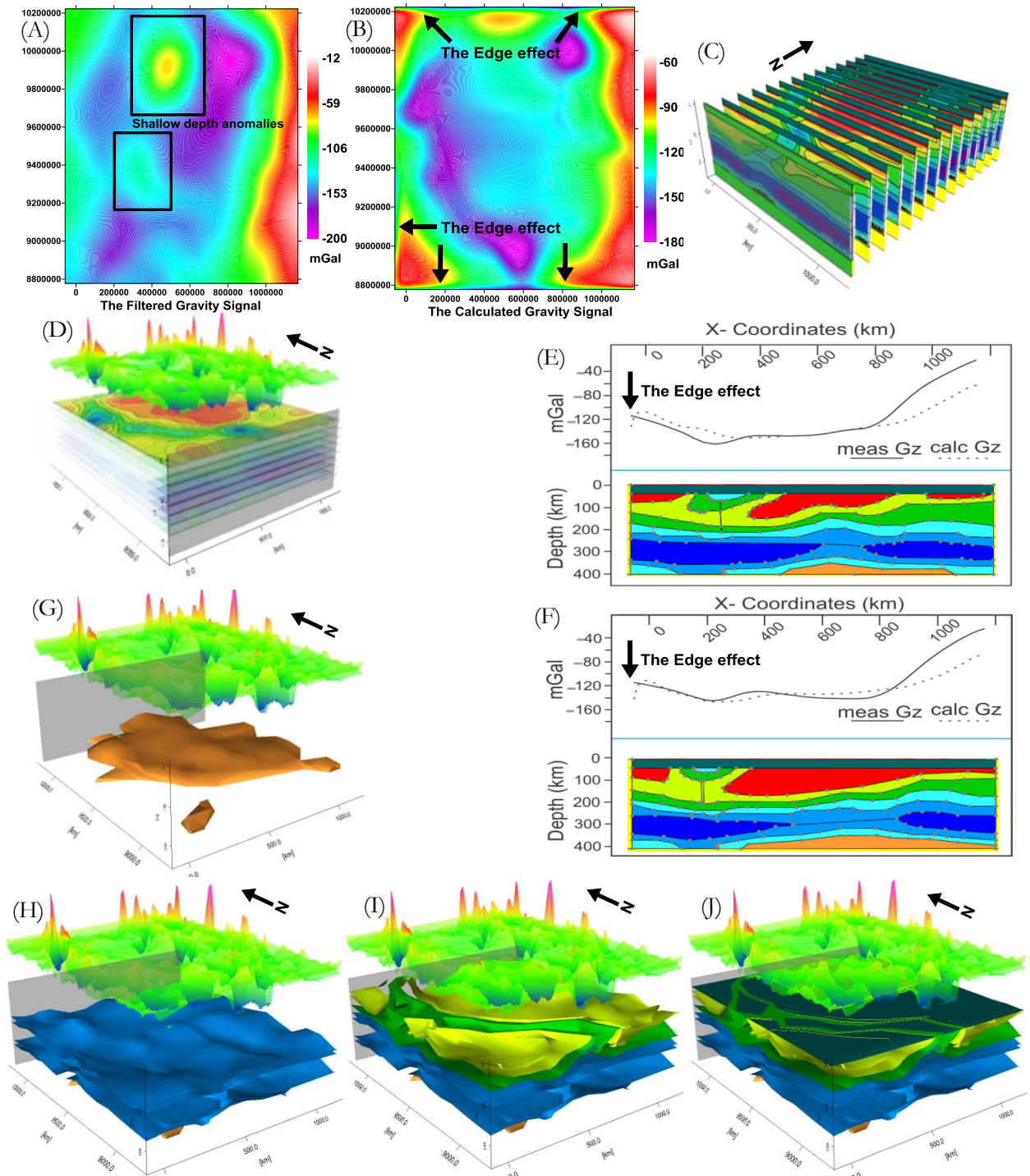


Figure 35: (A) The results using 111 km Cosine roll-off filter showing the imperfection in the filtering process. (B) The calculated gravity signal after the object based inversion. (C) The importing process of the classified sections out from 3D OOA. (D) The importing process of the classified slices. (E) And (F) two sections from the reconstructed and their observed and calculated signal. (G) The reconstruction process of the high velocity zone below the mantle. (H) The reconstruction of the Plume. (I) The reconstruction of the three layers, craton and rifts. (J) The complete model

4.2.4. Discussion forward modelling (including object based inversion)

The forward modelling process was a crucial step in this research since it included the reconstruction of the model and the estimation of the density contrast of the objects. The process included critical steps that will be discussed in details below.

4.2.4.1. The depth limitation of the satellite gravity measurements

One of the critical points was the depth limitation and the validity of using gravity data to model the study area down to 400 km depth. Two tests were done to evaluate this. First, the power spectrum of the satellite gravity measurements was calculated to define the relation between the power of the wavelengths content of the data and their depth. The power spectra showed depth extends up to 170 km. This means that the wavelength content of the data could show up to 170 km; however, the contribution from deeper depths can be present since the wavelength content depend on the extend of the study area and not on the nature of the gravity measurements (Figure 36 (F) and (G)). Second, the data were subjected to Cosine roll-off filter to remove the short wavelengths up to 400 km (Figure 36(B)) which approximately can reach to 120 km as shown in the power spectrum Figure 36 (G). This step aimed to remove the effect of the upper part of the model up to the plume depth (~ 200 km). Then, the forward gravity signal of only the plume and the high velocity zone beneath it was calculated (Figure 36 (C)). The filtered satellite gravity signal was then compared with the forward calculated signal. The comparison showed a poor correlation. However, the forward calculated signal showed a good correlation with the low pass filtered signal > 1000 km based on the work of Simiyu and Keller (1997) (Figure 36(E)). This large wavelength cut off filter was not possible using the data extend of the study area. From both tests, it was concluded that the signal from the deep part of the model existed in the gravity measurements. Also, by referring to the literature, it was found that Mishra et al. (2012) used the regional Bouguer satellite gravity to model their study area up to 320 km depth.

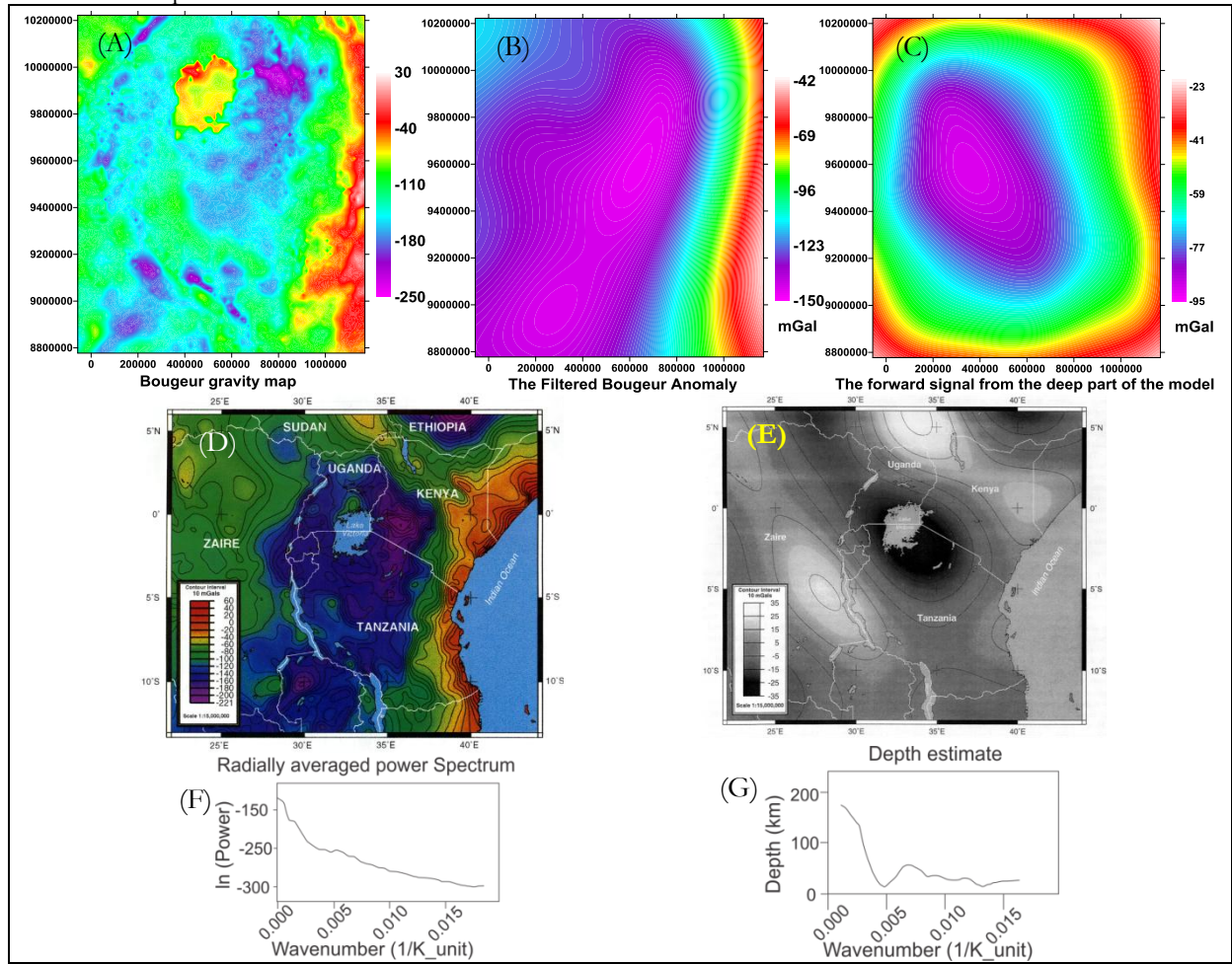


Figure 36: (A) The Bouguer anomaly map of the study area (B) The filtered Bouguer map using Cosine roll-off low pass filter > 400 km. (C) The forward gravity signal from the deeper part from the reconstructed model using plume and the high velocity zone below it. (D) The Bouguer anomaly map adapted from Simiyu and Keller (1997). (E) The low pass filtered Bouguer map using pass > 1000 km that correlate with the forward gravity signal adapted from Simiyu and Keller (1997). (F) The power spectrum of the Bouguer gravity signal. (G) The depth estimation based on the power spectrum.

4.2.4.2. The reconstruction process

In the forward modelling step, the forward model of the study area was constructed using the classified sections output from 3D OOA. The reconstructed model explained approximately 70% of the filtered measured satellite gravity signals (Figure 35 (B)). The results of the forward modelling process were affected by the reduction in the details due to the degradation that happened in the reconstruction process (Figure 37 (B) and (C)). The used section interval 111 km (1 degree) instead of 27.25 km (0.25 degree) affected the details of the objects in the reconstructed model. These details affected the accuracy of the forward modelling because the gravity signal shows these small scale details. However, separating this class in an individual object during 3D OOA was not possible, because it contained details that would not be possible to build them in the model due to the large section interval (111 km) (Figure 37(A) and (D)).

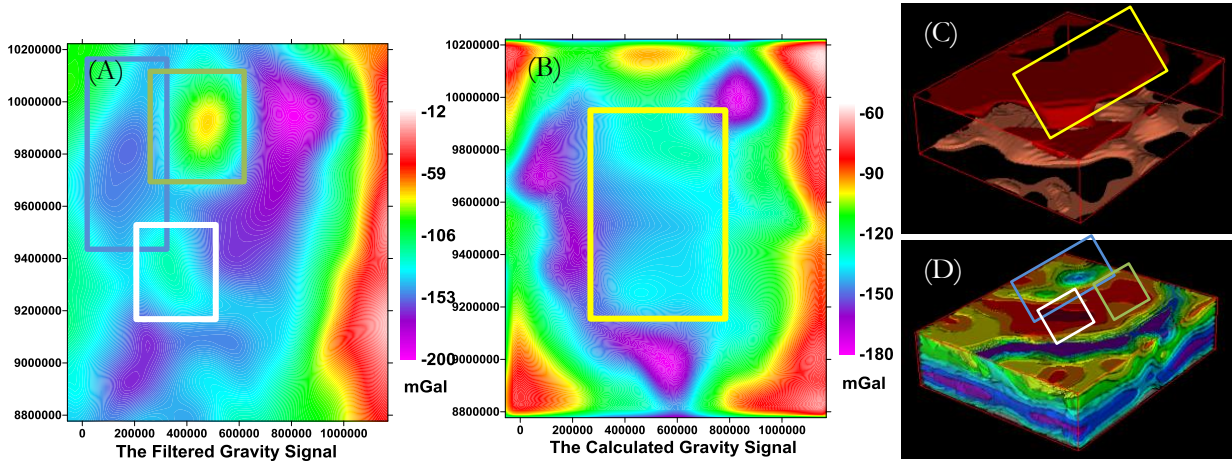


Figure 37: figure shows the effect of the class merging on the forward modelling stage. (A) and (D) show the details that existed in the model before the process of the degradation of the classes that related to the rift in blue rectangular, the northern portion of the craton in green rectangular (also see Figure 33 (A)) and the central portion of the craton in white that seems to belong to shallow depths anomalies. (B) and (C) show the effect of the class degradation during the classification of the craton in the forward modelling signal.

The reason behind selecting 111km as section interval (14 sections to reconstruct the model) was the difficulties in the reconstruction process that were faced during the synthetic stage. IGMAS+ software is a powerful and interactive software; however, the building process consumed a long time. The main reason was the errors that appeared during the building process. The software does not supply the user either with the source of errors, or a clear scheme to solve them. Also, the triangulation step caused several errors due to the limitation in representing various highly detailed shapes which all based on triangles.

4.2.4.3. The object based inversion process

The object based inversion process was controlled by the accuracy of the shape and the boundaries of the extracted objects. The 30% de-correlation between the measured and the calculated gravity signal is because of the missing details in shape and boundaries of the objects. In the synthetic test, the accurate calculated gravity signal 99.8% was retrieved. This de-correlation happened due to 4 factors:

1. The large section interval and the edge effect.
2. The inaccurate estimation of the accurate location of the object boundaries.
3. The assumption of the 3 layers between the upper part of the model and the lower part of the model was overestimated and they highly probable only two layers
4. The imperfection in the filtering process and the residual shallow anomalies.

The estimated density contrasts (Table 6) showed two values that contradicted with the seismic tomography results. The density contrast of Layer 1 and the inner plume objects. The wrong estimation for the density contrast of Layer 1 is highly probable because of the vertical overlapping with layers 2 and 3. However, the inner plume high density contrast was probably due to a different reason. In the work done by Cammarano (2013), the low velocity in this zone was translated to a high temperature (Figure 38

(A)), while the density showed an increased trend (Figure 38 (B)).

This can explain that this inner plume positive density contrast correlated with the long wavelength high anomaly at the eastern and the western end of the model in the filtered Bouguer anomaly maps (Figure 37 (A), Figure 36 (B) and (E)). However, this could not explain the low density zone that belongs to the plume beneath it (Figure 35 (G) and (H)).

4.2.4.4. Accuracy assessment of 3D OOA

The accuracy assessment of the extracted model of 3D OOA was evaluated based on the correlation result between the measured and the calculated gravity signal (Figure 37 (A) and (B)). The calculated gravity signal shows a correlation with the general pattern of low Bouguer anomaly in the middle of the map with high anomaly in the eastern and western end of the map. The rift trends were matched with the pattern in the measured data. However, the large section interval caused losing of some details in the objects. These details can improve the modelling process since they have a signature in the measured signal as the signal of the rift and the high velocity zone to the north of the craton as shown as shown in Figure 37 (A) and (D).

4.2.4.5. Evaluation

By comparing the results of the forward modelling with the work done on the area by Simiyu and Keller (1997) (Figure 39 (A) and (B)), some remarks can be mentioned. Their work modelled only four sections up to 200 km depth of the study area with few details in the deep part of the sections after 40 km depth (Figure 39 (A)). However, they included the crustal details in their work. Their model described the craton as a low density portion in the upper crust that ended at 40 km depth. However, the results of the seismic tomography showed that the root of the craton exceeded 100 km depth (Figure 7). Their work described the rift branches in the same manner as the results within this research. However, they defined the source of the rift as a head plume which does not correlate with the seismic tomography results. The forward modelling process in their work depended on seismic refraction profile, filtered gravity data and the surface measurements. Also, their work only modelled four sections over a larger study area than the study area of this research. However, the model out of this research includes more information about the deeper zone, based on 3D seismic tomography model, and it describes the full 3D density distribution of the area.

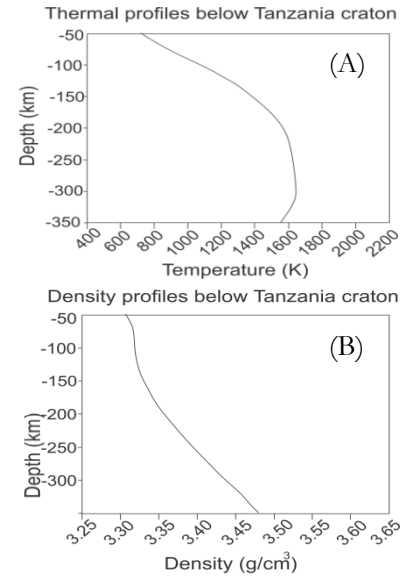


Figure 38: figure shows the low temperature in the zone that can be the reason for the low velocity in the inner plume zone.

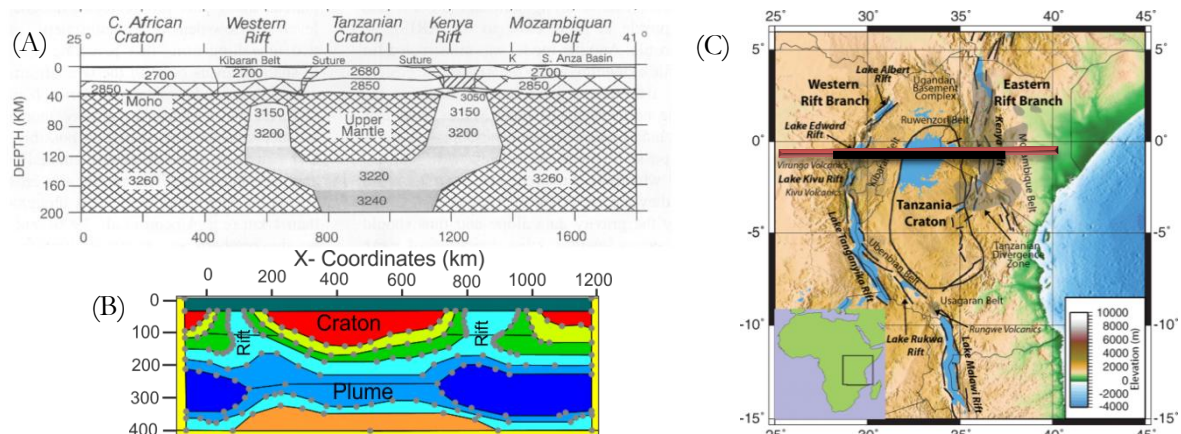


Figure 39: Figure shows the comparison between (A) the work of Simiyu and Keller (1997) and (B) the modelling of this research. (C) The study area map that shows the location and the extent of both sections.

4.2.5. Results constrained inversion

After the object based inversion process, the model was converted to voxels (Table 7), including the calculated density contrasts, in order to use it as a reference model for the constrained inversion process in GRAV3D.

X min	-100 km	length	1325 km	Step interval	27.25 km
Y min	8700 km	width	1600 km	Step interval	27.25 km
Z min	0	Depth range	500 km	Depth interval	5 km

Table 7: Table shows the spatial geometry of the exported 3D model out of the forward modelling process.

The model contained:

- 1- The spatial geometry of the 3D cube.
- 2- The calculated density contrast that produced the best fit with the filtered satellite gravity signal in the object-based inversion.

The MATLAB code created a 3D mesh based on the spatial geometry of the cube. Then, the codes were used to convert the density contrasts to a reference model that were used to constrain the inversion process (Figure 40 (A), (B), and (C)).

4.2.5.1. Preparing the gravity signal

The Bouguer gravity measurements were used in the inversion process (Figure 40 (I)) with 2% Gaussian noise added (Figure 40 (J)). The assigned error will be recalculated through the Generalized Cross Validation (GCV) mode of inversion. The GCV is a mode in the inversion process that estimates the regularization parameter automatically (the degree of the misfit required to end the inversion process). The GCV allows the estimation of the error in the data, and hence use it to estimate the regularization parameter require for the inversion (Haber and Oldenburg, 2000).

4.2.5.2. The inversion parameters

At this stage, the gravity signal, 3D mesh, and density reference models were already prepared. However, the inversion process required several parameters. The parameters used in the inversion were:

The parameter	The available values	The reason
Depth weighting	Depth Distance (Selected)	When depth constrains is available it is preferred to use the Distance weight method which bases the weight on the distance from constrains. It is also important to mention that in case of using reference model, the weighting function has no effect on the inversion results
Wavelet compression	Default User None (Selected)	The compression causes loss of some of the details in the model. Therefore, It was not included in the inversion.
Mode	Chifact Constant trade-off GCV (Selected)	The GCV (generalized cross validation) mode is the best choice in case of gravity data where error estimation is not available. GCV automatically estimates the error in the data and determine the regularization parameter based on it.
The aspect ratio	Lc, Ln, Lz (273,273,50)	The Alphas or aspect ratio determine the expected gross geometry in the model. In the case of the study area model, the model contains different objects with different geometries. Therefore, It is better to adjust the ratio according to the geometry of the cells (27.25km, 27.25km, 5 km \sim 275,273,50)

Table 8: Table shows the selected parameters for the inversion process and the explanation behind the selection of each parameter value.

4.2.5.3. The inversion process

The inversion process was carried out using the reference model as a constraint for the inversion process. The values of the density contrast for the different objects were used except the value of the crust. The crust was assigned no reference value to allow the inversion process to estimate the rapid variation in the density contrast within the shallow depth of the crust. However, to prevent the inversion process from concentrating all density contrasts in the empty zone of the crust; the inversion process was bounded by -

0.15 and 0.15 g/cm³. These bounds values allowed free estimations of the density contrast since the maximum and minimum density contrast in the reference model were 0.056 and -0.058. However, it prevented the over concentration of the density contrasts in the crustal layer. The results of the inversion are shown in Figure 40 ((A), (B), (C), (D), (E), (F), (G) and (H)).

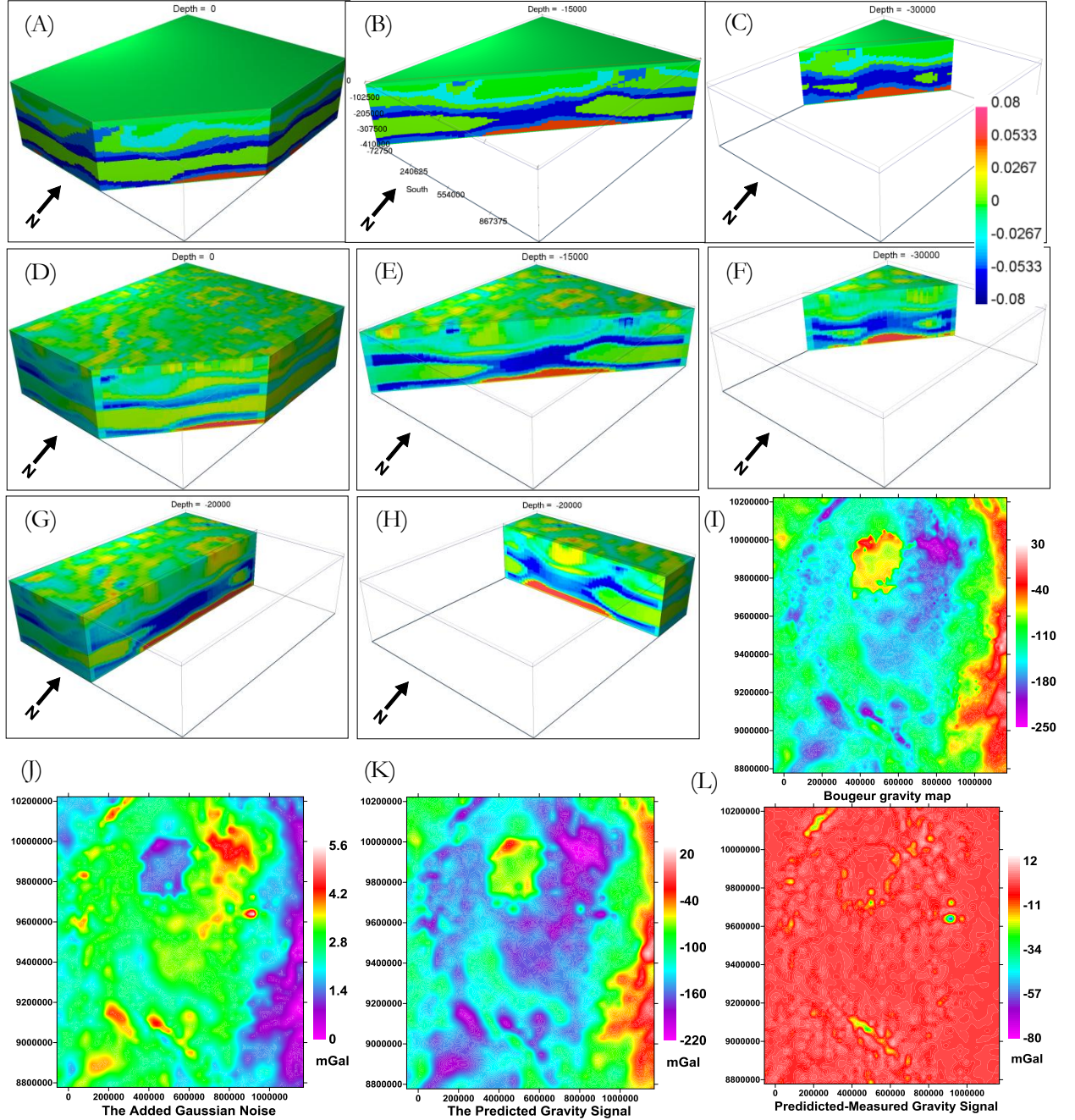


Figure 40: (A), (B), (C), (D), (E), (F), (G) and (H) are the results of the inversion process using density constraints as a reference model. (I) Bouguer satellite gravity measurements. (J) The added error to the Bouguer measurements. (K) The predicted gravity signal. (L) The difference between the measured Bouguer signal and the predicted signal.

4.2.5.4. The reference model results

The results of the inversion process using a reference model as a constraint showed enhanced details in the final inverted model. Also, the inversion process made some modifications to the density contrast of the objects and especially in the shallow zone (0:100 km). The model showed a re-distribution for density contrast of the objects. However, the influence of the inversion seems to be less on the deeper part of the model.

- *For the shallower part* of the model (crust 0:40 km depth), the model showed enhanced details of high and low density contrasts. It also logically connected the crust density anomalies with the middle part (40:200 km) that related to the upper mantle anomalies (Figure 40 (F) and (H)). This made the results geologically acceptable.
- *For the middle part* of the model (from 40:~250 km depth), the model showed that the general density contrast of the objects are preserved. However, parts from the craton were changed to higher density contrasts than in the reference model. Also, parts from the rift changed to lower density contrast than the reference model. The zone between the upper part, including the craton and the rifts, and the deep part, including the plume and the high velocity zone below it, showed a small variation related to the value of the dominant anomaly above it. In general, the model redistributed the variations within the objects as shown in (Figure 40 (H) and (E)).
- *For the deep part* of the model (Plume and the high velocity zone below it 250:400 km depth), the model preserved the general low density contrast of the plume. However, the density contrast was decreased and increased within different parts of it and its inner part as shown in (Figure 40 (D), (F) and (G)).

In general, the inversion process preserved the shape and the frame of the objects. The added value was the redistribution of the density contrasts within the object and the enhancement of the details in the shallow part. This was guided by the satellite gravity signal and the wavelength related content within it. The predicted gravity data had a good fit with the measured data. The errors in the predicted data were related to the evaluation of the Gaussian noise within the measured data, and they concentrated in the region of maximum and minimum measurements (Figure 40 (K)).

4.2.6. Discussion Constrained inversion

The inversion results (Figure 40) showed that the inversion process redistributed the density contrasts of the objects to improve the fit between the measured and the calculated satellite gravity data. Also, it enhanced the details in the shallow region of the model where there were no details from the object based inversion or the seismic tomography model. However, some parameters in the inversion process require some discussion.

4.2.6.1. The selected constraint format

The usage of the model of the forward modelling stage as a reference model was the optimum choice. The reference model constraints give the inversion process the frame to change within bounds without bias toward the predefined results. In case of the availability of density information with a high level of confidence, the bounds constraints are the favourable in that case. The shape of the extracted objects from the 3D OOA analysis had a high level of confidence because of the 70% correlation between the calculated gravity signal and the measured satellite one. However, the level of confidence was not the same for the estimated density contrasts. Hence, the usage of the reference model allowed the preservation of the main outline of the objects and in the same time allowed changes in the density contrast values to get the minimum misfit between the measured and the calculated gravity signal.

4.2.6.2. The inversion parameters

The inversion process required a lot of parameters. The parameter selection (Table 8) was based on selecting those parameters that would produce minimum loss of information or prevent bias in the inversion process. Clear choices were the non-compressional wavelet mode to prevent the loss of information in the estimated model, and the GCV value to estimate the acceptable misfit between the supplied reference model and the estimated one automatically. However, the selection of the Alphas is not an easy choice. The Alphas play an important role in shape and the depth extent of the estimated model. However, the criteria to select the optimum parameters are not clear and depend on trial and error.

4.2.6.3. Evaluation

The results were compared with the work done by Cammarano (2013). The work was based on assuming different mineralogical composition for the mantle and then the 3D S-wave seismic tomography model of the study area was converted into density using the equation of Stixrude and Lithgow-Bertelloni (2011). The authors used different mineralogical composition; however, there was no significant difference between them. However, not enough information is available about the models and the quality of the results since the work on the influence of composition is still on-going.

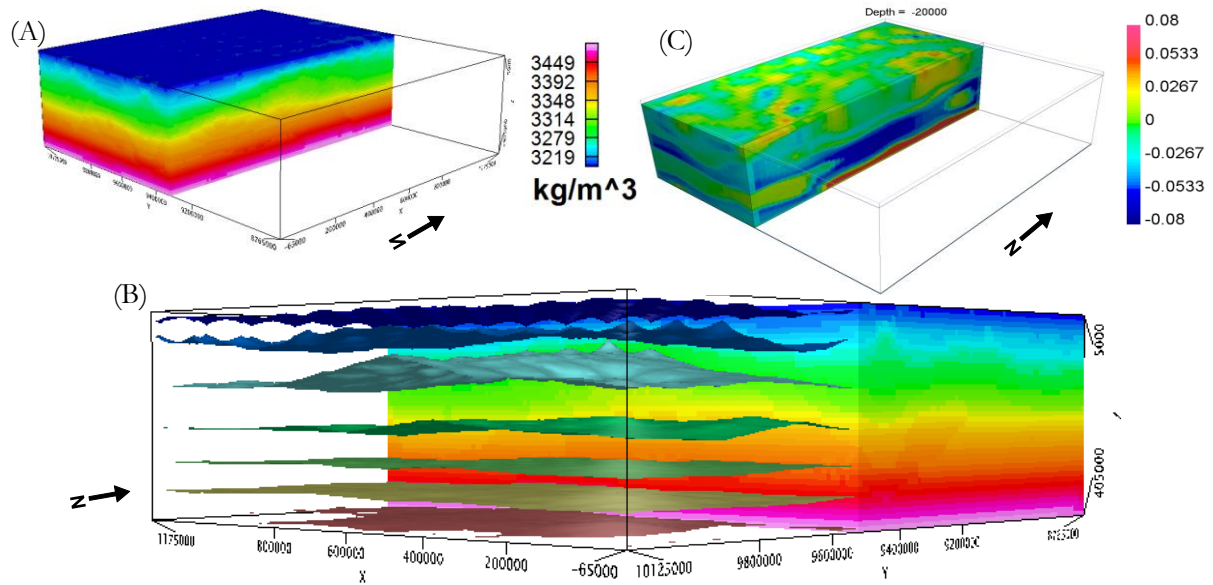


Figure 41: (A) Cammarano (2013) density model and (B) using seven equal intervals iso-surfaces. (C) The density model out of this study.

The model was displayed using histogram stretching to enhance the detail within the model. However, the model seems to be smooth and only describes the gradual variation with depth. Seven iso-density surfaces were created to define any object within the model. However, the model did not visually show any feature related to subsurface objects.

However, the model can be used in a different way. In case of the availability of the absolute density background of the study area, this model can be used to calculate the density contrast. Then, the calculated gravity signal out of this model can be compared with the forward gravity signal of the estimated model of this research. Also, the density contrast based on their model will be comparable with the density contrast results output from the constrained inversion process. It also can be used as additional constraints for controlling the inversion process. Also, information about the uncertainty within Cammarano (2013) model was not available since the work still work in progress.

Another important factor in the inversion process was the depth weighting function $w_r(z)$. This function describes the decay of the kernel function for the surface gravity data with depth. It controls the density contrast distribution with the depth. This function is one of the weak points of GRAV3D since it is the decay function of a spherical source within the model. The GRAV3D method can be improved by integrating one of the imaginative depth methods which are based on the upward continuation operator for data with the objective function of GRAV3D. This can provide a better depth weighting function that can partially retrieve the subsurface structures in the absence of a sufficient amount of the constraints.

4.2.6.4. General Discussion:

The different stages in the methodology work flow were linearly affecting each other. The improvement in each stage of the methodology can produce improvements in the final results. The 3D OOA rulesets for the 3D geophysical data need to be improved to be able to extract the actual location of the objects'

boundaries. The forward modelling IGMAS+ software needs development to become user friendly and allows to include fuzzy functions that can describe the fuzzy boundaries of the objects. The GRAV 3D inversion needs an improved depth weighting functions and also needs a clear methodology or automatic approach to define the Alphas of the inversion process.

5. CONCLUSION AND RECOMMENDATION

5.1. Conclusion

In this research, the state-of-art 3D OOA was able to extract 3D objects from 3D geophysical data. 3D OOA was tested first using a set of synthetic models that simulated the structure settings in the study area. 3D OOA was able to retrieve the synthetic models. The retrieved models showed a calculated gravity signal that had 99.8% correlation with the measured signal. Then, 3D OOA was used to extract subsurface objects from a 3D S-wave seismic tomography model of the central part of the East African Rift System. The extracted objects were used later to reconstruct the density contrast model of the study area through the forward modelling stage. The calculated gravity signal resulting from the reconstructed model had a 70% correlation with the filtered satellite gravity signal. The model from the forward modelling stage was used to constrain the inversion of the satellite gravity measurements using GRAV3D. The inversion process enhanced the details in the shallow part of the model and redistributed the density contrast within the object guided by the satellite gravity measurements. The answers of the research question were:

1- What is the capability of the 3D OOA to extract 3D objects out from 3D geophysical data?

3D OOA is capable to extract the 3D objects from the 3D geophysical data. The method revealed immense possibilities to extract the objects in different conditions, even in the case of fuzzy boundaries. The reconstructed models show 99.8 % correlation in case of synthetic models and 70% in the case of the real data; however, the estimated density contrast was not always optimal. This means that 3D OOA was able to solve the problem of the shape of the objects.

2- How will the 3D OOA represent the fuzzy characteristics of the geophysical subsurface bodies?

3D OOA was able to represent the fuzzy boundaries using the membership function. The membership function in eCognitions allows representing different kinds of fuzziness through different available membership functions.

3- How can the S-wave seismic tomography model represent the density distribution in the subsurface?

The S-wave seismic tomography model was successfully used as a basis for the definition of the shapes of 3D objects in the subsurface. The shape of each object had a signature in the measured satellite gravity signal. This signature allowed the estimation of the density contrast of each object.

4- What is the degree of the misfit? What is the effect of the low spatial resolution of the tomography model?

The misfit was 30% between the measured and the calculated gravity signal. This misfit was because the limitation in the reconstruction of fuzzy boundaries and high resolution detail in the forward modelling stage.

5- Can the forward model represent the regional gravity field of the study area?

Yes, the forward model using the extracted objects from the S-wave seismic tomography model was able to represent the regional field. It produced a calculated gravity signal that has a 70% correlation with the filtered (regional) satellite gravity.

6- How can the misfit between the calculated signal and the measured satellite gravity signal be adjusted?

The misfit can be minimized using the inversion technique with constraints from the reconstructed model. The inversion technique, GRAV3D, was able to reduce the misfit using the model output from the forward modelling stage with the estimated density contrasts.

7- How can the inversion of the satellite gravity data add to the 3D model of the study area?

The inversion process was able to enhance the shallow details in the model. Also, it was able to redistribute the density contrasts within the extracted objects according to the measured satellite gravity signal, even at larger depths.

5.2. Recommendations

The recommendations for the future research are:

- 1- 3D OOA can be efficiently used to interpret the 3D geophysical datasets which is a time consuming process. The link between 3D OOA in the biomedical field and the geophysical field should be established, since the biomedical field had improved steps ahead in the automatic interpretation and 3D objects extraction. Such techniques should be carefully studied and evaluated to use further in dealing with the 3D geophysical data.
- 2- 3D OOA rulesets need an improved approach to extract the location of the object boundaries in horizontal and vertical direction.
- 3- IGMAS+ has added an improved technique recently (Schmidt et al., 2011) that can add a voxel layer behind the object based model. This voxel layer can be used to describe the vertical variation in the density contrasts within the object. This approach can be used using Cammarano (2013) density model or using other equation to convert the S-wave seismic velocity model to density and use it to describe the density contrast distribution within the objects.
- 4- The depth weighting function in GRAV3D needs to be. One of the imagine depth methods as mentioned in Fedi and Pilkington (2012) or a new developed method can be used or invented to develop the software package.
- 5- The Alphas estimation in GRAV3D needs an automated approach to define them in case of the presence of constraints.

LIST OF REFERENCES

- ADAMS, A., NYBLADE, A. & WEERARATNE, D. 2012. Upper mantle shear wave velocity structure beneath the East African plateau: evidence for a deep, plateau-wide low velocity anomaly. *Geophysical Journal International*, 189, 123-142.
- ARISOY, M. O. & DIKMEN, U. 2011. Potensoft: MATLAB-based software for potential field data processing, modeling and mapping. *Computers & Geosciences*, 37, 935-942.
- ATHELOGOU, M., SCHMIDT, G., SCHÄPE, A., BAATZ, M. & BINNIG, G. 2007. Cognition Network Technology – A Novel Multimodal Image Analysis Technique for Automatic Identification and Quantification of Biological Image Contents Imaging Cellular and Molecular Biological Functions. In: SHORTE, S. L. & FRISCHKNECHT, F. (eds.). Springer Berlin Heidelberg.
- BARBOSA, V. C. F. & SILVA, J. B. C. 2011. Reconstruction of geologic bodies in depth associated with a sedimentary basin using gravity and magnetic data. *Geophysical Prospecting*, 59, 1021-1034.
- BARTHELMES, F., W., K. & PFLUG, H. 2011. *International Centre for Global Earth Models (ICGEM)* [Online]. Germany: GFZ German Research Centre for Geosciences. Available: <http://icgem.gfz-potsdam.de/ICGEM/> [Accessed August 26 2012].
- BEZADA, M. J. & ZELT, C. A. 2011. Gravity inversion using seismically derived crustal density models and genetic algorithms: an application to the Caribbean–South American Plate boundary. *Geophysical Journal International*, 185, 577-592.
- BILGILI, E., GOKNAR, I. C., ALBORA, A. M. & UCAN, O. N. 2005. Potential anomaly separation and archeological site localization using genetically trained multi-level cellular neural networks. *Etri Journal*, 27, 294-303.
- BLASCHKE, T. 2010. Object based image analysis for remote sensing. *ISPRS Journal of Photogrammetry and Remote Sensing*, 65, 2-16.
- BLOCK, A. E., BELL, R. E. & STUDINGER, M. 2009. Antarctic crustal thickness from satellite gravity: Implications for the Transantarctic and Gamburtsev Subglacial Mountains. *Earth and Planetary Science Letters*, 288, 194-203.
- BOSZCZUK, P., CHENG, L. Z., HAMMOUCHE, H., ROY, P., LACROIX, S. & CHEILLETZ, A. 2011. A 3D gravity data interpretation of the Matagami mining camp, Abitibi Subprovince, Superior Province, Québec, Canada: Application to VMS deposit exploration. *Journal of Applied Geophysics*, 75, 77-86.
- BROCHER, T. M. 2005. Empirical Relations between Elastic Wavespeeds and Density in the Earth's Crust. *Bulletin of the Seismological Society of America*, 95, 2081-2092.
- CAHEN, L. 1984. *The Geochronology and Evolution of Africa*. Clarendon Press.
- CAMMARANO, F. 15/9/2013 2013. RE: *Density and thermal models of East African Rift System using seismic tomography*.
- CAMMARANO, F., TACKLEY, P. & BOSCHI, L. 2011. Seismic, petrological and geodynamical constraints on thermal and compositional structure of the upper mantle: global thermochemical models. *Geophysical Journal International*, 187, 1301-1318.
- CHRISTENSEN, N. I. & MOONEY, W. D. 1995. Seismic velocity structure and composition of the continental crust: A global view. *Journal of Geophysical Research: Solid Earth*, 100, 9761-9788.
- CLAERBOUT, J. F. 1988. *Fundamentals of Geophysical Data Processing with Applications to Petroleum Prospecting*, Palo Alto, California, USA, Blackwell Scientific Publications.
- DIAS, F., BARBOSA, V. C. F. & SILVA, J. B. C. 2009. 3D gravity inversion through an adaptive-learning procedure. *Geophysics*, 74, I9-I21.
- DORNINGER, P. & PFEIFER, N. 2008. A Comprehensive Automated 3D Approach for Building Extraction, Reconstruction, and Regularization from Airborne Laser Scanning Point Clouds. *Sensors*, 8, 7323-7343.
- EBBING, J., BRAITENBERG, C. & GÖTZE, H. J. 2001. Forward and inverse modelling of gravity revealing insight into crustal structures of the Eastern Alps. *Tectonophysics*, 337, 191-208.
- ECOGNITION DEVELOPER 2011. *eCognition Developer 8.7 Reference Book*, München, Germany, Trimble Germany GmbH, Trappentreustr. .
- ELLIS, R. 2010. Non-Uniqueness in Potential Field inversion. Available: <http://www.geosoft.com/media/uploads/resources/technical-papers/non-uniqueness-in-potential-field-inversion.pdf> [Accessed 10/11/2012].

- ERKAN, K., JEKELI, C. & SHUM, C. K. 2012. Fusion of gravity gradient and magnetic field data for discrimination of anomalies using deformation analysis. *Geophysics*, 77, F13-F20.
- FEDI, M. & PILKINGTON, M. 2012. Understanding imaging methods for potential field data. *Geophysics*, 77, G13-G24.
- FEDI, M., PRIMICERI, R., QUARTA, T. & VILLANI, A. V. 2004. Joint application of continuous and discrete wavelet transform on gravity data to identify shallow and deep sources. *Geophysical Journal International*, 156, 7-21.
- FORSYTH, D. W. & LI, A. 2005. Array analysis of two-dimensional variations in surface wave phase velocity and azimuthal anisotropy in the presence of multipathing interference. *Seismic Earth: Array Analysis of Broadband Seismograms*. Washington, DC: AGU.
- GOETZE, H. J. & LAHMEYER, B. 1988. Application of three-dimensional interactive modeling in gravity and magnetics. *Geophysics*, 53, 1096-1108.
- GÓMEZ-ORTIZ, D. & AGARWAL, B. N. P. 2005. 3DINVER.M: a MATLAB program to invert the gravity anomaly over a 3D horizontal density interface by Parker–Oldenburg's algorithm. *Computers & Geosciences*, 31, 513-520.
- GREICIUS, T. 2012. *GRACE Mission Overview* [Online]. NASA. Available: http://www.nasa.gov/mission_pages/Grace/overview/index.html [Accessed 31 May 2012].
- HAASE, C. 2008. *Inversion of gravity, gravity gradient, and magnetic data with application to subsalt imaging*.
- HAAZ, I. 1953. Relationship between the potential of the attraction of the mass contained in a finite rectangular prism and its first and second derivatives. *Geofizikai Közlemenyek*, II.
- HABER, E. & OLDENBURG, D. 2000. A GCV based method for nonlinear ill-posed problems. *Computational Geosciences*, 4, 41-63.
- HARTMAN, R. R., TESKEY, D. J. & FRIEDBERG, J. L. 1971. A SYSTEM FOR RAPID DIGITAL AEROMAGNETIC INTERPRETATION. *Geophysics*, 36, 891-918.
- HIRSCH, K. K., BAUER, K. & SCHECK-WENDEROTH, M. 2009. Deep structure of the western South African passive margin — Results of a combined approach of seismic, gravity and isostatic investigations. *Tectonophysics*, 470, 57-70.
- HOEFLE, B., HOLLAUS, M. & HAGENAUER, J. 2012. Urban vegetation detection using radiometrically calibrated small-footprint full-waveform airborne LiDAR data. *ISPRS Journal of Photogrammetry and Remote Sensing*, 67, 134-147.
- HOLDEN, E.-J., WONG, J. C., KOVESI, P., WEDGE, D., DENTITH, M. & BAGAS, L. 2012. Identifying structural complexity in aeromagnetic data: An image analysis approach to greenfields gold exploration. *Ore Geology Reviews*, 46, 47-59.
- HUERTA, A. D., NYBLADE, A. A. & REUSCH, A. M. 2009. Mantle transition zone structure beneath Kenya and Tanzania: more evidence for a deep-seated thermal upwelling in the mantle. *Geophysical Journal International*, 177, 1249-1255.
- HWANG, C., KAO, E.-C. & PARSONS, B. 1998. Global derivation of marine gravity anomalies from Seasat, Geosat, ERS-1 and TOPEX/POSEIDON altimeter data. *Geophysical Journal International*, 134, 449-459.
- JULIÀ, J., AMMON, C. J. & NYBLADE, A. A. 2005. Evidence for mafic lower crust in Tanzania, East Africa, from joint inversion of receiver functions and Rayleigh wave dispersion velocities. *Geophysical Journal International*, 162, 555-569.
- KABAN, M. K. 2011. Gravity Anomalies, Interpretation. In: GUPTA, H. K. (ed.) *Encyclopedia of Solid Earth Geophysics*. Springer Netherlands.
- KAMPUNZU, A. B., BONHOMME, M. G. & KANIKA, M. 1998. Geochronology of volcanic rocks and evolution of the Cenozoic Western Branch of the East African Rift System. *Journal of African Earth Sciences*, 26, 441-461.
- KIM, N. 2011. *2,5 D reconstruction of building from very high resolution SAR and optical data by using object - oriented image analysis*. University of Twente Faculty of Geo-Information and Earth Observation (ITC).
- LAST, R. J., NYBLADE, A. A., LANGSTON, C. A. & OWENS, T. J. 1997. Crustal structure of the East African Plateau from receiver functions and Rayleigh wave phase velocities. *J. Geophys. Res.*, 102, 24469-24483.
- LI, X. Efficient 3D gravity and magnetic modeling. EGM 2010 International Workshop, Capri, Italy, Expanded Abstracts, 2010.
- LI, Y. G. & OLDENBURG, D. W. 1996. 3-D inversion of magnetic data. *Geophysics*, 61, 394-408.
- LI, Y. G. & OLDENBURG, D. W. 1998. 3-D inversion of gravity data. *Geophysics*, 63, 109-119.

- LOEKKEN, S. 2012a. *GOCE Science Goals* [Online]. European Space Agency (ESA). Available: https://earth.esa.int/web/guest/missions/esa-operational-eo-missions/goce/science#_56_INSTANCE_4yXL_matmp [Accessed 29 May 2012].
- LOEKKEN, S. 2012b. *What is GOCE?* [Online]. European Space Agency (ESA). Available: <https://earth.esa.int/web/guest/missions/esa-operational-eo-missions/goce> [Accessed 29 May 2012].
- MAIER, B., TIEDE, D. & DORREN, L. 2008. Characterising mountain forest structure using landscape metrics on LiDAR-based canopy surface models. In: BLASCHKE, T., LANG, S. & HAY, G. J. (eds.) *Object-Based Image Analysis*. Springer Berlin Heidelberg.
- MARSCHALLINGER, R., HOFMANN, P., DAXNER-HÖCK, G. & KETCHAM, R. A. 2011. Solid modeling of fossil small mammal teeth. *Computers & Geosciences*, 37, 1364-1371.
- MARTHA, T. R., KERLE, N., VAN WESTEN, C. J., JETTEN, V. & KUMAR, K. V. 2011. Segment Optimization and Data-Driven Thresholding for Knowledge-Based Landslide Detection by Object-Based Image Analysis. *Geoscience and Remote Sensing, IEEE Transactions on*, 49, 4928-4943.
- MISHRA, D. C., KUMAR, M. R. & ARORA, K. 2012. Long wavelength satellite gravity and geoid anomalies over Himalaya, and Tibet: Lithospheric structures and seismotectonics of deep focus earthquakes of Hindu Kush - Pamir and Burmese arc. *Journal of Asian Earth Sciences*, 48, 93-110.
- MUSHAYANDEBVU, M. F., LESUR, V., REID, A. B. & FAIRHEAD, J. D. 2004. Grid Euler deconvolution with constraints for 2D structures. *Geophysics*, 69, 489-496.
- NABIGHIAN, M. N., ANDER, M. E., GRAUCH, V. J. S., HANSEN, R. O., LAFEHR, T. R., LI, Y., PEARSON, W. C., PEIRCE, J. W., PHILLIPS, J. D. & RUDER, M. E. 2005. 75th Anniversary - Historical development of the gravity method in exploration. *Geophysics*, 70, 63ND-89ND.
- NGUYEN, H. T., PEARCE, J. M., HARRAP, R. & BARBER, G. 2012. The Application of LiDAR to Assessment of Rooftop Solar Photovoltaic Deployment Potential in a Municipal District Unit. *Sensors*, 12, 4534-4558.
- NOLET, G. 2011. Seismic Tomography
In: GUPTA, H. K. (ed.) *Encyclopedia of Solid Earth Geophysics*. Springer Netherlands.
- O'BRIEN, J., RODRIGUEZ, A., SIXTA, D., DAVIES, M. A. & HOUGHTON, P. 2005. Resolving the K-2 salt structure in the Gulf of Mexico. *The Leading Edge*, 24, 404-409.
- OASIS MONTAJ 2010. *Oasis Montaj help*, Toronto, ON Canada, Geosoft Incorporated.
- OWENS, T. J., NYBLADE, A. A., GURROLA, H. & LANGSTON, C. A. 2000. Mantle transition zone structure beneath Tanzania, east Africa. *Geophys. Res. Lett.*, 27, 827-830.
- PARK, Y., NYBLADE, A. A., RODGERS, A. J. & AL-AMRI, A. 2008. S wave velocity structure of the Arabian Shield upper mantle from Rayleigh wave tomography. *Geochem. Geophys. Geosyst.*, 9, Q07020.
- PARKER, R. L. 1973. RAPID CALCULATION OF POTENTIAL ANOMALIES. *Geophysical Journal of the Royal Astronomical Society*, 31, 447-455.
- RAWLINSON, N., POZGAY, S. & FISHWICK, S. 2010. Seismic tomography: A window into deep Earth. *Physics of the Earth and Planetary Interiors*, 178, 101-135.
- REID, A. B., ALLSOP, J., GRANSER, H., MILLET, A. & SOMERTON, I. 1990. Magnetic interpretation in three dimensions using Euler deconvolution. *Geophysics*, 55, 80-91.
- RITSEMA, J., NYBLADE, A. A., OWENS, T. J., LANGSTON, C. A. & VANDECAR, J. C. 1998. Upper mantle seismic velocity structure beneath Tanzania, east Africa: Implications for the stability of cratonic lithosphere. *J. Geophys. Res.*, 103, 21201-21213.
- ROTARSKA-JAGIELA, A., SCHÖNMEYER, R., OERTEL, V., HAENSCHER, C., VOGELY, K. & LINDEN, D. E. J. 2008. The corpus callosum in schizophrenia-volume and connectivity changes affect specific regions. *NeuroImage*, 39, 1522-1532.
- SANDWELL, D. T. & SMITH, W. H. F. 1997. Marine gravity anomaly from Geosat and ERS 1 satellite altimetry. *JOURNAL OF GEOPHYSICAL RESEARCH-ALL SERIES-*, 102, 10-10.
- SCHMIDT, G., KIETZMANN, M., KIM, J. & BINNIG, G. 2010. Cognition Network Technology for Fully Automatic 3D Segmentation of Lymph Nodes in CT Data
In: DÖSSEL, O. & SCHLEGEL, W. C. (eds.) *World Congress on Medical Physics and Biomedical Engineering*. Munich, Germany: Springer Berlin Heidelberg.
- SCHMIDT, S., PLONKA, C., GÖTZE, H. J. & LAHMEYER, B. 2011. Hybrid modelling of gravity, gravity gradients and magnetic fields. *Geophysical Prospecting*, 59, 1046-1051.
- SERTCELİK, I. & KAFADAR, O. 2012. Application of edge detection to potential field data using eigenvalue analysis of structure tensor. *Journal of Applied Geophysics*, 84, 86-94.

- SIMIYU, S. M. & KELLER, G. R. 1997. An integrated analysis of lithospheric structure across the East African plateau based on gravity anomalies and recent seismic studies. *Tectonophysics*, 278, 291-313.
- SPECTOR, A. & GRANT, F. S. 1970. Statistical models for interpreting aeromagnetic data. *Geophysics*, 35, 293-&.
- SPICER, B., MORRIS, B. & UGALDE, H. 2011a. Structure of the Rambler Rhyolite, Baie Verte Peninsula, Newfoundland: Inversions using UBC-GIF Grav3D and Mag3D. *Journal of Applied Geophysics*, 75, 9-18.
- SPICER, B., MORRIS, B. & UGALDE, H. 2011b. Structure of the Rambler Rhyolite, Bale Verte Peninsula, Newfoundland: Inversions using UBC-GIF Grav3D and Mag3D. *Journal of Applied Geophysics*, 75, 9-18.
- STIXRUDE, L. & LITHGOW-BERTELLONI, C. 2011. Thermodynamics of mantle minerals – II. Phase equilibria. *Geophysical Journal International*, 184, 1180-1213.
- STROBL, J. 2008. Segmentation-based Terrain Classification. In: ZHOU, Q., LEES, B. & TANG, G.-A. (eds.) *Advances in Digital Terrain Analysis*. Springer Berlin Heidelberg.
- TAPLEY, B. D. & KIM, M.-C. 2001. Chapter 10 Applications to Geodesy. In: LEE-LUENG, F. & ANNY, C. (eds.) *International Geophysics*. Academic Press.
- TEDLA, G. E., VAN DER MEIJDE, M., NYBLADE, A. A. & VAN DER MEER, F. D. 2011. A crustal thickness map of Africa derived from a global gravity field model using Euler deconvolution. *Geophysical Journal International*, 187, 1-9.
- THOMPSON, D. T. 1982. EULDPH - A new technique for making computer-assisted depth estimates from Magnetic data. *Geophysics*, 47, 31-37.
- VAN DER MEIJDE, M. 2011. Earth structure from gravity : exploring GOCE for subsurface information : powerpoint. Presented at special seminar at the Universidade Federal do Rio Grande do Norte (UFRN), 16 November 2011, Natal, Brazil. 30 slides.
- WALKER, K. T., NYBLADE, A. A., KLEMPERER, S. L., BOKELMANN, G. H. R. & OWENS, T. J. 2004. On the relationship between extension and anisotropy: Constraints from shear wave splitting across the East African Plateau. *J. Geophys. Res.*, 109, B08302.
- WANG, G., ZHANG, S., YAN, C., SONG, Y., SUN, Y., LI, D. & XU, F. 2011. Mineral potential targeting and resource assessment based on 3D geological modeling in Luanchuan region, China. *Computers & Geosciences*, 37, 1976-1988.
- WANG, G., ZHU, Y., ZHANG, S., YAN, C., SONG, Y., MA, Z., HONG, D. & CHEN, T. 2012. 3D geological modeling based on gravitational and magnetic data inversion in the Luanchuan ore region, Henan Province, China. *Journal of Applied Geophysics*, 80, 1-11.
- WILLHAUCK, G. 2012. *eCognition Community, 3D LiDAR Point Cloud Analysis* [Online]. Munich, Germany. Available: <http://community.ecognition.com/home/ecognition-labs/3d-lidar-point-cloud-analysis/?searchterm=3D> [Accessed 01/09/2012 2012].
- WILLIAMS, N. C. 2008. *Geologically-constrained UBC-GIF gravity and magnetic inversions with examples from the Agnew-Wiluna greenstone belt, Western Australia*. University of British Columbia.
- WILTSE, M. A., PRAKASH, A. & BURNS, L. E. 2009. Image analysis of airborne geophysical data from the Salcha River - Pogo area, Alaska. *Canadian Journal of Remote Sensing*, 35, S56-S71.
- ZHANG, L., HAO, T. & JIANG, W. 2009. Separation of potential field data using 3-D principal component analysis and textural analysis. *Geophysical Journal International*, 179, 1397-1413.

APPENDIX 1

The ruleset for the simple models

- 3D Segmentation
 - _threshold=auto threshold on Layer 1
 - creating 'Objects': _NonObject <= _threshold < _Object on Layer 1
 - all at Objects: convert image objects -> Connected 3D

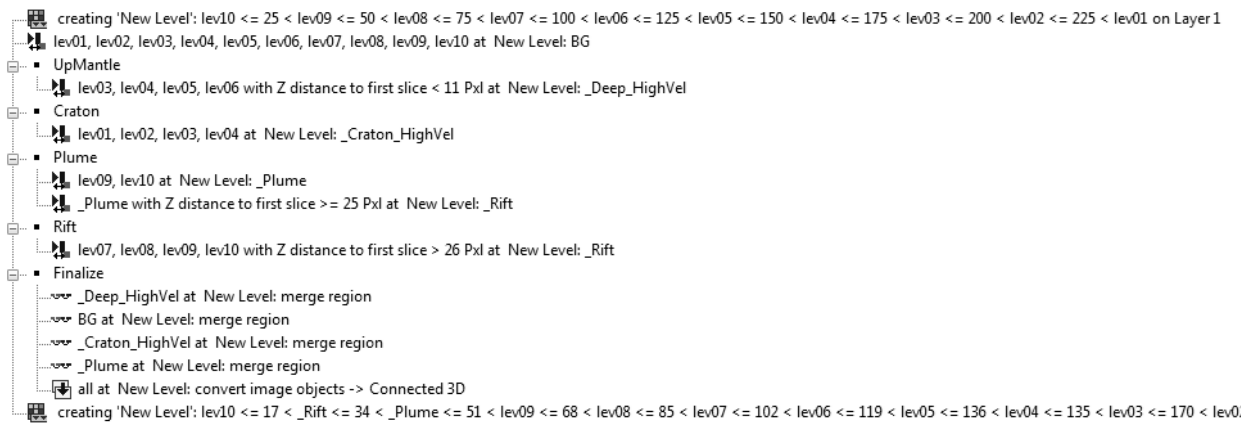
The ruleset for the first complex model

- Complex_3FuzzyZones
 - _threshold=auto threshold on Layer 1
 - creating 'objects': _Objects <= _threshold < _Background on Layer 1
 - _Objects at objects: 10 [shape:0.1 compact:0.1]
 - Background
 - _Objects with Mean Layer 1 <= 12 at objects: _Background
 - _Background at objects: merge region
 - _Background with Number of pixels < 300000 at objects: _Objects
 - Craton
 - _Objects with Mean Layer 1 = 20 at objects: _Craton
 - _Craton at objects: merge region
 - Rift
 - _Objects with Mean Layer 1 = 128 at objects: _Rift
 - _Rift at objects: merge region
 - Plume
 - _Rift with Z distance to first slice <= 36 Pxl at objects: _Plume
 - _Craton with Z distance to first slice <= 36 Pxl at objects: _Objects
 - _Plume with Number of pixels <= 800 at objects: _Objects
 - Boundary
 - _Craton, _Plume_Boundary, _Plume, _Rift_Boundary, _Rift at objects: convert image objects -> Connected 3D
 - _Objects with Z distance to first slice >= 44 Pxl at objects: _Rift_Boundary
 - _Objects with Z distance to first slice <= 35 Pxl at objects: _Plume_Boundary
 - _Objects with Z distance to first slice <= 43 Pxl and Mean Layer 1 = 32 at objects: _Plume_Boundary
 - _Objects with Z distance to first slice <= 43 Pxl and Z distance to first slice >= 36 Pxl at objects: enclosed by _Plume_Boundary: _Plume_Boundary +
 - _Objects with Z distance to first slice = 36 Pxl and Mean Layer 1 = 72 at objects: unclassified
 - unclassified with Number of pixels < 2000 at objects: _Objects
 - _Objects with Mean Layer 1 = 52 and Z distance to first slice = 36 Pxl at objects: unclassified
 - _Objects at objects: enclosed by unclassified: unclassified +
 - unclassified at objects: _Plume_Boundary
 - _Objects, _Plume_Boundary at objects: enclosed by _Craton: _Plume_Boundary +
 - _Plume_Boundary at objects: merge region
 - _Plume_Boundary with Number of pixels < 450 at objects: _Objects
 - loop: _Rift_Boundary at objects: grow(z-) into _Objects
 - 5x: _Plume_Boundary at objects: <- _Objects
 - _Craton with Z distance to first slice = 36 Pxl at objects: _Plume_Boundary
 - _Plume_Boundary at objects: merge region
 - _Objects at objects: _Rift_Boundary
 - _Rift_Boundary at objects: merge region
 - 12x: _Plume_Boundary with Z distance to first slice > 40 Pxl and Z distance to first slice < 43 Pxl at objects: grow(x) into _Rift_Boundary where Layer 1 < 100
 - _Plume_Boundary with Z distance to first slice = 16 Pxl at objects: _Plume
 - _Plume at objects: merge region
 - _Craton, _Plume_Boundary, _Plume, _Rift_Boundary, _Rift at objects: convert image objects -> Connected 3D
 - export view to ExportView

The ruleset for the second complex model



The ruleset of the real data



APPENDIX 2

The XML file to convert the image slices to 3D image stack

```
<?xml version="1.0" encoding="UTF-8"?>
<scene><layout columns="1"></layout>
<files>*.jpg</files>
</scene>
```


APPENDIX 3

The MATLAB Code to convert the real data voxel into mesh that can be adjusted according to the input voxel through the values of the densities in the for loop

```
close all
clear all
clc

% read the reference file
[nameref, pathref] = uigetfile('*.den', 'Select the modified reference
model code file');
if isequal(nameref,0)
    disp('User selected Cancel')
else
    disp(['User selected', pathref nameref]);
end

fullfileref=[pathref nameref];
fidref_in=fopen(fullfileref,'r');
if (fidref_in==-1)
    disp('Unable to open VOXEL file');
    return;
end
fileref=importdata(fullfileref);
fclose(fidref_in);

%% read voxel file
[name, path] = uigetfile('*.vxo', 'Select a MATLAB code file');
if isequal(name,0)
    disp('User selected Cancel')
else
    disp(['User selected', path name]);
end

fullfile=[path name];
fid_in=fopen(fullfile,'r');
if (fid_in==-1)
    disp('Unable to open VOXEL file');
    return;
end
file=importdata(fullfile);
fclose(fid_in);

% read the data from voxel file
nx= str2double(file.textdata{3,1} (5:length(file.textdata{3,1})));
ny= str2double(file.textdata{4,1} (5:length(file.textdata{4,1})));
nz= str2double(file.textdata{5,1} (5:length(file.textdata{5,1})));

dx= str2double(file.textdata{6,1} (5:length(file.textdata{6,1})));
dy= str2double(file.textdata{7,1} (5:length(file.textdata{7,1})));
dz= str2double(file.textdata{8,1} (5:length(file.textdata{8,1})));

lowercoor=file.textdata{9,1} (9:length(file.textdata{9,1})-1);
[r]=find(lowercoor ==',');
lowx=str2double(lowercoor(1:r(1,1)-1));
lowy=str2double(lowercoor(r(1,1)+1:r(1,2)-1));
lowz=str2double(lowercoor(r(1,2)+1:length(lowercoor)));
```



```

uppercoor=file.textdata{10,1}(9:length(file.textdata{10,1})-1);
[v]=find(uppercoor ==',' );
upperx=str2double(uppercoor(1:v(1,1)-1));
uppery=str2double(uppercoor(v(1,1)+1:v(1,2)-1));
upperz=str2double(uppercoor(v(1,2)+1:length(uppercoor)));

data=[file.data(:,2),file.data(:,1),file.data(:,3)*-1,file.data(:,4)];
datasorted=sortrows(data,[1 2 3]);

%% wrirtting the parameter of the mesh file

NE=nx;
NN=ny;
NV=nz;
E0=lowx;
N0=lowy;
V0=upperz;

%% Replace density
datasortedmod= [datasorted(:,1) datasorted(:,2) datasorted(:,3) fileref];
bounds=zeros(length(datasortedmod),2);

for i=1: length(datasortedmod)

    if datasortedmod(i,4)==1 % Litho
        datasortedmod(i,4)= 0.15;
%        0.118;
        bounds(i,1)= -0.15;
        bounds(i,2)= 0.15;
    else
        end

    if datasortedmod(i,4)==2 % craton
        datasortedmod(i,4)= 0.001;
        bounds(i,1)= 0.001-0.05;
        bounds(i,2)= 0.001+0.05;
    else
        end
    if datasortedmod(i,4)==3 % yellow green
        datasortedmod(i,4)= -0.025;
        bounds(i,1)= -0.025-0.05;
        bounds(i,2)= -0.025+0.05;
    else
        end
    if datasortedmod(i,4)==4 % green
        datasortedmod(i,4)= 0.003;
        bounds(i,1)= 0.003-0.05;
        bounds(i,2)= 0.003+0.05;
    else
        end
    if datasortedmod(i,4)==5 % cyan
        datasortedmod(i,4)= -0.047;
        bounds(i,1)= -0.047-0.05;
        bounds(i,2)= -0.047+0.05;
    else
        end
    if datasortedmod(i,4)==6 % Light blue

```



```

        datasortedmod(i,4)= -0.058;
        bounds(i,1)= -0.058-0.005;
        bounds(i,2)= -0.058+0.05;
    else
    end
    if datasortedmod(i,4)==7 % blue
        datasortedmod(i,4)= 0.006;
        bounds(i,1)= 0.006-0.005;
        bounds(i,2)= 0.006+0.05;
    else
    end

    if datasortedmod(i,4)==8 % upmantle
        datasortedmod(i,4)= 0.056;
        bounds(i,1)= 0.056-0.05;
        bounds(i,2)= 0.056+0.05;
    else
    end

    if datasortedmod(i,4)==0
        datasorted(i,4)=0;
        bounds(i,1)=-0.1;
        bounds(i,2)=0.1;
    else
    end

end

%% write reference file
output_denname = 'reference_const.den';
fOut_den       = fopen(output_denname,'w');
fprintf(fOut_den,'%f\n',datasortedmod(:,4));
fclose(fOut_den);

%% write bounds1 file
output_denname = 'bounds1.den';
fOut_den       = fopen(output_denname,'w');
fprintf(fOut_den,'%f\n',bounds(:,1));
fclose(fOut_den);

%% write bounds2 file
output_denname = 'bounds2.den';fOut_den = fopen(output_denname,'w');
fprintf(fOut_den,'%f\n',bounds(:,2));
fclose(fOut_den);

```